MAGNETORESISTIVE ELEMENTS IN COMBINATION WITH SCHOTTKY-BARRIERS ON GALLIUM ARSENIDE

Ph.D. thesis by Jan Bornemeier,
born on April, 16th. 1974 in Detmold

University of Bielefeld
Department of Physics
Nano Device Group

February 3, 2005

Dated: February 2005

ERKLÄRUNG

Hiermit versichere ich, dass ich die vorliegende Arbeit selbständig verfasst habe und keine als die angegebenen Quellen und Hilfsmittel verwendet habe.

Bielefeld, den 3.2.2005

Jan Bornemeier

Erstgutachter:	P.D. Dr. H. Brückl
Zweitgutachter:	Prof. Dr. M. Sauer

Table of Contents

Preface

One of the most promising and exciting developments in state of the art physics is the so called *Spinelectronic* (*Spintronic*) technology. Present semiconductor devices rely on the precise manipulation of electronic charge. In spintronic devices not only the charge of an electron but also its spin is utilized. This additional degree of freedom allows the construction of completely new non-volatile electronic components. Such applications are based on different magnetoresistive effects. The scientific research concentrates primarily on the Giant Magneto Resistance (GMR) and the Tunnel Magneto Resistance (TMR) effect [1][2]; the high potential for applications accelerated this development [3][4].

Beyond the industrial interest in applications the nature of magnetism and electronic transport can be studied by specialized spinelectronic devices. Thin film GMR multilayers for example have been used for the first quantifications of the spin attenuation lengths in transition metals [5][6][7][8], predicted by *Mott* [9].

Especially experiments with ballistic electrons can deliver interesting information about, e.g. spin scattering in ferromagnetic metals [10][11]. Since the invention of Ballistic Electron Emission Microscopy (BEEM), several different experiments on attenuation length and metal/semiconductor interface characterization have been accomplished using this upgraded Scanning Tunnel Microscope (STM) [12].

A different approach looks at ballistic currents generated in solid state structures, in particular MR-junctions. Current research of IBM (Almaden) investigates Magnetic Tunnel Transistors (MTT) and similar Schottky tunnel-barrier hybrid junctions, which inject ballistically spin-polarized currents into multiple quantum wells, thus into a Light-Emitting Diode (LED) [13]. The spin direction of the injected electrons affects the circular polarization of the emitted light. From the determined spin-polarizations it is possible to obtain spin diffusion lengths inside the semiconductor, here Gallium Arsenide.

A possible application for spin-polarized currents in semiconductors can be all kinds of spin-transistors. *Das* and *Datta* proposed a possible lateral spin-transistor setup based on a Schottky-gate between ferromagnetic structures used as source and drain [14]. Unfortunately the spin-polarization measured in this configuration does not exceed $\approx 0.1\%$ [15][16][17]. The experiment requires highly polarized currents due to the so-called *conductivity mismatch* or *fundamental obstacle* for electrical spin injection from a ferromagnetic metal into a diffusive semiconductor [18]: Both spin channels get filled up by electrons due to the fact that the density of charge carriers inside the semiconductor is about 4 orders of magnitude lower than in metals and furthermore the semiconductor's conduction band is not spin-split; the polarization is virtually lost. Injection via a tunnel magnetoresistive junction is a promising solution to deal with this: small but highly polarized currents can conserve the polarization during the injection.

Although spintronic is a popular subject in actual research scattering processes and injection of spin polarized currents into semiconductors are not yet fully understood. The reason might be the challenging demands of the experimental setups and the topical bridging between the two disciplines of semiconductor physics and magnetism. Only few and partially inconsistent data for spin attenuation lengths in transition metals and causations for temperature and energy dependent scattering can be found in the literature for typical energies of about 1 eV. Furthermore, spin transistors with metal polarizer and analyzer[1] have not been fabricated yet.

The preparation and use of different injection tools for spin-polarized ballistic electrons is outlined in this thesis. Hybrid junctions, consisting of MR-junctions, tunnel and Schottky-barriers are characterized and compared with the theory. It is shown that ballistic currents are injected into semiconductor substrates. These currents should be highly spin-polarized. With help of the the experimental results spin attenuation lengths in Cobalt are calculated and discussed. The effect ratio

---

[1] Spin transistors with dilute ferromagnetic semiconductors as a polarizer have been successfully fabricated [19].

measured in the ballistic current is compared to the predicted ratio, calculated from attenuation lengths.

Moreover BEEM investigations on spinvalves are presented. BEEM is presented as a tool to map magnetic domains in spinvalves. Additionally, magnetization dependent spectroscopy on spinvalves has been accomplished and the results are compared with theoretical predictions. Magnetic major-loops of the investigated junction are measured in the ballistic current.

Experimental Idea

Experiments with ballistic electrons in specialized MR-junctions are the content of this thesis. Hybrid samples consisting of Magnetic Tunnel Junctions (MTJs) and Schottky-barriers have been developed, optimized, fabricated, and investigated for that purpose. Continuative experiments have also been done.

The ambition is to inject spin-polarized electrons above the Fermi level into a semiconductor substrate. The spin-polarization of a ferromagnetic thin film is usually ≈30-50% at room temperature, depending on the metal, refer to e.g. [20]. A magnetic tunnel junction consists of two ferromagnetic thin films, separated by a thin insulating tunnel barrier. This stack is usually embedded in conductive layers and seed layers to improve the growth during the deposition. The use of layers which affect the coercive fields of the ferromagnetic electrodes is common, too. If the ferromagnetic films are magnetized antiparallel, the electrical tunnel resistance is phenomenologically higher than in parallel alignment, when a bias is applied at the tunnel-barrier. This effect is called the tunnel magneto resistance effect. With the difference in resistance the magnetoresistive effect ratio is defined, see below.

In this thesis, the lower electrode consists only of a single Cobalt layer which is directly sputtered on a semiconducting substrate where a Schottky-barrier is formed. The chosen tunnel bias of the TMR junction is ≈1 V. Electrons, which are injected into the Cobalt electrode, have a certain chance to pass this film without scattering. Due to the fact that those charge carriers do not loose energy in this layer, they can pass the Schottky-barrier subsequently. This non-scattered current fraction is called *ballistic* current.

The chance of an electron to pass the magnetized Cobalt layer without scattering depends on its spin. It has a better chance to pass this film when the spin momentum is aligned parallel to the layer's magnetization than in the other case (antiparallel). For that reason, more electrons with parallel spin than antiparallel polarized are detected at the Schottky-barrier.

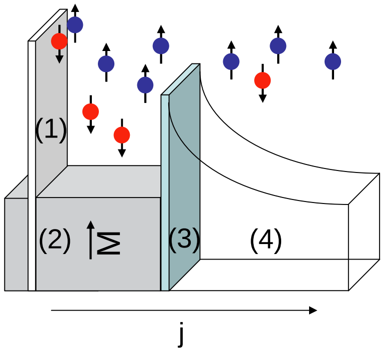

Figure 1: Simplified schematic sketch of the MTJ based experiment: Electrons with both spin states (with 30-50% spin-polarization from the upper ferromagnetic layer) are injected from the tunnel barrier (1) into the lower MTJ base electrode (2). Parallel polarized current fractions have a better chance to pass the Schottky-barrier (3) and enter the semiconductor (4). The total spin-polarization and the magnetoresistive signal is amplified in the base electrode.

If the magnetization of both electrodes is aligned parallel, the majority electrons (with spin parallel to both layers) dominate the tunnel current because of the TMR effect. Due to the fact, that those electrons have a better chance to pass the Cobalt layer without scattering, the spin-polarization of the ballistic current is amplified inside this film.

In case of an antiparallel alignment of the ferromagnetic electrodes the tunnel current is less and only spin-polarized to a small degree. Only small fractions of this current pass the Cobalt and the Schottky-barrier. Consequently the magnetoresistive effect ratio observed in the current which passed the Schottky-barrier is higher than the TMR ratio observed in the tunnel current. The spin-polarization converges to 100% if the Cobalt layer thickness is $\approx$10 nm. Figure 1 shows a simplified sketch of the setup. This experiment is used in this thesis to characterize ballistic currents and to quantify the spin attenuation lengths in Cobalt.

Not only TMR- but also different GMR-effect based junctions have been investigated; the idea of these experiments is mostly analogical.

Therefore the theoretical chapter will address the following topics:

- Magnetoresistive effects and their origins
- Metal/semiconductor interfaces
- Ballistic electrons in metal
- Basics of BEEM
- Ballistic hybrid junctions

Chapter 1

Theory and Basics

1.1 Magnetoresistive Effects

The intensive research on magnetoresistive effects started with the discovery of the antiferromagnetic exchange coupling and the GMR by *Grünberg et al.* [1]. Differing from the use as a simple sensor, GMR based junctions are presented here as spin-filter for ballistic currents.

Most experiments presented in this thesis are based on specialized MTJs [2]. The relevance of the TMR effect versus other magnetoresistive effects emerged with the first two-digit effect ratios measured at ambient temperature [21][22]. For a review of the development before refer to [23].

In general, MTJs are used as prototypes in sensors and MRAM applications nowadays [24]. Combined with modern patterning techniques the potential of MTJs surpasses even that of GMR sensors [25][26]. In contrast to the standard applications the tunnel-barrier is used in this thesis to inject ballistic currents. Details are discussed in section 1.5.2.

1.1.1 Tunnel Magneto Resistance Effect

The Tunnel Effect and Spin-polarized Tunneling

The tunnel effect is one of the early experimental proofs of the quantum theory. E.g. the source of β-rays could be explained as electrons or positrons that tunnel out of an

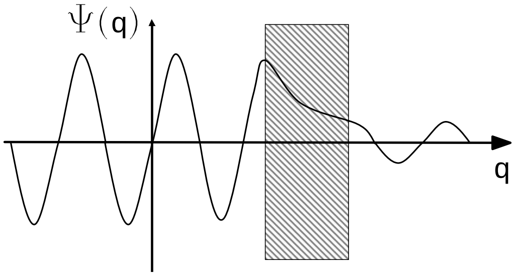

Figure 1.1: The wave function can attain the classical forbidden potential barrier. $\Psi(q)$ has an exponential decay inside the barrier; the wave is attenuated beyond. In thick barriers the wave is evanescent and practically no tunneling occurs.

atomic core. Early theoretical studies about tunneling in solid state structures have been accomplished in the 1930s but it is still topic of current research [27].

In the quantum theory each particle is assigned to a wave function ψ. Using Heisenberg's interpretation of the quantum mechanics, $\psi^2 d^3x$ is the probability to find the particle in a volume element d^3x. This wave can attain areas, usually potential barriers, which are forbidden for a classical particle, see figure 1.1. ψ has an exponential decay in such areas. Tails of the wave function may exist behind the forbidden area. For that reason the probability to find the particle beyond a potential barrier is not zero, in contrast to the classical prediction. This probability is evanescent if the forbidden area is thick.

In MTJs electrons tunnel through insolating barriers. As these barriers are thin films (here: $\approx 1 \ldots 2\,\mathrm{nm}$) a tunnel current, sufficient high for common measurement techniques, can be observed. To explain this tunnel effect of electrons between realistic metals, especially from one transition metal to an other, a closer look to the <u>D</u>ensity <u>O</u>f <u>S</u>tates (DOS) ρ in the metals and the transmission probability matrix element T through the barrier in dependency of the energy E is necessary. A characteristic feature of transition metals is the split d-band, which causes a different DOS for electrons with different spin in the conductance band. The current from electrode 1 to electrode 2 can be written as

$$I_{1,2}(E) = \frac{2\pi e}{\hbar} \int_{-\infty}^{\infty} \rho_1(E) \cdot \rho_2(E + eV) \cdot |T^2(E)| \cdot f(E) \cdot (1 - f(E + eV))dE \quad (1.1.1)$$

f is the Fermi-Dirac function and V the bias voltage at the barrier [28]. The complete current is the difference between $I_{1,2}$ and the current in the opposite direction $I_{2,1}$.

Wentzel, Kramers and *Brillouin* established an approximation, the WKB approximation, to calculate the probability T for a particle to tunnel in dependence of its energy E [29]. This method is a series expansion of $\hbar$ with neglecting terms of higher order than $\hbar^2$.

From this it follows that

$$T(E) \approx \exp\{-\frac{2}{\hbar} \int \sqrt{(2m(\Phi(x) - E_x))}\, dx\}. \tag{1.1.2}$$

m is the mass of the passing particle and Φ is the barrier height. The term under the square root is the effective barrier. It is obvious that high energy particles have a better chance to pass a realistic e.g. gaussian shaped barrier: The thickness is less for those particles.

Tunnel Barriers in Solid State Structures

The preparation of tunnel barriers is in practice a big challenge. In this thesis all tunnel barriers, except those in the BEEM experiments, are magnetron sputtered aluminium films, which are oxidized after sputtering by a microwave plasma. The TMR effect is reliant on a high quality barrier; leak currents and pinholes have to be avoided. For the characterization of these insulating layers some simplifications of the theoretical descriptions are necessary.

The simplest approximation is the *Simmons* fit [30][31]: The barrier is assumed to be rectangular-shaped. The fit can deliver the average barrier height Φ and thickness d, which are the most important parameters.

More detailed is the *Brinkman* fit [32], which is used in this thesis: The barrier is assumed to be trapezoid-shaped. Beside the height and thickness a parameter for the asymmetry $\Delta\phi$ can be obtained. This is important if an electron tunnels from one material to another with different Fermi-energy, see figure 1.2. Brinkman calculated the voltage-dependent tunneling conductance of trapezoidal barriers using two extreme models: the WKB approximation and perfectly sharp boundaries between metal electrode and insulator. Both cases display ”roughly parabolic” conductance/voltage plots for voltages $\lesssim 0.4\,\mathrm{V}$. The term ”roughly parabolic” is explained by Brinkman as follows:

”(...)one immediately recognizes the parabolic nature, in contrast to linear or exponential dependencies which have been observed in some Chromium or doped junctions or at high voltages.”

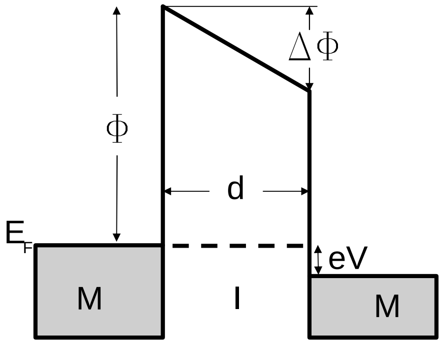

Figure 1.2: Schematic sketch of Brinkman's barrier model at a metal/insulator/metal contact. The barrier is assumed to be trapezoid shaped. Additionally the bias eV is sketched. The barrier thickness d, the barrier height Φ and the asymmetry ΔΦ can be obtained by fitting a quadratic function to the differentiated I/V curve, recorded at a tunnel barrier.

Taking the first terms of the WKB approximation, this quadratic behavior can be confirmed because the conductance can be written as $\frac{dI}{dV} = AV^2 + BV + C$. The demanded barrier data can be obtained by fit parameters A,B and C:

$$\Phi = \frac{eC^2}{32A}\ln^2\left(\frac{h^3}{\sqrt{2}e^3 m_{\mathrm{eff}}}\sqrt{AC}\right) \tag{1.1.3}$$

$$d = \frac{\hbar}{8\sqrt{\Phi m_{\mathrm{eff}}}}\ln\left(\frac{h^3}{\sqrt{2}e^3 m_{\mathrm{eff}}}\sqrt{AC}\right) \tag{1.1.4}$$

$$\Delta\Phi = -\frac{12\hbar\Phi^{\frac{3}{2}}B}{\sqrt{2m_{\mathrm{eff}}}edC}. \tag{1.1.5}$$

m_{eff} is the effective mass (assumed to be 0.4 [33]). In practice an I/V curve is measured, numerically differentiated and fitted by a standard code [34]. In case of tunneling between two ferromagnetic transition metals the magnetization of the layers should be aligned parallel during the I/V measurement. For a closer look, refer to [35].

TMR Effect

Magnetic tunnel junctions consist of two ferromagnetic thin films separated by a thin insulating barrier. In this context "thin" always means the scale of a few nanometers. If a bias voltage is applied between the ferromagnetic layers, the resistance of the tunnel current can be measured. Phenomenologically there is a significant difference in the resistance if the layers are magnetized parallel or antiparallel. Jullière explains this behavior as entirely based on the spin-polarization [2]:

The spin of a tunneling electron is conserved during the tunnel process in a first approximation. A two channel model for majority and minority electrons can be assumed. Both ferromagnetic electrodes have a certain spin-polarization at the interface to the barrier, defined as

$$P = \frac{\rho^{maj} - \rho^{min}}{\rho^{maj} + \rho^{min}}, \tag{1.1.6}$$

where ρ^{maj} is the DOS for the majority, ρ^{min} for the minority electrons, respectively.

In case of parallel magnetization the tunnel current is high. Majority and minority electrons have free states on both sides of the tunnel-barrier in the same quantity. The electrons can tunnel into free states. In antiparallel alignment there are less states for the majority electrons on the other side of the barrier, therefore they cannot tunnel. The total tunnel current is reduced.

So the tunnel currents, resistances respectively, are different in different magnetic alignments. The TMR ratio is defined by the tunnel resistances $R^{\uparrow\downarrow}$ and $R^{\uparrow\uparrow}$ as

$$TMR = \frac{R^{\uparrow\downarrow} - R^{\uparrow\uparrow}}{R^{\uparrow\uparrow}}. \tag{1.1.7}$$

The standardization on the resistance in antiparallel configuration of the magnetic layers is only convention. Jullière used the more pessimistic standardization on the resistance in parallel configuration (often referred as "JMR").

Phenomenological the spin-polarizations of the electrodes also deliver this ratio:

$$TMR = \frac{2P_1P_2}{1 - P_1P_2} \tag{1.1.8}$$

Jullière's model is only an approximate description of the TMR effect. A major weakness of this model is the definition of the spin-polarization in equation 1.1.6 for tunnel experiments. In contrast to Andreev reflection ([36]) or photoemission experiments ([37]) this polarization is no intrinsic attribute of materials. It depends on the transfer matrix of the tunnel-barrier. This matrix can be different for different barrier materials and barrier thicknesses[1].

---

[1] E.g. it is reported that some experiments with Strontium Titanate show a negative TMR-ratio [38].

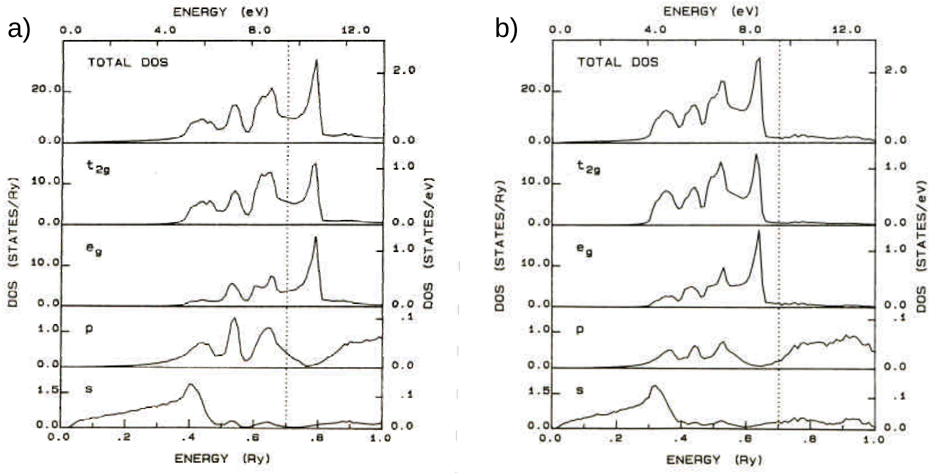

Figure 1.3: DOS for spin states in Cobalt from [39]. Figure a) shows the spin-down DOS, b) the spin-up DOS. The dotted line visualizes the Fermi-energy. The majority- and minority DOS is reversed at the Fermi level: The spin-up DOS is the minority DOS.

A second weakness is an apparent antilogy regarding the DOS in transition metals:

As an approximation the bulk DOS is assumed to be the interface DOS. A closer look to this near the Fermi level shows that in all ferromagnetic 3d transition metals the minority charge carriers' contribution is larger there, see figure 1.3 as an example for Cobalt [39]. Consequently the experimental spin-polarization should be negative.

This antilogy can be resolved as follows: Ferromagnetism relies on 3d-electrons. However the tunneling process is dominated by s-electrons because of their higher effective mass, refer to equation 1.1.2. The TMR effect occurs like Jullière's model predicts with 3d transition metals because these s-band electrons are polarized antiparallel to the 3d band electrons via hybridization [40].

In this thesis only comparatively thick Aluminium oxide barriers are investigated. No negative spin-polarizations have been observed for such stacks. In fact, all measured spin-polarizations of common ferromagnetic materials like Cobalt, Nickel, Iron and alloys of those show a polarization of about 30-50% at low temperatures in this configuration [20][41]. Higher values can be achieved using half-metallic alloys or amorphous metals [42][43].

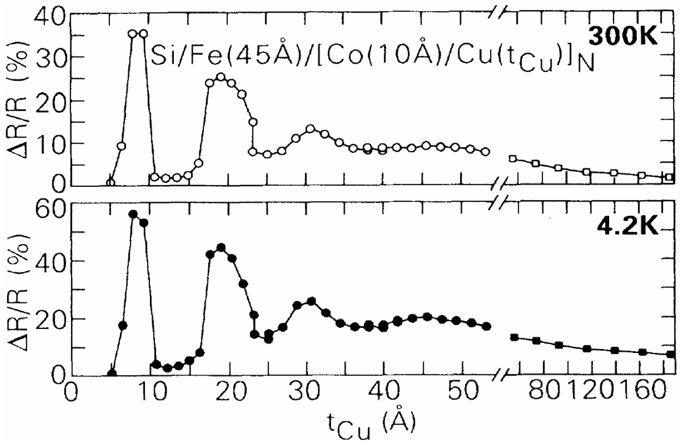

Figure 1.4: Example for the oscillatory behavior or MR-amplitude with varied spacer thickness, from [45]. In this case Cobalt/Copper multilayer stacks have been characterized at ambient and at liquid Helium temperature.

Experimental details of the characterization of magnetic tunnel junctions are presented in chapter 2.2.

1.1.2 Giant Magneto Resistance Effect

Fundamentals

The development of GMR sensors is motivated by the high potential for applications. For instance GMR read head sensors in a hard disk drive are a common application [44]. Nowadays, the areal data density on the disk is increased to ≈50 Gbit/inch^2. This development is inter alia a consequence by the use of GMR-sensors.

When Grünberg *et al.* investigated a Fe/Cr/Fe tri-layer system by Brillouin light scattering they discovered an antiferromagnetic coupling between the ferromagnetic layers over the Chromium spacer [1]. Further examination by *Parkin et al.* showed an oscillatory nature of this phenomenon if the spacer thickness is varied, see figure 1.4. Dependent on the interlayer thickness the coupling can be ferromagnetic or antiferromagnetic and the oscillatory period depends on the non-ferromagnetic material in between [46]. The fundamentals of this phenomenon can be explained with the Rudermann Kittel Kasuya Yosida (RKKY) exchange coupling [47][48]. For a closer look it is necessary to take quantum well states inside the interlayer into account, which are induced by electron reflection at the interfaces [49][50][51]. Details can be found in [52].

The GMR effect occurs in stacks, consisting of thin ferromagnetic layers separated by thin (in practice usually) diamagnetic interlayers. If an external magnetic field forces the ferromagnetic layers to polarize in parallel (in an antiparallel coupled stack) a decrease in the in-plane resistance can be observed [53][54]. This behavior can be explained by the two channel or two current model for electrical transport in ferromagnetic transition metals [55]. For details refer to [56] or [57]. The definition of the GMR ratio is analog to the definition of the TMR ratio in equation 1.1.7.

In general antiferromagnetic coupling between the layers is not necessary to observe the GMR effect. In literature a tri-layer without coupling is often referred to as a *spinvalve*.

Spinvalves

The term ”Spinvalve” is ambiguous in literature, but in general all definitions show a common base:

- Two ferromagnetic thin films are separated by a non-ferromagnetic interlayer.
- The coercive fields of the single layers are different.
- The stack shows GMR effect.

Dieny et al. e.g. used this term for a stack where one of the layers is pinned by the exchange bias of an additional antiferromagnetic layer [58]. This concept is useful for sensor applications: In interlayer exchange coupled GMR multilayer sensors fluctuations of the interlayer thickness can form areas with antiferromagnetic coupling and ferromagnetic coupling. This leads to a decrease of the effect ratio. In exchange bias coupled systems this problem does not occur.

The simplest way to form a spinvalve is to use two different ferromagnetic materials with different coercive fields and separate them with a (comparatively to a usual GMR stack) ”thick” diamagnetic layer, so that approximate no interlayer coupling is present. Copper is the most common spacer due to the good conductance. The use of e.g. Ruthenium is popular, too, due to the excellent coupling properties.

In this thesis spinvalves of the latter type with Copper spacer are investigated, not in Current In Plane (CIP) but in Current Perpendicular to Plane (CPP) geometry (refer to chapter 3 and 4). First CPP measurements have been performed by *Pratt et al.* [59]. Measurements in this geometry usually show a higher GMR ratio than

CIP experiments [60]; however, in contrast to CIP-measurements, it is necessary to pattern the layers; consequently fabrication and measurement are less trivial.

The idea of the perpendicular measurement in this thesis is different to the standard experiment, because not the common *diffusive* charge transport through the layers but the *ballistic* is investigated. The MR-effect observed in the ballistic current has different origins; this is the content of chapter 1.3.2.

1.2 Metal Semiconductor Interfaces

Most modern electronic devices rely on semiconductor technics. Hence semiconductor surfaces and interfaces are a prevalently studied subject in science for more than 130 years. The knowledge of metal/semiconductor contacts goes back to pioneering work of *Braun* who discovered the asymmetrical characteristic of I/V-plots at such interfaces in 1874 [61]. In the early years it was common to compare charge transport phenomena in semiconductor junctions with those in electron tubes. In his famous publication *Schottky* showed the limits of this analogy and formed the first model of the electronic behavior at a semiconductor metal interface, the so called *Schottky-Barrier* [62].

1.2.1 Schottky's Model

The diode at an ideal semiconductor metal interface has been explained by Schottky as follows:

In thermal equilibrium the Fermi levels of the metal and the semiconductor must be aligned at the interface. The difference in work function $e\phi_M = E_{Vac} - E_F$ of the metal and electron affinity χ_{SC} of the semiconductor induces different situations of band bending. When the two materials are brought in contact the compensation of the Fermi levels leads to a charge flow, which causes a dipole layer at the interface. Due to the low charge carrier concentration in semiconductors, which is orders of magnitude less than in metals, shielding is less effective here. In metals the participating charge is screened within the *Thomas-Fermi* screening distance ($d_{TF} \approx 0.5\,\text{Å}$), in semiconductors the space charge extends hundreds of Ångstroms inside [63].

This space charge layer can be either depletion or accumulation. Depletion is generated e.g. if a low work function metal is contacted with a n-type semiconductor. Accumulation can occur e.g. if a high work function metal is brought in contact with a n-type semiconductor.

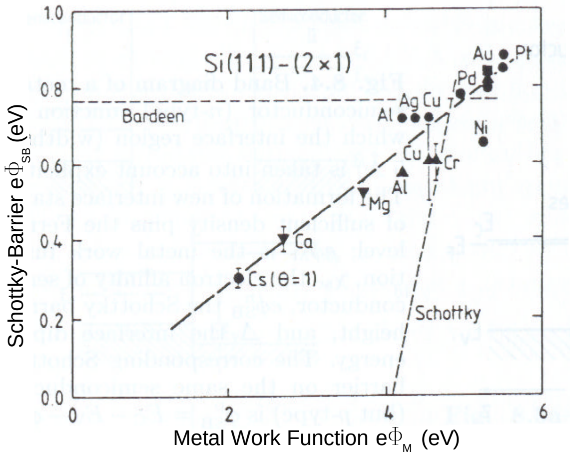

Figure 1.5: Schottky-barrier height versus metal work function, taken from [64]. The data is obtained on cleaved Silicon (111)-(2×1) surfaces. Predictions from Schottky's and Bardeen's model are plotted for comparison. Both models are not adequate to describe the experimental data.

In general *Poisson's* equation 1.2.1 governs band bending $V(x)$ and the form of space charge layers.

$$\frac{d^2V}{dx^2} = -\frac{\rho(x)}{\epsilon\epsilon_o} \tag{1.2.1}$$

Here ρ is the space charge density and ϵ the dielectrical constant. The maximum band bending at the interface is related to the potential barrier an electron has to pass which is excited from the metal into the conduction band of the semiconductor. This is the so called Schottky-barrier Φ_{SB}.

Schottky's model describes the main features of metal/semiconductor diodes; however it is too naive to get deep insight into the phenomena at the interface. According to Schottky a strong variation of Φ_{SB} with the work function is expected; this is not experimentally observed. A comparison between experimental reality and Schottky's prediction is visualized in figure 1.5.

Schottky neglects chemical bonds of metal atoms at the interface to the semiconductor atoms. These bonds induce interface states which influence the barrier notably, even in the ideal case without intermixing of semiconductor and metal atoms.

1.2.2 Models with Interface States

Bardeen improved Schottky's model by implementing interface states between the two materials [65]. His argumentation refers to experimental data of *Meyerhof*, who studied contact potential differences and rectifications for metal point contacts to silicon and germanium [66]. Since the nature of interface states was completely unknown and hard to observe Bardeen assumed that the well known surface states of the semiconductor persist buried under the metal layer. Surface states arise because the periodicity of the crystal is interrupted by the surface and solutions of Schrödinger equation exist which correspond to states in the gap of the semiconductor. The wave function of these states is evanescent, similar to tunneling wave functions. In Bardeen's model semiconductor surface states pin the Fermi level.

The total charge balance consists then of three fractions:

- The charge in the metal Q_M
- The space charge in the semiconductor Q_{SC}
- The charge at the interface (here semiconductor surface, respectively) states Q_{SS}

Charge neutrality of the whole system requires $Q_{SC} = Q_{SS}$ in thermal equilibrium. No net current can flow through the junction then. Figure 1.6 visualizes the band scheme in this model.

It is obvious, that band bending and the Schottky-barrier height are strongly dependent of these additional states, but independent of the metal in this model.

Regarding experimental data it is also obvious that Bardeen's assumption that the interface states can be identified as semiconductor surface states is incorrect. The I/V characteristics of a semiconductor-metal contact are in fact strongly influenced by the metal and its work function, refer to figure 1.5 again. It is the approach of taking interface states what makes Bardeen's model remarkable.

Spicer et al. proposed an alternative model where the Fermi level is pinned by defect levels in the semiconductor gap, the so called Unified Defect Model (UDM) [67] [68] [69], later Advanced UDM (AUDM)[2] [70] [71] [72]. Using photoemission spectroscopy the surface fermi level position of III-V semiconductors (Gallium-Arsenide, Indium-Phosphate and Gallium-Antimony) with less than one monolayer metal and oxygen coverage has been determined experimentally. Spicer found that the Fermi

---

[2] It is called *unified* because it additionally applies to III-V metals and insulators and *advanced* historically after identifying the defect levels.

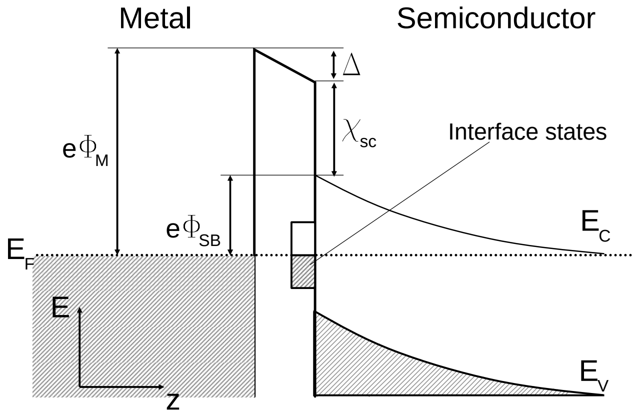

Figure 1.6: Schottky-barrier with interface states (schematic). Φ_M is the metal work function, χ_{SC} the electron affinity of the semiconductor, Δ is the interface dipole energy and Φ_{SB} the Schottky-barrier height.

level is pinned with coverage of 20% metal or ∼1% Oxygen, respectively. For a large range of different metals like Caesium, Indium, Gold, Aluminium and Oxygen the pinning is independent of the metal used; the observed states are an intrinsic parameter of the semiconductor.

For n-type Gallium-Arsenide an electron depletion layer is formed and E_F is pinned at about 0.75 eV above the valence band maximum. In case of p-type Gallium-Arsenide a hole depletion layer is formed and E_F is pinned between 0.4 and 0.5 eV above the valence band maximum. The dominant state is at 0.7 eV and can be associated with a local Arsenide deficit [67]. These states are referred as $\underline{\text{M}}$etal $\underline{\text{I}}$nduced $\underline{\text{G}}$ap $\underline{\text{S}}$tates (MIGS).

The nature of MIGS is complex at non-ideal metal-semiconductor interfaces. The states can be identified as tails of the Bloch function assigned to a state in the metal, which range into the semiconductor [73]: It cannot change abruptly to zero where no electrical states exist in the forbidden band, see a schematic sketch in figure 1.7. The breakdown of periodicity of the Bloch function leads to an exponential decay with imaginary wave vectors in the semiconductor.

In a one-dimensional idealized model, the dispersion curve of the vectors fills the gap of the semiconductor with virtual states, the so called $\underline{\text{V}}$irtual $\underline{\text{I}}$nduced $\underline{\text{G}}$ap $\underline{\text{S}}$tates (VIGS), refer to figure 1.8. As the name suggests not all of these states really

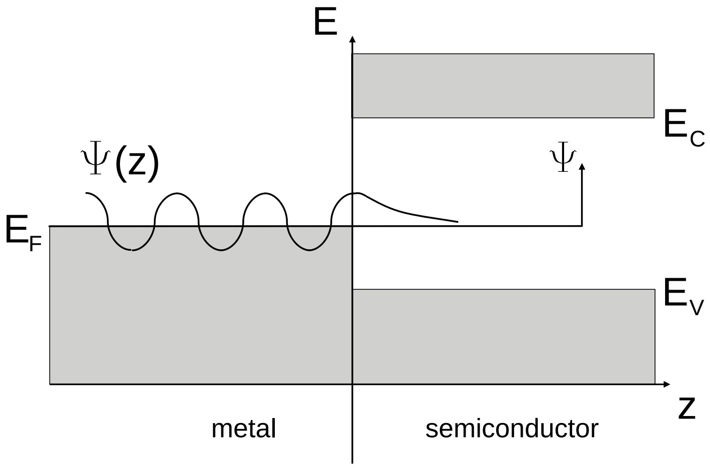

Figure 1.7: Bloch wave ranging inside a semiconductor (qualitatively). $\Psi(z)$ cannot change abruptly to zero in the forbidden zone.

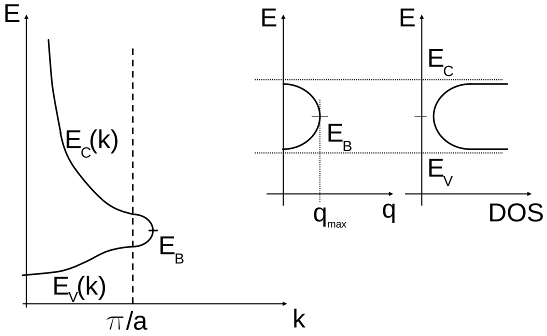

Figure 1.8: One-dimensional model of dispersion curve. The imaginary wave vectors $\kappa = -iq$ fill the gap of the semiconductor until q_{max}. In this model the vectors are symmetric around the branching point. The appropriate DOS in the gap has singularities at E_V (the highest level in the valence band) and E_C (the lowest level in the conductance band).

exist; the existence depends on the default conditions at the interface. The Bloch function of a state in the metal induces VIGS in the semiconductor and their DOS has singularities at E_V and E_C, see figure 1.8. These virtual states can be derived from the band structure. The more donor like states can be separated from the more acceptor like states by the so called branching point E_B, which can be calculated by summation of the bulk states [74][75][76][77].

The branching point E_B is crucial for the understanding of the nature of Schottky-barriers:

- If E_F is below E_B a positive interface charge interacts with the charge carriers.
- If E_F is above E_B a negative interface charge interacts with the charge carriers.

In the first case ionized empty donor states build up the charge, in the second case occupied acceptor states have the analog converse effect. In the one dimensional model visualized in figure 1.8 E_B is in the middle of the gap.

The difference $\delta_{FB} = E_F - E_B$ describes the intra-bond charge transfer due to the interface dipole Δ, which depends on the metal. The complete intra-bond charge transfer can be calculated by the empirical formula of *Pauling et al.* [78]:

$$\Delta q = \frac{0.16}{eV}|\psi_M - \psi_{SC}| + \frac{0.035}{(eV)^2}|\psi_M - \psi_{SC}|^2 \tag{1.2.2}$$

ψ_M and ψ_{SC} are the electro-negativities of the metal and the semiconductor. Due to the fact that $\psi_M \approx 2.0\,eV$ and $\psi_{SC} \approx 1.9 - 2.1\,eV$, the charge transfer can be neglected as a first approximation. In this case it is possible to estimate the Schottky-barrier height from the branching point of the VIGS and the Fermi level. Results of calculations that take Δq into account can be proven clearly experimentally[3] [79] [80] [81]. A strong correlation between the charge neutrality level $(E_B - E_V)$ and the Schottky-barrier height can be observed and used to estimate the branching point [75], refer to figure 1.9.

The existence of VIGS and the corresponding DOS over the whole gap in realistic three-dimensional crystals and ideal interfaces has been derived for several examples [82][83]. In these cases E_B is no more the middle of the gap like in the simplified one-dimensional model; it is dependent on the variety of wave functions contributions from different directions of the Brillouin zone and especially determined by zones with a high DOS.

In most III-V semiconductors, the band structure in the zone center Γ determines the direct gap. It bears little relation to the conductance band as a whole. The small

---

[3] These experiments concentrate on noble metals evaporated on different semiconductors. In case of transition metals the interface is not that perfect, refer to chapter 1.2.3

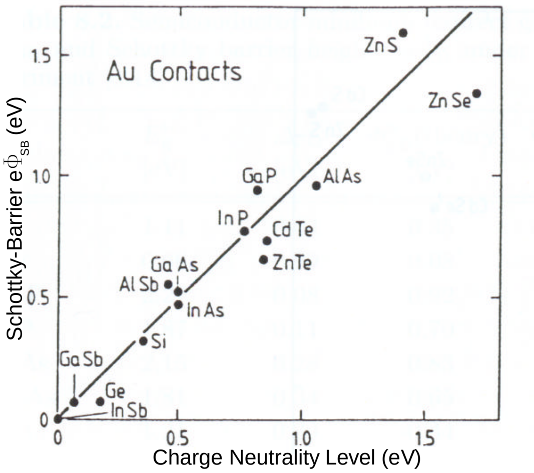

Figure 1.9: Experimental Schottky-barrier heights of Gold contacts to common semiconductor substrates versus the charge neutrality level ($E_B - E_V$), theoretically derived by Tersoff [74], taken from [64].

effective electron mass there induces only little k-space associated with this gap. The effective mass at minima associated with indirect gaps is usually higher; they describe a large region of the conductance band in k-space and are therefore more significant for this band. For that reason the states near indirect minima determine the position of E_B.

More accurate calculations performed by *Tersoff* use an indirect gap which is corrected for spin-orbit splitting Δ_{SO}. This leads to

$$E_B = \frac{1}{2}[\overline{E}_{V,max} + E_{C,min,ind}], \tag{1.2.3}$$

where $E_{C,ind}$ is the indirect conductance band minimum, not located at Γ. $\overline{E}_{V,max}$ is the maximum of the valence band, located at Γ. It is an average value due to spin orbit splitting in Γ. The twofold-degenerate band maximum is pushed up about $\frac{1}{3}\Delta_{SO}$ relative to the threefold-degenerate band with no spin orbit splitting, while the split off state is pushed down $\frac{2}{3}\Delta_{SO}$. Thus the effective maximum is $\overline{E}_V = E_V - \frac{1}{3}\Delta_{SO}$.

The Schottky-barrier height can be estimated from the minimum indirect gap energy $E_{C,ind,min} - E_V$, the interface spin orbit splitting Δ_{SO} and $\delta_{FB} = E_F - E_B$:

$$e \cdot \Phi \approx \frac{(E_{C,ind,min} - E_V - \frac{1}{3}\Delta_{SO})}{2} + \delta_{FB} \tag{1.2.4}$$

	$\delta_{FB} = E_F - E_B$	Δ_{SO}	$\Phi_{SB,theo}$	$\Phi_{SB,exp}$
Si	1.11	0.04	0.35	0.32
Ge	0.66	0.29	0.08	0.07
GaAs	1.81	0.34	0.65	0.52
InAs	1.21	0.39	0.34	0.47
AlAs	2.15	0.28	0.83	0.96
GaP	2.27	0.08	0.92	0.94
InP	1.87	0.11	0.70	0.77
AlSb	1.63	0.70	0.50	0.55
GaSb	0.80	0.75	0.07	0.07

Table 1.1: Schottky-barrier parameters of common semiconductors covered with Gold, experimental and theoretical, all in eV, taken from [74][75][76][77].

The consistency of this approximation is demonstrated in table 1.1, which shows the parameters, calculated and measured, for Gold deposited on common semiconductor substrates.

1.2.3 Chemistry Dependent Models

Film growth studies show that interfaces between semiconductors and metals are not as ideal as the VIGS and MIGS model suppose. Chemical reactions and structural changes like interdiffusion are not included in these models. Using Low Energy Electron Diffraction (LEED) spectroscopy a dependence of Schottky-barrier height on chemical reactivity can be detected [84].

Especially the interface between III-V semiconductors and transition metals is strongly reactive [85][86]. Hence a specialized model for this case has been developed by *Ludeke* and *Landgren* [87]. It is based on experimental data from X-ray photoemission spectra of Gallium Arsenide (110) and Gallium Antimonide (110) surfaces, covered with several transition metals. The common ground and quintessence of all these investigation is interdiffusion and compound formation of these metals with the substrate. Comparing e.g. deposited Titanium and Palladium layers on Gallium Arsenide indicates strong exchange-type reaction but shows remarkable differences in the Fermi level position, which is not conform to the AUDM [88]. Figure 1.10 shows exemplarily the decompositions of the Gallium and the Arsenide 3d-surface levels for different coverage of Titanium and Palladium.

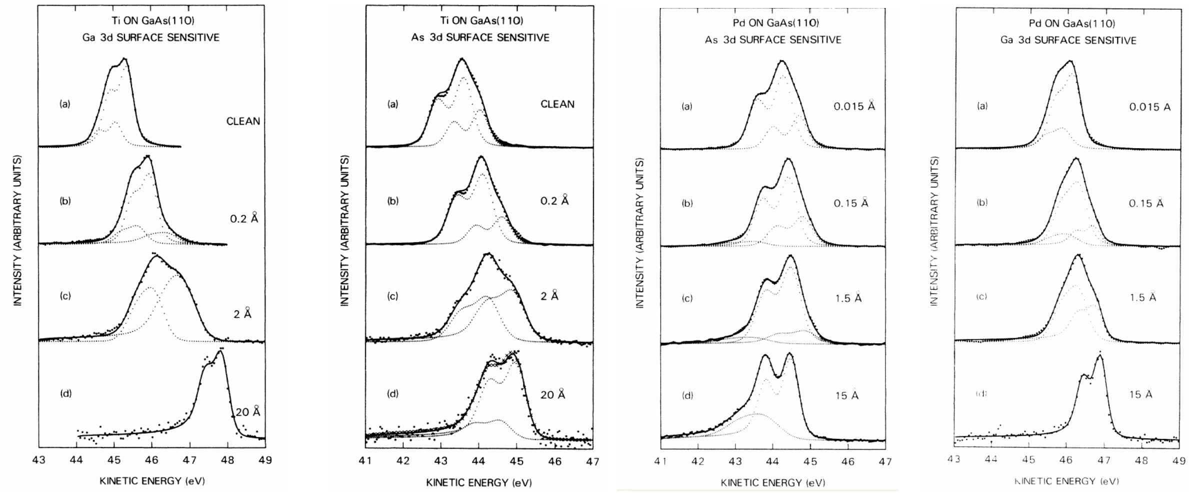

Figure 1.10: Decompositions of 3d surface level of Gallium and Arsenide for different coverages with Titanium and Palladium, indicated in the sketch [88]). These spectra have been measured by X-ray photoemission. The larger dots are experimental data. The small dotted lines are the single kinetic energy components fitted by a *Doniach-Sunjic* line shape [89]. The sum of the components is displayed by the solid line.

The experimental data can be explained by the *mixed interface Schottky model*, also called *effective work function model* by *Freeouf* and *Woodall* [90][91]. The chemistry of the new compound at the interface forms the basis of this theoretical approach. It suggests that the Fermi level is not pinned by surface states. It is "...related to the work functions of microclusters of the one or more interface phases resulting from either oxygen contamination or metal-semiconductor reactions which occur during metallization" [91].

All these models are important for the theoretical understanding of real interfaces and Fermi-pinning, but for predictions of Schottky-barrier heights and other interface parameters detailed information about roughness and metallurgy of the interface is necessary. Such conditions are mostly not given in practice. Investigations on the interface chemistry are difficult to perform in realistic stacks. For that reason it is nearly impossible to predict real Schottky parameters of barriers between transition metals to III-V semiconductors by theoretical calculations.

It is necessary to note at this point that for perfect Schottky-barrier preparation (which is necessary for fundamental investigations on semiconductor/metal interfaces) the substrate is cleaved under UHV conditions, so that no oxide is on the surface before the deposition of the metal. For a review of practical techniques refer to e.g. [64] or [63].

In this thesis such conditions are not fulfilled. The Schottky-barriers are by far not perfect and fortunately this sophisticated preparation is not necessary. The Gallium Arsenide wafer is etched by hydro-carbonic acid to remove the oxide and subsequently put into UHV. Annealing under vacuum condition to remove the hydrogen termination is set aside, for details refer to chapter 2.1.1. As seen in the experiments this is sufficient for ballistic electron experiments.

1.2.4 Electrical Characterization of Schottky-Barriers

The electrical characterization of Schottky-barrier parameters by performing I/V curve measurements is the most common method for comparison to others[4]. For that purpose, an ohmic contact is prepared at the semiconductor. If no bias is applied, electrons can pass the barrier only by tunneling and by their thermic kinetic energy. As an approximation only the current density in perpendicular direction to the interface of the Schottky-barrier j_z can be taken into account, first from the metal to the semiconductor:

$$j_z^{M \mapsto S} = \int_{E_F + e\Phi_{SB}}^{\infty} e \cdot v_z \cdot D_C(E) \cdot f(E) dE, \tag{1.2.5}$$

where v_z is the velocity component in z-direction, $f(E)$ the Boltzmann distribution and $D_C(E)$ the DOS in the conductance band. The bias is contained implicit in v_z in this formula.

A square root dependency of the DOS can be assumed as an approximation, thus $D_C(E) \sim \sqrt{E - E_C}$, where $E - E_C$ is the kinetic energy of an electron in the conduction band. The current density $j_z^{M \mapsto S}$ from the metal to the semiconductor can be estimated as:

$$j_z^{M \mapsto S} = A^* \cdot T^2 \cdot \exp \frac{-e\Phi_{SB}}{k_B \cdot T} \exp \frac{eV}{k_B T} \tag{1.2.6}$$

$A^* = 4\pi m^* k_B^2 / h^3$ is the Richardson constant, T the temperature and k_B the Boltzmann constant. For free electrons the effective mass of the electrons is $m^* = m_0$ and $A^* = 120\, A/(cm^2 K^2)$.

---

[4] Photoemission experiments are used e.g. for more fundamental research on semiconductor/metal interfaces [88].

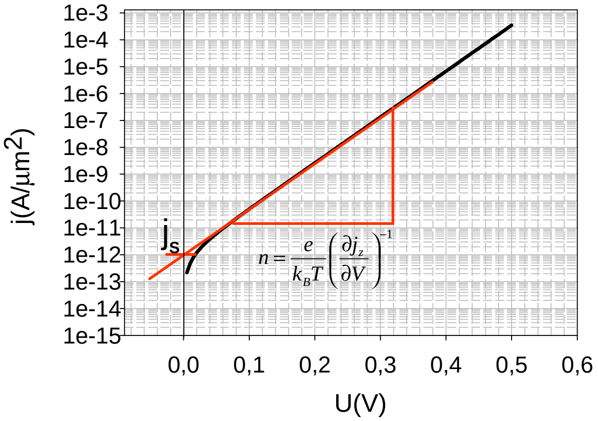

Figure 1.11: Forward current density of the I/V Schottky-diode characteristic, plotted logarithmically. The graph has been calculated for $n = 1$ and $j_s = 1\,pA/\mu m^2$ at room temperature with equation 1.2.8. The Schottky-barrier parameters n and j_s can be reobtained from the (extended) linear part of the graph: The slope delivers n and the zero-crossing current density is j_s. Additionally Φ_{SB} can be calculated exemplary from j_s with equation 1.2.9 as $\Phi_{SB} \approx 0.8\,eV$.

The current density in the opposite direction from the semiconductor to the metal can be estimated as:

$$j_z^{S\mapsto M} = -A^* \cdot T^2 \cdot \exp\frac{-e\Phi_{SB}}{k_B \cdot T} \tag{1.2.7}$$

From this it follows that the total thermionic current density is:

$$j_z^{S\leftrightarrow M} = j_s[\exp(eV/k_BT) - 1] \tag{1.2.8}$$

where

$$j_s = A^*T^2\exp(-e\Phi_{SB}/k_BT) \tag{1.2.9}$$

is the saturation current density. j_s can be fitted from a logarithmical plot of the current density to the bias in forward direction; the Schottky-barrier height can be determined from this, see figure 1.11.

For practical reasons an ideality factor n can be included in this equation, to quantify the non-ideal behavior of an experimentally obtained Schottky-barrier:

$$j_s = A^*T^2\exp(-e\Phi_{SB}/nk_BT) \tag{1.2.10}$$

This n can be written as:

$$n = [1 + \frac{\partial \Delta\Phi}{\partial V} + \frac{k_B \cdot T}{e} \frac{\partial(\ln A^{**})}{\partial V}]^{-1} \tag{1.2.11}$$

The meanings of the three single summands in equation 1.2.11 are:

1. 1 for ideal behavior
2. $\frac{\partial \Delta\Phi}{\partial V}$ is the bias dependence of the barrier correction $\Delta\Phi$ due to combined effects of image force and applied field
3. Term to take tunneling contributions, recombination effects and trapping at interface states into account[5]

In the ideal case, the second and third summand of equation 1.2.11 are zero[6]. To gain n from experimental data, it is necessary to determine the slope of the linear part of figure 1.11 in forward direction:

$$n = \frac{e}{k_B T} \frac{dV}{d(\ln j_z)} \tag{1.2.12}$$

for $V > \frac{3 k_B T}{e}$. It is obvious that reasonable values for the barrier height can only be obtained for $n \approx 1$ because j_s cannot be quantified accurately otherwise.

n can also be obtained for $V < \frac{3 k_B T}{e}$ and reverse bias with the more general formula 1.2.13:

$$n^{-1} = \frac{k_B T}{e} \frac{\partial}{\partial V} ln[j_z/(1 - e^{\frac{-eV}{k_B T}})] \tag{1.2.13}$$

One should note that the ideality factor is in fact a function of the bias and can only be specified for a particular operating point. The practical procedure, using equation 1.2.12, is a common approximation for the evaluation of the Schottky-contact. For a review on the theory of metal/semiconductor contacts and the characterization of Schottky junctions refer to [63].

---

[5] This term contains the generalized Richardson constant $A^{**} = p_P p_Q \frac{a^*}{1 + p_P p_Q v_r / v_d}$. Here p_P is the probability of electron emission over the potential barrier into the metal without electron-optical-phonon backscattering. p_Q is the ratio of the current flow *with* tunneling and quantum-mechanical reflection to the current flow *without* these effects, v_r is the recombination velocity and v_d the diffusion velocity from thermionic emission. The effective Richardson constant is in practice dependent on the bias, due to the current's tunneling contributions and recombinations with interface states.

[6] The best ideality factor to be found in realistic experiments is $n \approx 1.01 - 1.02$; the "non-ideal" effects never disappear completely [63].

1.3 Ballistic Electrons in Transition Metals

1.3.1 Diffusive and Ballistic Transport

Historically *Drude's free electron gas theory* comprehends inter alia the assumption that resistivity of metals is a consequence of electron scattering at atomic cores [92] [93]. This model was improved by *Mott*[7]: Charge transport in realistic extended crystal is always limited by scattering of electrons (holes, respectively) at phonons, impurities, lattice imperfections and other electrons [9], except in superconducting materials. The latter effect is of particular importance in ferromagnetic metals. Scattering at atomic cores makes no contribution to the resistance. In transition metals electron-electron scattering occurs in two processes according to Mott:

1. Direct scattering of two electrons near the Fermi-surface. For spherical Fermi surfaces this makes no contribution to the conductivity, but for non-spherical Fermi-surfaces a term in the resistance $\sim T^2$ arises, particularly large for transition metals.

2. At low temperatures in ferromagnetic metals, a term in the resistance appears due to scattering of conduction electrons by spin waves $\sim T^2$. At high temperatures a term for spin disorder becomes more important.

When an electric field is applied, the random walk of the charge carriers gets a preference direction. Technically the current direction is defined opposite to the mean electron flow. The mean free path λ of an electron with Fermi speed, according to different experiments, in most metals at room temperature about 5 to 100 Å[94]. The usual electron transport, dominated by scattered charge carriers, is called *diffusive*.

An electron injected into a solid state structure with a certain energy above the Fermi level has a limited chance to pass it without scattering, depending at first on the length of the path which it has to pass inside the metal and secondary on intrinsic parameters of the material and thirdly on the energy. This *ballistic* electron, a ballistic current, respectively, can be used for several investigations. Especially in nanometer-scale patterned structures and thin films ballistic currents can be observed due to the short ways, e.g. in MTJs and spinvalves measured in CPP geometry.

---

[7] Nobel Prize in Physics 1977 "for ... fundamental theoretical investigations of the electronic structure of magnetic and disordered systems"

1.3.2 Spin Attenuation Lengths and Ballistic Magneto Current

Origins of the Spin Dependent Electron Transport in Transition Metals

The general interest in measuring electron attenuation lengths came up with Drude's theory of electronic transport. Lots of experimental results for different metals can be found in literature, e.g. the pioneer work of *Fuchs* and *Sondheimer* [95][96]. These works concentrate on measurements of the conductance of thin films and thin wires [97].

The essential modification in the interpretation of such experiments on transition metals came up with the band theory:

> With use of the band theory, Mott anticipated that in transition metals the scattering from s- to d-bands dominates electronic transport [9]. Though the d-band in ferromagnetic elements is spin split, the attenuation length must be spin-dependent.

First experimental investigations on electron spin-polarization in ferromagnetic materials have been accomplished by LEED on Nickel surfaces [98]. The diffracted intensities of a spin-polarized electron beam is dependent on the magnetization of the sample. Furthermore photoemission experiments show an asymmetric behavior for the spin-polarization on ferromagnetic surfaces [99]. Based on these results, first calculations concerning the energy dependence of spin attenuation lengths have been carried out [100]. These works concentrate on larger electron energies than in this thesis.

Campbell and *Fert* verified Mott's hypothesis in dilute binary and ternary ferromagnetic alloys but were unable to quantify the lengths in the first experiments [55]. This has been accomplished again by Fert and several other groups using GMR junctions more than 50 years after Mott's prediction.

First illustrations of the GMR effect took mainly interfacial spin dependent scattering into account. More detailed studies introduced spin-dependent bulk scattering [101]. The associated attenuation lengths have been quantified in specialized spinvalve stacks [5][6][7][8]. The experimental setups are sketched in chapter 3.1.3.

Various alternative techniques have been used to investigate spin-dependent electron transport:

- Spin-resolved photoemission [102][103][104]
- Time and spin-resolved two-photon photoemission [105]

- Spin-resolved electron transmission [106][107]
- BEEM (see below) [94][108][109][110]
- SVT (see below) [111]

The approach accomplished in this thesis is related to the two latter prompts.

The transport in transition metals can be explained using Matthiessens' rule [112]:

$$\lambda_{\uparrow\uparrow}^{-1} = \lambda_{\uparrow\uparrow,e/h}^{-1} + \lambda_{\uparrow\uparrow,e/e}^{-1} + \lambda_{\uparrow\uparrow,phonon}^{-1} + \lambda_{\uparrow\uparrow,th.SWabs.}^{-1} \tag{1.3.1}$$

$$\lambda_{\uparrow\downarrow}^{-1} = \lambda_{\uparrow\downarrow,e/h}^{-1} + \lambda_{\uparrow\downarrow,e/e}^{-1} + \lambda_{\uparrow\downarrow,phonon}^{-1} + \lambda_{\uparrow\downarrow,th.SWem.}^{-1} + \lambda_{\uparrow\downarrow,SSWem.}^{-1} \tag{1.3.2}$$

$\lambda_{e/h}$, $\lambda_{e/e}$ and λ_{phonon} are attenuation length terms that take electron-hole, electron-electron and electron-phonon scattering into account. Additionally terms for emission ($\lambda_{\uparrow\downarrow,th.SWem.}$) and absorption ($\lambda_{\uparrow\uparrow,th.SWabs.}$) of thermal spinwaves are implemented. Equation 1.3.2 contains an extra term for spontaneous spinwave emission. Only majority spin electrons can absorb and only minority spin electrons may emit spinwaves due to the conservation of angular momentum. Theory predicts that the minority spin attenuation length is dominated by the $\lambda_{min,SSWem.}$ term [113][114]. A detailed experimental investigation of spinwave terms can be found in [112].

Ballistic Current Attenuation and BMC-Ratio

In general the decay of a non-polarized ballistic current inside a non-magnetic material, dependent on the distance d, can be written as

$$I(d) = I_0 \cdot e^{-t/\lambda}. \tag{1.3.3}$$

I_0 is the original current, the emitter current, respectively. λ is the attenuation length of the ballistic current. This parameter is dependent on the crossed material and the energy of the injected charge carriers. Scattered electrons loose energy and are no more called ballistic.

If the current is injected into a ferromagnetic metal, equation 1.3.3 has to be modified. The spin-dependent mean free paths have to be implemented. Similar to GMR and TMR explanations a common approach is the use of two independent channels for the two possible spin states. The result is equation 1.3.4:

$$I(d) = I_0 \cdot [0.5 \cdot e^{-t/\lambda_{\uparrow\uparrow}} + 0.5 \cdot e^{-t/\lambda_{\uparrow\downarrow}}]. \tag{1.3.4}$$

$\lambda_{\uparrow\uparrow}$ and $\lambda_{\uparrow\downarrow}$ are the different attenuation lengths for majority electrons and minority electrons.

The experiments in chapter 3.1 demand a special estimation: The injected current is polarized. For that reason the spin-polarization P_E has to be implemented in equation 1.3.4. Furthermore a case differentiation is necessary. In case the current is injected from another ferromagnetic metal the magnetization alignment of both metals affects the resulting current. This leads to the general equation 1.3.5 for the ballistic current $I_{\uparrow\uparrow}$ and $I_{\uparrow\downarrow}$ in case of parallel and antiparallel magnetization in magnetic tunnel junctions:

$$I_{\uparrow\uparrow(\uparrow\downarrow)}(d) = I_0(0,5+0,5P_E)e^{-t/\lambda_{\uparrow\uparrow(\uparrow\downarrow)}} + I_0(0,5-0,5P_E)e^{-t/\lambda_{\uparrow\downarrow(\uparrow\uparrow)}}. \tag{1.3.5}$$

In principle, it is possible to derive spin attenuation lengths with this equation just by measuring the current for both cases when the precondition of known spin-polarizations and layer thickness is given. Practically this measurement is not trivial. The ballistic current must be separated from the diffusive. In this thesis this is done by injection of electrons with energy $E \gtrsim 1$eV over a tunnel potential barrier and subsequent energy-filtering of scattered electrons by a Schottky-barrier. The Schottky interface metal is grounded to avoid electrical charging. Obviously the spin-polarization of the ballistic current is rising with increasing passed path. The Schottky-barrier requires the implementation of a transmission coefficient T to equation 1.3.5 [10]:

$$I_{\uparrow\uparrow(\uparrow\downarrow)}(d) = I_0(0,5+0,5P_E)e^{-t/\lambda_{\uparrow\uparrow(\uparrow\downarrow)}}T_{\uparrow\uparrow(\uparrow\downarrow)} + I_0(0,5-0,5P_E)e^{-t/\lambda_{\uparrow\downarrow(\uparrow\uparrow)}}T_{\uparrow\downarrow(\uparrow\uparrow)}. \tag{1.3.6}$$

T is considered to be spin dependent here. It is the theoretical transmission through the barrier in a junction with 0 nm base thickness. For some heterostructures , slight spin-filtering effects have been predicted, but this is neglected here [115][116].

In chapter 3.2 and 4, the estimations for the current have to be modified for the special cases of different stacks with and without polarization of the injected current. In practice the ratio of collector-current to emitter-current I_C/I_0 is plotted versus different base layer thicknesses t to get λ from a fit.

As a result from the spin filtering effect in ferromagnetic thin films, it is possible to define a new magnetoresistance e.g. in TMR stacks. For apparent physical reasons this phenomenon is not called "magnetoresistance" but "magneto current" in the following. The definition of the <u>B</u>allistic <u>M</u>agneto <u>C</u>urrent ratio (BMC) is analog to the definition of the TMR ratio in equation 1.1.7:

$$BMC = \frac{I^{\uparrow\uparrow} - I^{\uparrow\downarrow}}{I^{\uparrow\downarrow}}. \tag{1.3.7}$$

Due to the fact that no bias is applied at the Schottky-barrier not the resistances but the ballistic currents are used for this definition.

1.4 Ballistic Electron Emission Microscopy

1.4.1 Scanning Tunnel Microscopy

One of the most powerful tools to observe the electronic structure of conducting surfaces is the Scanning Tunnel Microscope (STM). It has been developed by *Binning* and *Rohrer* [117][118] during the 1980s[8]. Due to its simple setup (consisting in principle of some Piezo electric ceramics, a tip and a high quality current measurement device) and its high performance, inexpensive commercial devices and also construction kits are available.

In principle, a STM works as follows: A metallic tip, in practice usually a sharpened Tungsten wire, scans over the conducting surface of the sample. The distance between tip and surface is about 1 nm. A bias voltage, applied between sample and tip, generates a tunnel current which can be measured. As explained in chapter 1.1.1 this current is extremely dependent on the distance d the electrons have to tunnel, namely $\mathrm{I} \sim e^{-d/d_0}$. As a rule of thumb, it is possible to assume that one Ångstrom difference in distance is one order of magnitude difference in the current.

The resolution is in first approximation only dependent on the tip's shape. A Tungsten filament cut by wire cutting pliers can possibly deliver sub-atomic resolution but more complex tip preparation processes lead to a better chance for sharp tips. First atomic resolution STM pictures have been published only months after the pioneering publication [119].

There are two modes to operate the STM:

- Keeping the tip in a constant level over the sample (*constant-height mode*)
- Keeping the current constant (*constant-current mode*)

In case of an electronically homogenous surface, constant-current mode means essentially constant distance d to the surface. Characterizing inhomogenous surfaces, the topography and the electronic structure of the surface can indeed be obtained very exactly, but not properly be separated[9].

Keeping the height over the sample constant enables quick measurements but should only be performed at extremely smooth surfaces. An unevenness could damage or change the shape of the tip in this operation mode.

---

[8] Nobel prize in Physics 1986 "…for their design of the scanning tunneling microscope"

[9] This is an essential equivocality in all STM pictures: The topography and the electronic structure of the observed sample can never be separated *in situ*. Only additional information can clarify if e.g. an experimental unevenness on a smooth surface is a topographic imperfection or an atom with different electronic properties. Spectroscopy can differentiate this but is very time intensive. For that reason it is a common technique to scan the same area two times with different tunnel bias [120].

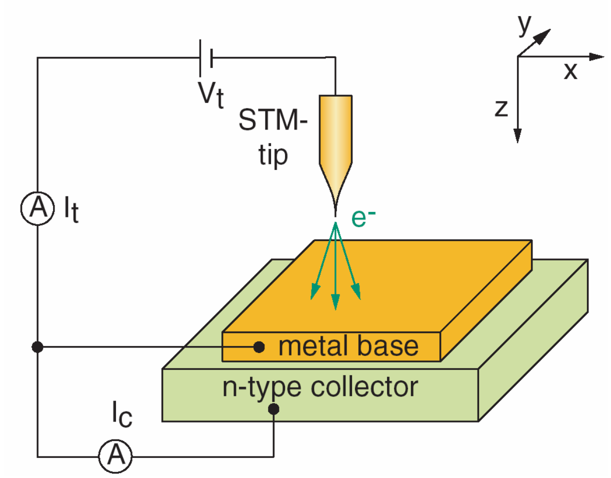

Figure 1.12: Schematic setup of a ballistic electron emission microscope [125]. Additionally to the STM current I_t, the ballistic current I_C into the substrate is recorded simultaneously.

A detailed description and review of tunnel microscopy can be found in [121] and [122].

1.4.2 BEEM

To observe samples consisting of a thin film on a semiconductor surface, a STM can be upgraded to a three terminal device called Ballistic Electron Emission Microscope (BEEM). This apparatus has been build and published first by *Kaiser* and *Bell* in 1988 [12][123][124]. For BEEM experiments, additionally to the tip/surface current, the ballistic current into the semiconductor is measured. Schottky-barrier parameters can be measured by tunnel-current/voltage spectroscopy; this makes direct imaging of subsurface interface properties with sub-nanometer resolution possible, the Schottky-barrier is mapped. Furthermore comparing topography scan and the simultaneous recorded ballistic scan allows the identification of measurement artifacts. The schematic setup is shown in figure 1.12.

In this thesis special magnetoresistive stacks, namely spinvalves, are investigated by BEEM. Setups like these are also referred in the literature as Ballistic Electron Magnetic Microscope (BEMM) or Ballistic Electron Emission Spectroscope (BEES)

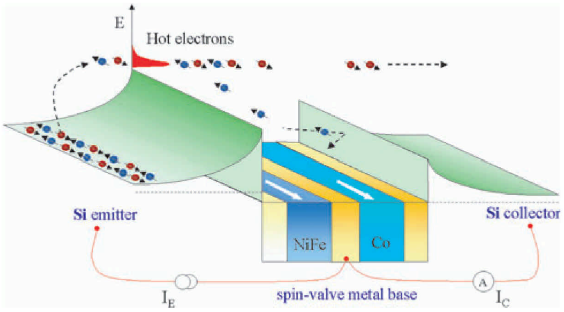

Figure 1.13: The SVT schematic from [129]. The spinvalve is embedded between two Schottky-barriers. Scattered electrons do not pass the second barrier.

[108][126]. It is possible to map magnetic domains in nanometer scale using the ballistic current [127].

A detailed description of the BEEM used and the experiment itself can be found in chapter 4.3.

1.5 MR-junction/Schottky Hybrid Junctions

1.5.1 Spinvalve Transistors

The first experimental solid state structure, based on the transport of non-equilibrium hot electrons rather than on Fermi electrons, has been the Spinvalve Transistor (SVT) by *Lodder et al.*, introduced in 1995 [111][128]. This device consists of a spinvalve installed between two semiconductors and thus two Schottky-barriers. The Schottky-contacts are made with noble metals like Gold and Platinum. One semiconductor is the emitter, the metallic spinvalve is the base and the second semiconductor is the collector of this transistor. The current is measured in CPP geometry. Figure 1.13 is a sketch of the experimental setup.

The idea is to filter the electrons by their spin as explained in chapter 1.3.2. Electrons scattered inside the spinvalve will not be able to pass the Schottky-barrier due to the energy loss. If both layers are magnetized parallel, the electrons polarized antiparallel to them are filtered because of their shorter attenuation length in both layers. In case of an antiparallel alignment, all electrons are filtered in one of the layers. The total current is reduced drastically compared to that in parallel alignment.

The SVT's maximum experimental MR ratio of about 400% at room temperature is exceptionally high [130].

Lodder's SVT is the first experimental proof for ballistic electron effects in a magnetoresistive spintronic setup. However the fabrication is challenging: The two Schottky-barrier assembly can only be manufactured by wafer bonding under UHV conditions. Furthermore the stack of a spinvalve plus the noble contacts to the semiconductor is thick in the dimension of ballistic electron experiments. For that reason the collector currents are usually small; with special setups and slightly biased collector electrode an effect ratio of 400% and an output current of $40\,\mu A$ could be measured recently [130].

For a recent review on this topic refer to [131].

1.5.2 TMR/Schottky Hybrid Junctions

TMR/Schottky hybrid systems consist of a magnetic tunnel junction on a semiconductor substrate. The lower electrode, the base, is deposited directly on the substrate without any buffer layers. Spin-polarized ballistic electrons are injected from the upper electrode of a MTJ, the emitter, into the lower electrode, the base; ballistic electrons are filtered to their spin and fractions get non-scattered into the semiconductor, the collector, see chapter 1.3.2. The first important advantage of this setup, compared to the SVT, is the possibly thin base which enables higher ballistic currents. The second advantage is the comparatively easy fabrication which is based on standard deposition techniques. The currents in parallel and antiparallel alignment of the magnetization in a hybrid stack can be calculated from equation 1.3.6 in chapter 1.3.2. Using equation 1.3.7 the spin attenuation lengths can be estimated from collector current data of an assembly of junctions with varied base layer thicknesses. In general the BMC ratio is lower than in SVT systems because only a single layer filters the ballistic electrons.

This BMC ratio is not obligatory dependent of the TMR ratio value. The TMR ratio is high if the spin-polarization at the interfaces of the tunnel-barrier is high and the tunnel-barrier itself has no short circuits. The BMC ratio depends primarily on the attenuation lengths and the perfect parallel and antiparallel aligned electrodes.

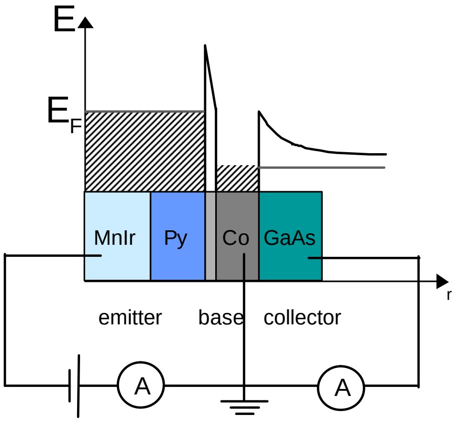

Figure 1.14: TMR/Schottky-barrier hybrid junction (schematic). The ferromagnetic electrodes are a Permalloy (NiFe 80/20) and a Cobalt layer. In contrast to Lodder's measurement no second bias is applied between Schottky-barrier and lower ferromagnetic MTJ electrode.

1.5.3 Tunnel-Barrier/Spinvalve/Schottky-Barrier Hybrid Junctions

A composition of TMR/Schottky hybrid and SVT is achieved by replacing one Schottky-barrier of the SVT by a tunnel barrier [132] [133]. This junction is referred to Magnetic Tunnel Transistor (MTT). The BMC ratio of the SVT is conserved or even better and the fabrication is comparatively easy. Parkin *et al.* report a BMC ratio of 3400%[10] [133]. Furthermore, a spin-polarized current can easily be injected into the spinvalve by deposition of a ferromagnetic metal on the tunnel-barrier, just like in a magnetic tunnel junction.

To calculate the BMC ratio equation 1.3.4 has to be extended by inserting new terms for the three layers, where the non-magnetic term can be cancelled and both currents must be inserted in equation 1.3.7.

---

[10] This value is commented by Lodder as not to be comparable with SVT effect ratios due to the comparatively low transfer ratio ($\approx 10^{-7}$)[134]. In practice MTT and SVT junctions are often additionally biased between base and collector to optimize the electrical specifications. Transfer ratio and effect ratio can be balanced this way. Rising the effect ratio affects the signal to noise ratio negatively. Especially for sensor applications balancing may be useful, because not a high effect ratio but a good signal to noise ratio and high collector currents are desired in this case.

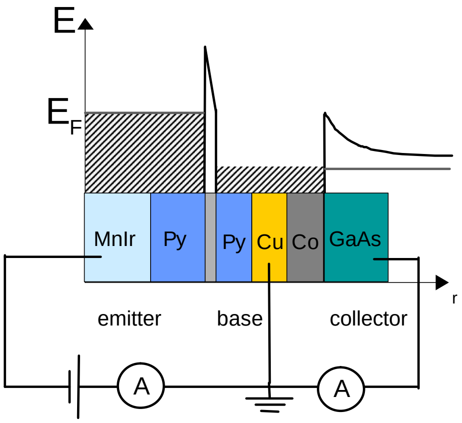

Figure 1.15: Tunnel-junction/Spinvalve/Schottky-barrier hybrid setup with spinpolarized injection from a pinned Permalloy layer schematic.

In case of a Cobalt/Permalloy spinvalve the BMC ratio can be written as:

$$\begin{aligned} BMC = {} & [[I_0 \cdot 0.5 \cdot e^{-d_{Co}/\lambda_{\upuparrows Co}} \cdot e^{-d_{Py}/\lambda_{\upuparrows Py}} + I_0 \cdot 0.5 \cdot e^{-d_{Co}/\lambda_{\uparrow\downarrow Co}} e^{-d_{Py}/\lambda_{\uparrow\downarrow Py}}] \\ & -[I_0 \cdot 0.5 \cdot e^{-d_{Co}/\lambda_{\upuparrows Co}} \cdot e^{-d_{Py}/\lambda_{\uparrow\downarrow Py}} + I_0 \cdot 0.5 \cdot e^{-d_{Co}/\lambda_{\uparrow\downarrow Co}} \cdot e^{-d_{Py}/\lambda_{\upuparrows Py}}]] \\ & /[I_0 \cdot 0.5 \cdot e^{-d_{Co}/\lambda_{\upuparrows Co}} \cdot e^{-d_{Py}/\lambda_{\uparrow\downarrow Py}} + I_0 \cdot 0.5 \cdot e^{-d_{Co}/\lambda_{\uparrow\downarrow Co}} \cdot e^{-d_{Py}/\lambda_{\upuparrows Py}}] \\ = {} & \frac{[e^{-d_{Co}/\lambda_{\upuparrows Co}} \cdot e^{-d_{Py}/\lambda_{\upuparrows Py}} + e^{-d_{Co}/\lambda_{\uparrow\downarrow Co}} e^{-d_{Py}/\lambda_{\uparrow\downarrow Py}}]}{[e^{-d_{Co}/\lambda_{\upuparrows Co}} \cdot e^{-d_{Py}/\lambda_{\uparrow\downarrow Py}} + e^{-d_{Co}/\lambda_{\uparrow\downarrow Co}} \cdot e^{-d_{Py}/\lambda_{\upuparrows Py}}]} - 1. \end{aligned} \quad (1.5.1)$$

In case of spin-polarized injection from another ferromagnetic layer or (possibly) by a magnetized STM tip into the spinvalve, this estimation has to be modified. Again the 0.5 terms have to be replaced by terms containing the emitter spin-polarization P_E. The maximum ratio is determined by the states with minimum and maximum ballistic current, assuming that both magnetic spinvalve layers have approximately the same filtering effect. If this precondition is not given, e.g. one layer is much thicker than the other, it is necessary to derive this special case differently. As a visualization figure 1.15 is considered as an example. If the unpinned Permalloy layer between tunnel-barrier and Copper is antiparallel to both other layers, the ballistic current is minimal. The highest ballistic current is estimated in case of all layers are

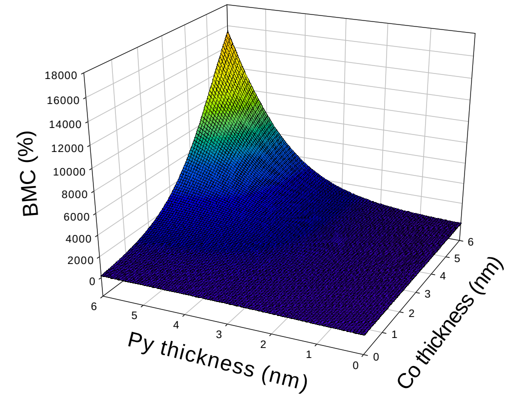

Figure 1.16: Visualization of equation 1.5.2. The BMC-ratio is plotted versus the layer thicknesses for Cobalt and Permalloy. The spin-polarization of the injected current is estimated to be 50%. The assumed attenuation lengths are $\lambda_{\uparrow\uparrow Co} = 6.0\,\mathrm{nm}$ and $\lambda_{\uparrow\downarrow Co} = 1.0\,\mathrm{nm}$ for Cobalt and $\lambda_{\uparrow\uparrow Py} = 5.04\,\mathrm{nm}$ and $\lambda_{\uparrow\downarrow Py} = 0.9\,\mathrm{nm}$ for Permalloy (refer to section 3.1.3). With rising layer thickness the effect ratio increases exponentially.

parallel magnetized. This leads to:

$$BMC = \frac{\left[(0.5+0.5P_E)e^{-d_{Co}/\lambda_{\uparrow\uparrow Co}} \cdot e^{-d_{Py}/\lambda_{\uparrow\uparrow Py}} + (0.5-0.5P_E)e^{-d_{Co}/\lambda_{\uparrow\downarrow Co}} e^{-d_{Py}/\lambda_{\uparrow\downarrow Py}}\right]}{\left[(0.5+0.5P_E)e^{-d_{Co}/\lambda_{\uparrow\uparrow Co}} \cdot e^{-d_{Py}/\lambda_{\uparrow\downarrow Py}} + (0.5-0.5P_E)e^{-d_{Co}/\lambda_{\uparrow\downarrow Co}} \cdot e^{-d_{Py}/\lambda_{\uparrow\uparrow Py}}\right]} - 1. \tag{1.5.2}$$

The influence of the Permalloy emitter is implemented by the spin-polarization terms. This ratio is obviously higher than without spin-polarized injection as a consequence of the additional state. Because of the complexity of this formula, it is visualized in figure 1.16.

Chapter 2

Fabrication and Characterization

2.1 Fabrication

2.1.1 Substrate Choice and Preparation

To observe ballistic effects, the diffusive current fractions have to be filtered from the total current. As mentioned before for this purpose, a Schottky-barrier is used in this thesis. To obtain an appropriate Schottky-contact, the choice of the semiconductor substrate is crucial.

The use of the most common semiconductor in industry and science, Silicon, is not promising because of the difficulty in handling and preparation. The use of semiconductor substrates requires clean room conditions during all the preparation. In industrial Silicon processing standardized clean procedures consisting of several etch and oxidizing steps are used to remove the natural oxide from the wafer and to form a clean atomic smooth surface terminated by Hydrogen. The Hydrogen is removed by subsequently annealing of the sample under UHV-conditions just before the deposition process is started.

This approach is not practicable. If the use of Silicon is not stringent, there are alternatives: Gallium Arsenide is one of the most promising substrates for semiconductor applications and for research purposes. The electronic structure is well known [135]. The charge carrier mobility is higher than in Silicon which makes it a promising candidate for semiconductor applications.

The substrates used in this thesis are Silicon-doped 2"-Gallium Arsenide (100)-wafers with a carrier concentration of $1 - 5 \cdot 10^{17}/cm^3$ [1]. For hybrid junction experiments, a commercial substrate delivered by *Crystec*[2] has been used. The front side surface is epipolished, the backside is lapped. BEEM applications have also been obtained by a substrate grown by Molecular Beam Epitaxy (MBE) by *Strasser et al.* at the TU Vienna, which are crystalline at the surface[3]. With Cobalt deposited on these kind of wafers, it builds up a Schottky-barrier with a height of about 0.5 - 1 eV reverse-biased to the substrate; details are discussed in chapter 3.1.1.

The first step of preparation is the deposition of 50 nm Gold on the backside of the whole wafer by DC-magnetron sputtering and annealing the substrate for 90 s at $370° C$ on a hot plate [137]. Gold atoms move into the substrate via diffusion. This forms an ohmic contact to the semiconductor[4]. After this procedure, the wafer is fragmented to small parts which are used as samples. The next step is the removal of the natural oxide at the surface by an etch dip of the sample in hydrochloric acid for 30 s. This acid etches selectively the surface oxide but not the Gallium Arsenide; this fact additionally benefits smooth surfaces. Immediately after the etch dip the substrate is scavenged in deionized water, dried by a Nitrogen rinse and loaded into the vacuum chamber for deposition.

A better Schottky-barrier could be fabricated by cleaving the substrate in UHV just before sputtering, but this is not possible with wafer surfaces and not necessary for ballistic experiments.

2.1.2 Metal Deposition

All layers are deposited by DC-magnetron or RF sputtering in the commercial full automatized apparatus CLAB 600 from *Leybold Dresden*, see figure 2.1. The layers are sputtered in the main chamber which contains one 4" RF magnetron sputter source for Manganese-Iridium, four DC magnetron sputter sources for Tantalum, Copper, Aluminum (all 4") and Gold (2") and two special DC magnetron sputter sources for ferromagnetic targets[5] (4"). Equipment variations for special purposes, e.g. changing targets or even sources or installing homogenizer for dynamic wobble

---

[1] Error bars for the carrier concentration in Gallium Arsenide wafers are usually in this magnitude.

[2] Crystec Charge number S3620 and S3629. For a detail characterization of electronic properties refer to [136].

[3] The polishing process performed at commercial crystalline substrates damages the perfect surface. In the MBE system perfectly finishing crystalline layers are grown.

[4] In fact the contact is a low quality Schottky-barrier. Its resistance, especially in reverse-bias direction, can be neglected compared to the Cobalt Schottky-barrier.

[5] The permanent magnet under the target is stronger in such sources due to the field shielding of the ferromagnetic target.

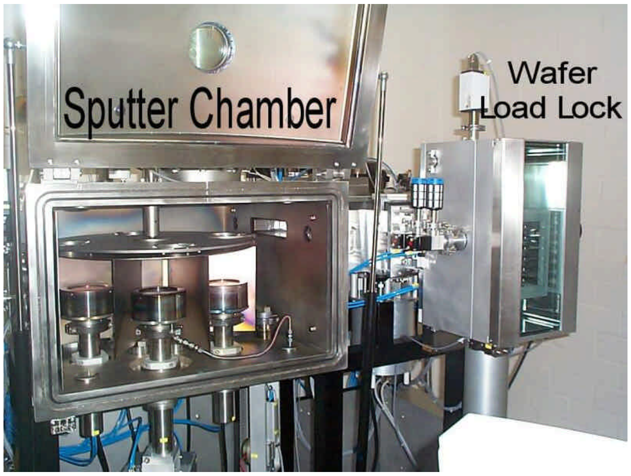

Figure 2.1: CLAB 600 by *Leybold Dresden*.

deposition, are possible within a few hours. The chamber has a base pressure of at least $3.5 \cdot 10^{-7}$ mbar. For sputtering, Argon is let into the chamber to a pressure of about $1.3 \cdot 10^{-3}$ mbar; during the sputtering the pressure is kept constant by shifting a shutter in front of the main turbo pump at a certain level. The sputter power is kept constant at 115 W for all materials except Gold (29 W). The sputter rate of each target is controlled at regular intervals by reference samples which are analyzed by X-ray diffraction or AFM, refer to [57]. Additionally standardized magnetic tunnel junctions are sputtered and evaluated regularly[6]. This well known junction is a strong indicator for almost any problem of the sputter apparatus.

Two plasma oxidation chambers are implemented to the CLAB 600, so that no break of the vacuum is necessary for the oxidizing procedure. The first is a microwave plasma chamber, the second a pulse-plasma chamber (which has not been used for these experiments). Barriers are prepared by first sputtering a layer of 1.4 nm Aluminum and oxidizing that in the next step, yielding a 1.8 nm thick Aluminum oxide layer. An 1.8 nm Aluminum oxide layer evolves from the Aluminum and the Oxygen. To control charge effects on the surface of the sample during the oxidation, a drop of silver paste is put on the edge of the sample, so that a connection to the sample holder is guaranteed. The sample holder is put on a controlled electrical potential of -10 V against the microwave base [139]. This is stringent for predictable results in

---

[6] The properties of this stack are presented in e.g. [20][138]

oxidizing. For a closer look on plasma oxidation processes refer to [138].

The Manganese-Iridium, a natural anti-ferriomagnetic alloy, has to be either annealed over Neèl temperature[7] and cooled down in a homogenous magnetic field, referred to *field cooling*, or sputtered in presence of a magnetic field.

The first process must be accomplished *ex situ*. If the whole stack is annealed, a further advantage, especially in magnetic tunnel junctions, occurs: defects and imperfections in the tunnel barrier can heal.

The second process must be accomplished *in situ*. The most mentionable advantage here is that it is not necessary to anneal the sample, because the heating may change some sample properties. The second advantage lies in the wide open possibilities of magnetic design, especially in sensors, which are not possible by *ex situ* alignment. Ferromagnetic layers can be aligned in different direction within one stack. Furthermore, one preparation step is saved. In presence of a crystalline axis of the substrate it is necessary to attend on a reasonable alignment of this axis and the field direction. The crystal anisotropy might induce a hard axis in direction of the exchange bias field otherwise. Except the Cobalt layer thickness, the stack is always the same in the following experiments:

x nm Co/ 1.8 nm Alox./ 4 nm Py/ 10 nm MnIr/ 4 nm Ta / 50 nm Cu / 30 nm Au

The base-layer thickness x is varied between 4 and 12 nm. Stacks with less than 4 nm base thickness are impossible to characterize. Especially in the uncovered parts of the lower electrode (see chapter 2.1.3), where the Cobalt surface oxidizes, no proper connection via this layer in guaranteed. More than 12 nm thickness leads to the limit of current resolution in the measurement of ballistic electrons; the emitter current should be $\geq 50\,pA$ for clear results in the used measurement setup. In contrast to usual TMR stacks no buffer and conducting layers can be deposited under the lower electrode. 1.8 nm Aluminum oxide forms the tunnel-barrier. The upper electrode consists of a Permalloy layer, antiferromagnetically pinned by Manganese-Iridium. All layers above the tunnel-barrier are sputtered in a magnetic field, applied by two Neodymium-Iron-Boron permanent magnets, integrated in a sputter-mask[8]. This induces an alignment of the Permalloy to the antiferromagnetic Manganese-Iridium. The field is aligned along the (100)-axis of the Gallium Arsenide to avoid angles between the Cobalt and Permalloy easy axis [9]. Tantalum is deposited as a diffusion barrier. Copper and Gold layers are put on top for the electrical contact and to avoid

---

[7] This threshold is no constant but dependent on the layer thickness. The blocking temperature is always about $175^\circ C$.

[8] The sputter mask is not removed during the deposition of the non-ferromagnetic layers because this might induce bugs in the processing of the handlers inside the sputter chamber.

[9] Though the mask change is a critical process, it is applied during the whole sputtering of the upper electrode.

oxidation.

Subsequently the sample is annealed at $200^\circ C$ for 20 minutes and cooled down in a magnetic field. This step is rather important to increase the quality of the barriers than for the magnetic advancement. Up to an annealing temperature of $200^\circ C$ the ideality factor approaches to 1 and the diode in reverse-bias direction blocks the current better after annealing. Crossing this threshold degrades both parameters. The sample gets more and more ohmic, probably due to diffusion and alloying processes of the gold at the sample backside and the Cobalt.

2.1.3 Lithography

The lithographic procedure begins with spin-coating and baking of resist layers on the sample surface. This synthetic layer is exposed and developed, so that parts of the sample are protected by the remaining resist in a subsequent Argon ion beam etch process. Several different resists of *Allresist* have been used in this thesis. The ion milling process is controlled by a Quadropol Mass Spectrometer (QMS), so that the stop in a certain layer is possible. After this the resist is removed.

Three different types of lithography were used in this thesis:

1. Optical Lithography with Masks

This technique is accomplished by putting a prefabricated mask that is light permeable at the areas which shall be exposed on the sample. An ultra violet lamp, operated by the *Thermo Oriel* controller[10] exposes the photosensitive resist (AR-P 535[11], spin-coated 1 s at 200 rpm and 30 s at 6000 rpm, baked 30 min at 95° C) for a certain adjustable time. After developing the resist remains only at the light protected areas. Although smaller patterns are possible, the minimum reasonable size is $\approx 5 \times 5\,\mu m^2$. This is the fastest and easiest pattern procedure but exact positioning of the mask is not possible.

2. Optical Lithography with Laser Lithographer

The exposing procedure is accomplished by a commercial laser exposing apparatus by *Heidelberg Instruments*. The sample is scanned under a lens, equipped with a shutter,

---

[10] Controller: Digital Exposure Control Model 68950.
Lamp: Thermo Oriel Instruments Model 87431-1000-1.
Power supply: 68810 arc lamp power supply

[11] This positive resist is exposed inverse, thus it works like negative resist.

which lets the ultra violet laser light pass to the areas which are to expose. The result after developing is the same like in optical lithography by masks, but the minimum pattern size is $\approx 1\,\mu m^2$. The positioning of the starting point on the sample makes directed exposing possible, assisted by a positioning camera. The same resist is used as for mask lithography.

3. Electron Beam Lithography

A Scanning Electron Microscope (SEM) from *LEO* (LEO 1530) has been upgraded for e-beam lithography by *Raith Instruments.* A current-sensitive resist (AR-N 7500, spin-coated for 1 s at 200 rpm and 30 s at 4000 rpm, baked for 2 min at 85° C) is exposed by the electron beam. The theoretical minimum pattern size is more dependent on the resist than on the SEM. Practically the smallest dots using PMMA resist are $\approx 25 \times 25\,\mathrm{nm}^2$ and the minimum gaps are $\approx 10\,\mathrm{nm}$. The smallest magnetic tunnel junctions fabricated and characterized with conducting AFM was a 50 nm dot [140]. Due to the fact that the used device is originally a SEM extremely exact positioning is possible.

In contrast to usual TMR characterization for ballistic current measurements, it is necessary to pattern the lower TMR electrode, here to $625{\times}625\,\mu m^2$ squares, so that the Schottky-barrier area is defined and not large[12]. The single junctions and a contact to the lower electrode is patterned inside these squares. At least a two step lithography is necessary.

The first step can be accomplished by optical mask lithography. After exposing and developing the Argon ion etch apparatus is used to remove the uncovered material down to the substrate.

The second step can be either accomplished by the laser exposer or e-beam lithography, because of the necessity of positioning. On top of the $625{\times}625\,\mu m^2$ squares now squares of $50 \times 50\,\mu m^2$, $80 \times 80\,\mu m^2$ and $100 \times 100\,\mu m^2$ are exposed. Additionally the border and a part of the middle is endorsed like displayed in figure 2.2. Afterwards the sample is etched until the aluminum oxide barrier can be detected with the QMS. The tunnel barrier at the surrounding area is mechanically destroyed extensively[13] and is used as a contact to the lower ferromagnetic electrode. Due to the large area the resistance to the base electrode is low compared to that of a single junction. The TMR bias can be applied now between the outer structure and the single junctions.

---

[12] In principle it would be adequate to cleave the edges of the sample properly away, so that no shortcuts on the sides influence the Schottky-barrier.

[13] During the ultra sonic bonding this area is contacted at several points. Due to local destructions of the tunnel-barrier and the superior area the net resistance at the tunnel-barrier is negligibly.

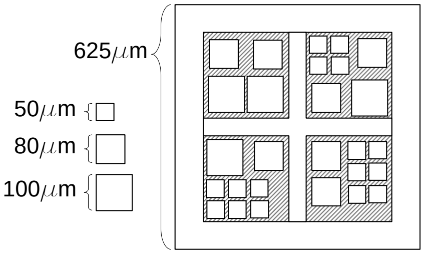

Figure 2.2: Lithographic design schematic. Three different sizes for the MTJs are patterned. The border is used for the contact to the lower electrode. It is kept near to the single junctions to avoid high ohmic resistance within the thin lower electrode, which is not protected against oxidation.

Subsequently the sample is glued in an IC-Socket by conducting silver (to ensure the ohmic contact) and contacted by $25\mu m$ gold wires, connected by ultra sonic bonding.

2.2 Characterization Techniques

2.2.1 Electrical Characterization

TMR ratio

In practice the TMR ratio is measured by applying a small bias of 10 mV or less at the tunnel-barrier and recording the resistance versus a magnetic field. The sample is fixed between coils. A magnetic *major-loop* in a simple MTJ[14] is recorded as follows:

The field is linearly driven from a high field down to zero and up to the negative maximum value, then returned to the positive value. After the zero-crossing, when the coercivity H_{C1} is reached in negative direction, the first layer will switch; the resistance increased. Increasing the field further, H_{C2} will be crossed in negative direction and the resistance will fall back to the original value. The switching on way back to the initial value is analogous unless there are special couplings (Neél-coupling,

---

[14] "Simple" means without pinned layers or similar interlayer or shape induced couplings.

exchange-bias etc. refer to chapter 2.2.2 or [20]). Indirectly, the hysteresis of both layers can be recorded and the TMR ratio is specified.

A *minor-loop* is performed by stopping the field enhancement at the antiparallel state and going back again. The complete hysteresis for the soft magnetic layer can be recorded like this (including zero-crossing magnetization on the way back) and the TMR ratio is measured.

It should be mentioned here that the choice of 10 mV bias is a user defined setting which is only constituted by practical reasons. Thorough measuring at low temperatures should be accomplished with less bias; 10 mV electron energy is nearly similar to room temperature electron energy. On the other hand ballistic currents need higher bias, so that non-scattered electrons can pass the Schottky-barrier.

Tunnel barrier

Additionally to major- and minor-loops it is reasonable to record the I/V characteristics. The evaluation of the tunnel-barrier, described in chapter 1.1.1, reveals its quality. The thickness from the Brinkman fit should be close to the known thickness from the sputter parameters and the barrier height should be sufficiently high, otherwise the TMR ratio is affected. Furthermore, a low quality barrier will not allow ballistic measurements, due to the dielectrical breakdown at low bias voltages.

BMC

Characterizing a hybrid junction requires a two channel measurement, similar to the BEEM setup. The conventionally measured TMR tunnel-current is the first. Additionally the ballistic current between lower electrode and semiconductor is monitored simultaneously.

For this recording a special high internal resistance amplifier/measurement box was designed and build in collaboration with *Slawomir Czerkas* and the *Elektronik Werkstatt, Physik Universität Bielefeld*. Instead of common two probe (four probe[15], respectively) measurement specialized boxes, this device has a third independent electrode. Bias can be applied and currents plotted from electrode one to two (channel one) and electrode two to three (channel two), where the joint electrode two is grounded. For that reason both currents are recorded related to the ground. This is

---

[15] Four probe measurement of the TMR ratio is not advisable in TMR/Schottky hybride junctions. The lower electrode is thin and might be oxidized at uncovered areas. This leads to a high lateral resistance which can induce measurement artifacts in the effect ratio [141].

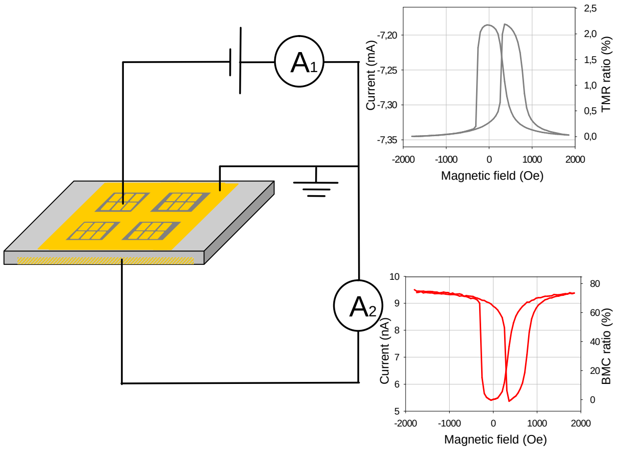

Figure 2.3: Sketch of electrical characterization. Junctions, patterned like shown in figure 2.2 are connected by US-bonded Gold wires. For connecting the upper electrode, the top of the junction is connected; the base is contacted via the border. The TMR-ratio is measured by plotting the currents I_1 (at the ampmeter A_1) and the BMC-ratio by plotting I_2 (at the ampmeter A_2) versus the magnetic field.

useful because measurements on floating potential are more difficult and limited in resolution. Figure 2.3 is a sketch of the setup.

To obtain clear results it is necessary to measure at low temperature. For that purpose a closed cycle helium cryostat by *Oxford Instruments*[16] is used. Temperatures between 10 K and 330 K can be accessed, stabilized, and computer controlled[17]. The sample IC-socket is plugged into the cryostat. The electrical connection to a switching box is established. This box performs the switching of the single pins of the IC-socket computer controlled to the amplifier/measurement box. The amplified signals are analyzed by two *Keithley 2000* multimeters, which are digitally read out by a computer via IEEE. The computer saves all data to the department server.

When the tunnel bias (in the right direction and sufficiently high) is applied on channel one (the grounded electrode two is the lower electrode), ballistic currents are monitored on channel two, without applying a bias. Diffusive scattered electrons can discharge to the ground. Although both channels are able to record in the same

---

[16] Cryopump: Edwards Crypdrive 1.5

[17] Controller: Oxford Instruments ITC 503

range of currents and the hardware is identic, the second channel is optimized for small while the first is more accurate for higher currents[18].

MR-Characterization via I/V-Curves

An alternative approach to characterize a BMC-junction completely is to record two I/V-characteristics, one in parallel and one in antiparallel alignment of the magnetic electrodes. The bias is applied at the tunnel-barrier and the current at the Schottky-barrier is measured again simultaneously. Tunnel barrier parameters can be obtained with the Brinkman fit from the graph with parallel electrode alignment. Plotting the effect ratios TMR=(I_{TBP}(V)/I_{TBAP}(V))-1 and BMC=(I_{SBP}(V)/I_{SBAP}(V))-1 versus V yields the complete bias dependent TMR and BMC characteristics.

In practice, there is a non-trivial obstacle using this technique: The noise on both measurements affects the resulting plot drastically. Especially at the Schottky-barrier, the signal can range from the magnitude of pA in reverse- to μA in forward-bias direction. Noise reduction is difficult because the amplification of the signal cannot be adjusted to these conditions during the measurement due to different internal resistances on the amplifier/measurement box.

Although this characterization method has been used for TMR/Schottky hybrid junctions in this thesis this technique is more important for BEEM spectra of spinvalves (refer to section 4.4).

2.2.2 Magnetic Characterization

The magnetic analysis is primarily used for the spinvalve experiments in chapter 4 and 3.2, because the existence of an antiparallel alignment of ferromagnetic layers is crucial there. Also in TMR- and GMR-junctions, an antiparallel alignment is desired. For that reason magnetic investigations are performed in this thesis. Interactions between the layers may influence the magnetic behavior and consequently the magnetoresistive effects. In most real stacks additional pinning layers (e.g. antiferromagnetic layers [142] [143]) are included for better antiparallel arrangement. Other natural exchange couplings between the layers are present additionally. Néel coupling [144], dipole coupling[19] and anisotropic behavior of the magnetic layers influence the switching process. Computer aided simulations of switching processes are an established tool to predict and to interpret the behavior experimentally found.

Most computer simulations of spintronic junctions are based on the *Stoner Wohlfarth* model [145]. In principle, these calculations are obtained by finding the local

---

[18] Due to offset calibrations it is impossible to be accurate over the whole range.

[19] Due to the lateral large MR-junctions dipole couplings are negligible here.

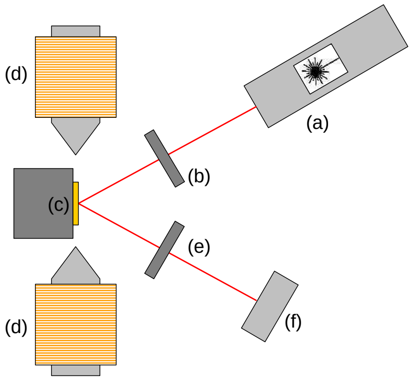

Figure 2.4: Sketch of MOKE setup. A laser (a) transmits light through a linear polarizer (b) to the sample on a fixation (c). Two ferrite coils (d) apply the magnetic field for the minor-loop. The reflected light has two pass the analyzer (e) which is a linear polarizer, 89° rotated to the first polarizer. The intensity of the laser beam behind this analyzer is recorded by a photodiode detector (f).

minimum of energy terms (Zeeman-, anisotropy- and orange-peel-term). Other simulations include the local magnetization and can map it in a graphical output, e.g. *oommf* (Object Oriented MicroMagnetic Framework) by the *National Institute for Standards and Technologies* [146].

This thesis concentrates on experimentally characterization of the magnetic behavior. Simulations cannot deliver additionally important information.

MOKE

The magnetic behavior of a MR-junction with a total stack thickness ¡20 nm can be investigated by performing a Magneto Optical Kerr Effect (MOKE)[20] measurement [151].

The experimental setup is arranged as follows: The light of a low-noise 0.5 mW laser diode is polarized and pointed on the sample in an angle of 25° to the sample

---

[20] As the name implies MOKE is based on the Kerr effect [147] [148]. This phenomenon is based upon the spin-orbit coupling and implicates the circular polarization of reflected light to the magnetization of the reflector surface [149] [150].

plain. The sample is fixed between Ferrite rod coils, which can apply a magnetic field of up to 3500 Oe. The reflected ray has to pass a second polarization filter, which is rotated 89° to the first and points into a photodiode detector. The setup is shown schematic in figure 2.4. For a detailed review on magneto optical Kerr effect characterizations refer to [151].

Chapter 3

Injection of Ballistic Currents via Tunnel/Schottky-Barrier Hybrid Junctions

3.1 Results from TMR/Schottky Hybrid Junctions

As mentioned in chapter 1.3.2, it is necessary to plot the collector-current versus the base-layer thicknesses t to obtain attenuation lengths by a regression. For that purpose the base electrode of the TMR stack must be varied to a reasonable extent for the analysis presented in this chapter. The remaining layers are kept in constant thicknesses for reproducibility purposes.

3.1.1 General Characterization of the TMR/Schottky Hybrid Junction

TEM

A powerful tool to examine a stack of thin films directly is the Transmission Electron Microscope (TEM) [152] [153]. Figure 3.1 shows a TEM cross section picture of a typical hybrid junction. The Aluminum oxide layer is the only amorphous layer; all others show crystalline growth. The crystalline growth of the Cobalt base layer is crucial for ballistic experiments. A consequence of small crystallites is the existence of many grain boundaries; these cause scatter processes which reduce the ballistic transmission. During the BEEM experiments in Vienna, a spinvalve with Ruthenium spacer and cover could not be characterized due to the low transmission. Ruthenium layers are known to have small crystallites and are a common spacer in GMR junctions [46][154]. This spinvalve has been 4 nm thinner than other spinvalves with Copper spacer and Gold coverage, which could be characterized. Amorphous growth would lead to even smaller signals. In fact, the Cobalt layer in figure 3.1 is crystalline.

The contrast between the Cobalt and the Gallium Arsenide is a strong indication for an oxide layer on the III-V semiconductor. This originates from the fact that the wafer is temporarily exposed to air between the etching process and the metal deposition. The interlayer has a thickness of approximately 1 nm and affects the barrier characteristics; quantifications will be presented later in this chapter. The consequences to the ballistic transmission have been neglected in this thesis. This neglect is legitimate because this thin barrier has no strong influence, as the characterizing parameters show, see below. The total electron transmission into the substrate might be reduced, but surely this is no spin dependent effect, so that the results are not affected. Furthermore this oxide protects Cobalt and Gallium Arsenide against intermixing by diffusion. This would decrease the Schottky-barrier quality[1] and cause inaccuracies in the quantification of the attenuation length due to the unknown metallurgy of the boundary area.

It is unlikely that the contrast is a consequence of the growth of the layer. When a Cobalt layer is deposited, the growth starts with a fcc arrangement. With increasing thickness, the alignment changes to hcp, which is favorable in thermodynamic equilibrium [155]. It is not known if this occurs only when the metal is deposited on amorphous substrates like Silicon oxide or on crystallite, too. Due to the fact that the density of fcc and hcp Cobalt is the same, it is not visible as a contrast in a TEM picture.

---

[1] Intermixing leads to an ohmic contact.

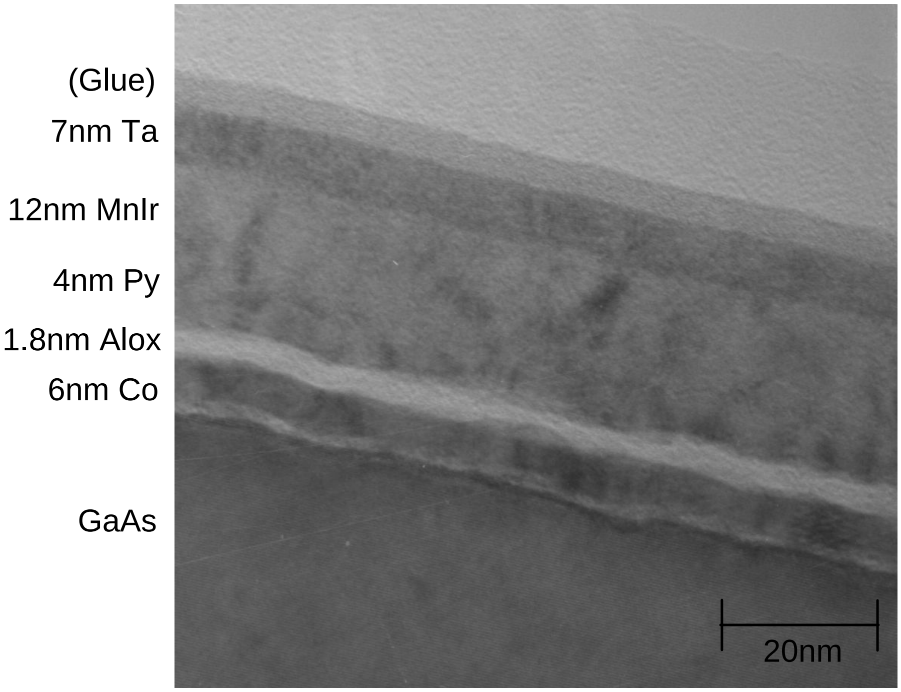

Figure 3.1: TEM cross section picture of a TMR/Schottky hybrid stack. Crystalline growth of all layers except the amorphous Aluminum oxide can be anticipated. The contrast inside the Cobalt layer, near the interface to the substrate, seems to be due to an oxide layer on the Gallium Arsenide. The boundary between Permalloy and Manganese Iridium layer is hard to see.

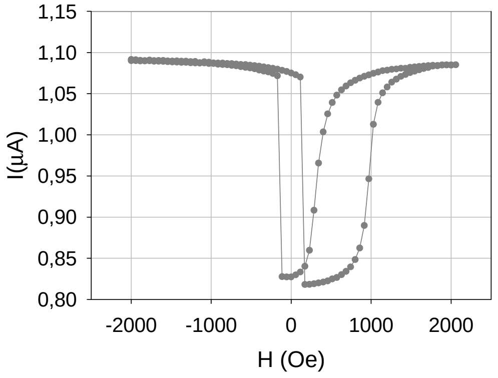

Figure 3.2: TMR major-loop of a BMC junction, recorded at 10 K and 10 mV bias. The junction has a lateral size of $50 \times 50\,\mu m^2$. The area resistance is $\approx$25M$\Omega\mu m^2$. In positive magnetic field direction, the sample is not saturated entirely. For technical reasons fields higher than 2 kOe are impossible to apply inside the cryostat. In this case an effect amplitude of more than 32% is observed, although the antiferromagnetic coupling is not perfect.

By using a TEM cross section picture, the total thickness is controlled. In this particular case, the Cobalt layer of nominal 6 nm thickness is about 5.7 nm thick in the TEM picture. This difference is within the error bar of 8% from the XRD-technique which is used to calibrate the sputter rate.

Tunnel Barrier and TMR

The TMR ratio varies from 12% to 14% at room temperature and from 24% to 32% at 10 K. The variation is due to the imperfections in the stack and the barrier, which cannot be optimized for every base layer thickness. Figure 3.2 shows a typical major-loop. The plateau in the current's minimum is a strong indicator for an antiparallel alignment of the magnetic electrodes. The *in situ* alignment of the Manganese Iridium layer is not as perfect as annealing above Néel temperature and cooling down in a magnetic field.

The tunnel-barrier is characterized using Brinkman's fit as explained in chapter 1.1.1. Samples without reasonable values for barrier height, thickness and asymmetry are not taken into account for two reasons:

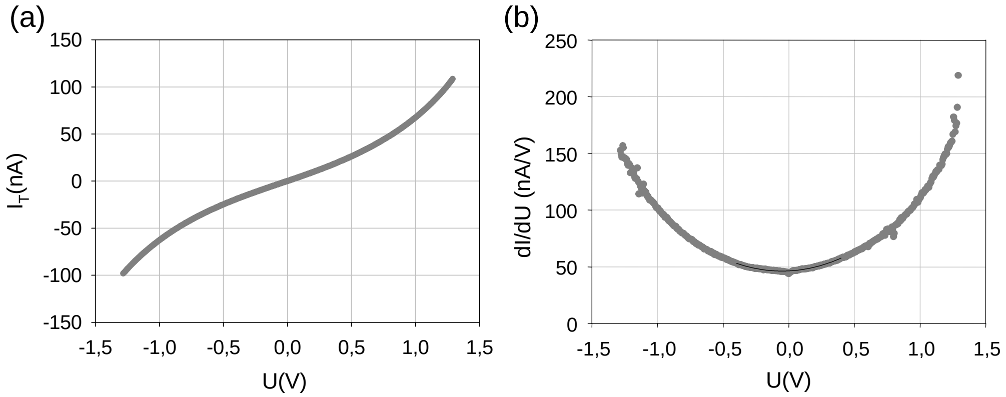

Figure 3.3: (a) Exemplary I/V plot of a $100{\times}100\mu m^2$ tunnel-barrier of MTJ. (b) Differentiated I/V plot. The Brinkman fit is used for evaluation. Therefore the data in the range of -400 to +400 mV are fitted with a paraboloid, sketched as a black line. This leads to a barrier height of Φ=3.2 eV, a thickness of d=1.75 nm and an asymmetry of $\Delta\Phi = 1.2\,eV$.

- Results would be dubious.
- Applying the necessary bias of at least $\sim 1\,V$, the junction is destroyed.

Figure 3.3 shows a typical I/V plot (a), its derivative (b) and an exemplary evaluation. These results are reproducible. The barrier height of 3.2 eV is a reasonable value, compared to other stacks with 1.8 nm Aluminum oxide. Typical values are $\Phi = 2.7 - 3.2$ eV. The barrier thickness is close to the expected value of d=1.8 nm. The asymmetry $\Delta\Phi = 1.2\,eV$ cannot be evaluated here. In standard TMR stacks with Cobalt and Permalloy electrode, embedded in seed and conducting layers, an asymmetry of $1 - 1.8$ eV is measured, too. This parameter is strongly dependent on offsets during the measurement. For I/V plots the measurement amplifier box has to be switched to a large effective range. The box offset is optimized for low ranges to characterize small currents. For technical reasons, it is impossible to optimize the measurement box in all working ranges at the same time. Offsets during I/V measurements might affect the measured asymmetry. Due to the fact that the more significant values Φ and d are in the expected range, it is possible to summarize that the Aluminum oxide layers are high quality tunnel-barriers.

Schottky-Barrier

In practice three conditions lead to high quality Schottky-diodes:

- Noble metal contacts (e.g. Gold)
- Perfect substrate surfaces (e.g. crystals cleaved under vacuum conditions)
- Undoped semiconductor with low carrier concentration

None of the conditions above is fulfilled in this case. First of all Cobalt is no noble metal. Furthermore, an oxide layer between Cobalt and Gallium Arsenide may influence the interface properties, as the TEM cross section picture 3.1 may indicate. The difficult theoretical description of Schottky-contacts with transition metals has already been sketched in chapter 1.2.3. Moreover, the substrate used for the experiment is doped.

For that reason, the Schottky-barrier of Cobalt to Gallium Arsenide is of comparably low quality. The ideality factor is typically between 1.3 and 1.5. As explained in chapter 1.2.4 this imperfection is due to combined effects of image force and applied field, tunneling contributions, recombination effects and trapping at interface states.

As an example figure 3.4(a) shows a typical Schottky I/V-characteristic. An ideality factor of n$\approx$ 1.4 can be evaluated from the logarithmic plot 3.4(b). The saturation current density can be read as $0.2\,\mathrm{pA}\mu m^2$. Calculating the Schottky-barrier height with equation 1.2.10 results in $\Phi_{SB} \approx 0.8\,eV$. The plausibility of this value is limited due to the non-ideal barrier, but the magnitude is reasonable. These results for ideality and barrier height are reproducible for almost all samples. In the literature $\Phi_{SB} = 1\,eV$ with n=1.06 and $\Phi_{SB} = 0.86\,eV$ with n$\approx$1 are reported for Cobalt on n-type (100) Gallium Arsenide [156][157]. In these experiments the substrate has been an undoped crystal with a carrier concentration of $2\times10^{16}/\ \mathrm{cm}^3$, and Selenium doped with a carrier concentration of $6\times10^{16}/\mathrm{cm}^3$, respectively. Therefore, the measured parameters in this experiment are reasonable values.

Experiments with Gold instead of Cobalt do not show high quality parameters, either. The best ideality factor of a Gold/Cobalt contact was 1.3 with $\Phi_{SB} = 0.5\,eV$. The reason for the non-ideal contact does not seem to be Cobalt specific but preparation technique specific. The oxidation of the substrate surface before the metal deposition cannot be prevented.

Fortunately, in practice a high quality barrier is not necessary for ballistic experiments. The barrier is only the filter which separates ballistic electrons from diffusively scattered electrons. High energy electrons have a better chance to pass the barrier as to be seen in figure 3.4(a).

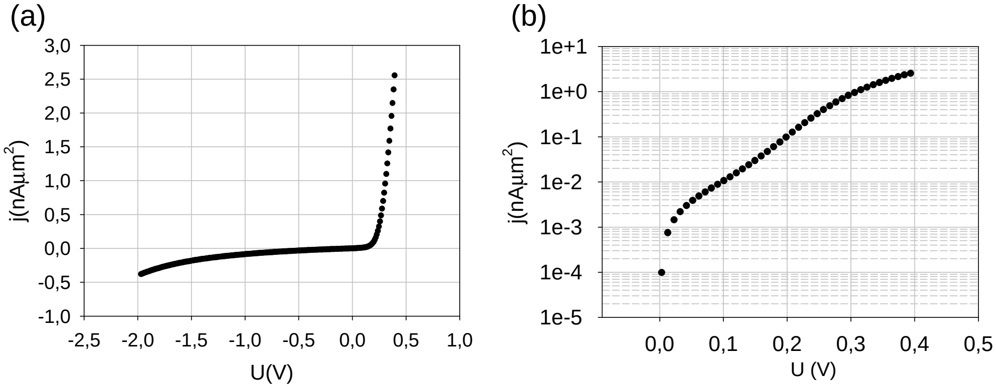

Figure 3.4: (a) I/V characteristic of Schottky-barrier at room temperature. (b) Same characteristic with logarithmically scaled current density (certainly only in forward direction). The ideality factor is n$\approx$ 1.4. With $j_s = 0.4\,pA/\mu m^2$ the Schottky-barrier height can be derived as $\Phi_{SB} \approx 0.8\,eV$. The accurate determination of j_s is affected by the ideality factor, q.v. figure 1.11. For that reason the plausibility of the Φ_{SB} value is limited.

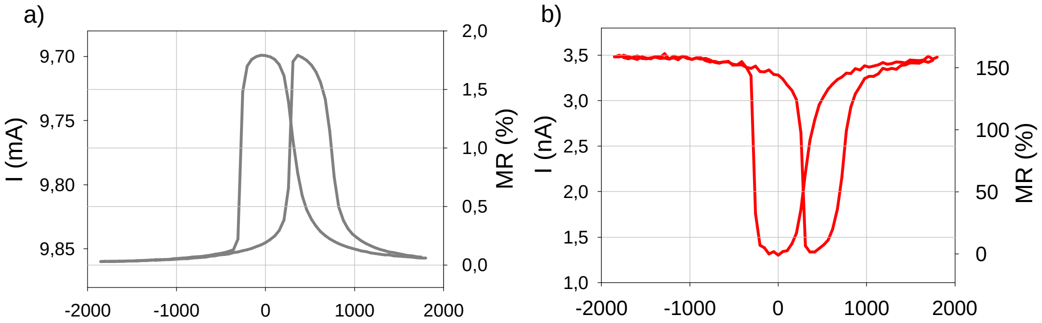

Figure 3.5: Major-loops of a TMR/Schottky hybrid junction (base thickness 4 nm), recorded at 10 K temperature and 1.6 V bias. The TMR channel (a) shows reduced TMR characteristic. The reduction of the ratio is due to the high bias. The simultaneous measured ballistic current (b) has a higher effect ratio but a lower current amplitude.

3.1.2 BMC

Figure 3.5 shows an exemplary major-loop of a TMR/Schottky hybrid junction. In the next sections the coherence of ballistical parameters with the base thickness, bias, temperature and spin attenuation lengths are analyzed.

BMC Ratio vs. Base Thickness

Figure 3.6 shows the measured BMC-ratios versus the base thickness. Such measurements are strongly influenced by inaccuracies, especially by small offsets at the Schottky-barrier which cannot be prevented. Consequently, the values vary. The black plot is an approximation for the maximum BMC ratio with $\lambda_{\uparrow\uparrow}$=6,0 nm, $\lambda_{\uparrow\downarrow}$=1,0 nm and 40% spin-polarization from the emitter. The dashed grey plots are approximations of the error induced by the sputter calibration error. It is plausible that (almost) all measured values are below the theoretical prediction, which requires ideal conditions. On the other hand, the measured ratios are not far below this threshold, which is an indicator for the good quality of the junctions.

To interpret and evaluate figure 3.6 it is necessary to investigate the influence of small offsets to this particular measurement.

Using equation 1.3.6 and 1.3.7 it is possible to estimate the idealized theoretically

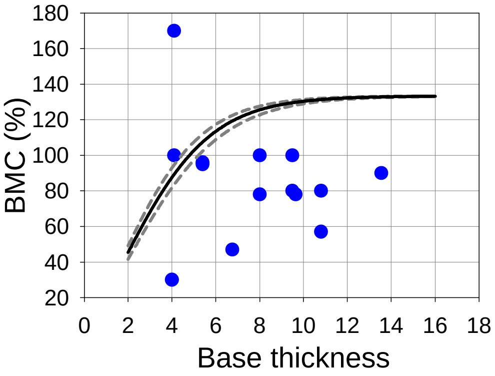

Figure 3.6: BMC-ratio versus base thickness. The BMC values scatter in the region of 80-100%. The black plot is the calculated maximum BMC for $\lambda_{\uparrow\uparrow} = 6,0\,nm$, $\lambda_{\uparrow\downarrow} = 1,0\,nm$ and 40% spin-polarization from the emitter. The dashed grey plots are 8% error bar approximations from the sputter calibration. The extraordinary value of 170% is unrealistic and seems to be an artifact.

predicted BMC ratio versus the base layer thickness for predetermined attenuation lengths and emitter spin-polarization. This has been accomplished exemplarily in figure 3.7.

As this figure suggests, the BMC ratio increases with rising base thickness. The increase ends at a certain threshold base thickness, depending on $\lambda_{\uparrow\downarrow}$, and the ratio converges to a constant value.

The BMC ratio increases, because the electrons polarized antiparallel to the base magnetization get filtered more effectively than the others, when the base thickness is increased, refer to figure 3.8. In this example, the spin-polarization of the ballistic current is more than 90% at 6 nm Cobalt thickness for all assumed $\lambda_{\uparrow\downarrow}$ values and converges to 100% for higher base thicknesses.

When a constant offset bias at the Schottky-barrier affects the ballistic currents $I_{\uparrow\uparrow}$ and $I_{\uparrow\downarrow}$ the behavior changes. Figure 3.9 visualizes the consequences of such an artifact or leak current:

- Offsets falsify the result for a thin base less than for a thick base. Both currents are affected to the same extent by the offset.
- If no offset affects the measurement the BMC ratio keeps almost constant when

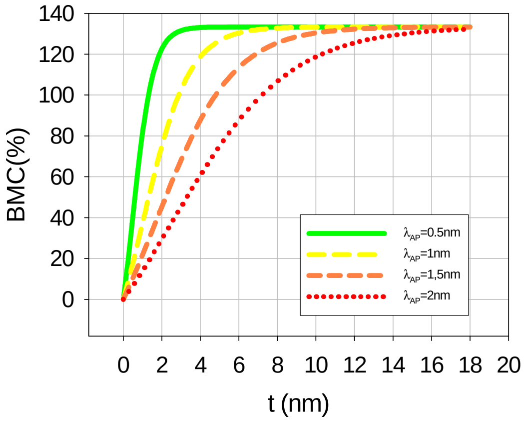

Figure 3.7: Visualization of BMC ratio versus the base layer thickness for different $\lambda_{\uparrow\downarrow}$ values and $\lambda_{\uparrow\uparrow}$=6 nm (the origin of these values is presented later in this chapter). In every case the maximum value converges to ≈130%.

the base thickness passes a certain threshold. The exponential decay of $I_{\uparrow\uparrow}$ and $I_{\uparrow\downarrow}$ forces it to converge.

- For a positive offset, the BMC ratio has a maximum limit and decreases in case of high base thickness. The relative difference between $I_{\uparrow\downarrow}$ and $I_{\uparrow\uparrow}$ is reduced.

- For a negative offset, the BMC ratio diverges for high base thickness. The relative difference of the currents increases.

To avoid this as much as possible, the amplifier/measurement box is gauged at regular intervals. Accurate attendance is crucial for reproducible results. Remaining inaccuracies in the current are in the magnitude of the noise, which is about $\approx 100\,pA$ at room temperature and $\approx 10-20\,pA$ at 10 K. Even such small offset biases can affect the result distinctly. This is the reason for the scattered values in figure 3.6.

It can be summarized that measured BMC ratios should be constant when a certain threshold for the base thickness is crossed, depending on the intrinsic attenuation lengths.

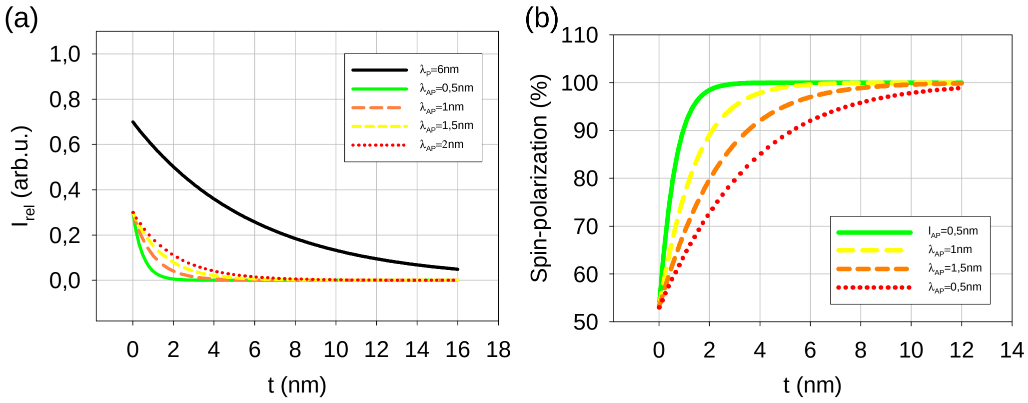

Figure 3.8: (a) Exponential decay of single spin channel currents plotted versus the base layer thickness t in a TMR/Schottky hybrid junction, here in the case of parallel magnetized electrodes. The black line is the parallel polarized current. The other lines are the antiparallel polarized currents for different $\lambda_{\uparrow\downarrow}$ values. Graph (b) is the spin-polarization versus the base thickness, plotted for different $\lambda_{\uparrow\downarrow}$ values. It rises continuously with increasing Cobalt layer thickness in the base.

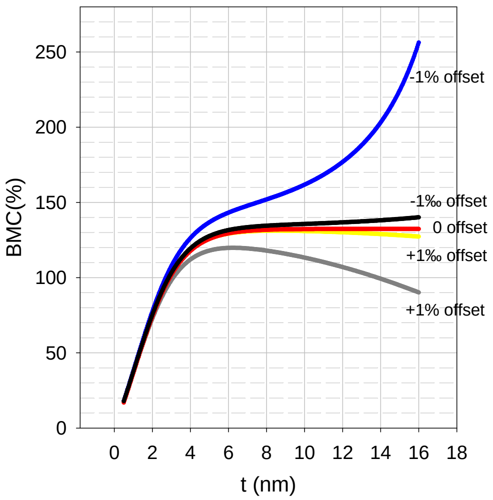

Figure 3.9: Same estimation as shown in figure 3.7 with an offset bias applied at the Schottky-barrier. The original current is increased ±0.1% and ±1%. The Schottky-barrier transmission coefficient T is implemented in the calculations. The red graph again is the graph without offset from figure 3.7. In case of positive offsets, the BMC ratio has a maximum. In case of negative offsets, e.g. when a small potential is applied against the ballistic current, the ratio even diverges, because the total current in antiparallel magnetization alignment converges to zero to a larger extend than in parallel alignment.

BMC Ratio vs. Bias

Depending on the temperature, the injection of ballistic electrons into the substrate can only be detected at comparably high voltages; the standard 10 mV TMR measurement is not possible. It is impossible to constitute a threshold value because the visibility of the effect is limited by the resolution of the current measurement in the used ampmeter. In practice at room temperature, the BMC is seen at voltages above $\gtrsim 500\,mV$ while at 10 K at least $950\,mV$ have to be applied. Figure 3.10 shows the BMC and the TMR ratio versus the bias for different temperatures for a TMR/Schottky hybrid junction with 9.6 nm base thickness. As expected, the TMR ratio decreases for high bias. The maximum BMC ratio is at low temperatures, but it does not disappear completely at room temperature.

Figure 3.10(a) shows the experimentally obtained BMC ratio of a hybrid junction versus the bias at 10 K. The abrupt appearance of a ballistic current is to be seen at the collector electrode at a certain bias value. When the temperature is increased, this threshold becomes blur, refer to figure 3.10 (b), (c) and (d). This threshold does not really exist. The BMC-effect appears above a certain bias because it is not possible to measure the BMC ratio at low temperatures and low bias due to the small current. Especially in antiparallel magnetic alignment, the signal-to-noise ratio is poor. Consequently a possibly existing bias dependence is not observed in this measurement.

In contrast to the plots in figure 3.10, figure 3.11 demonstrates the bias dependence of the BMC ratio. The ratio is calculated from two I/V-plots, one recorded at parallel and one recorded at antiparallel alignment of the ferromagnetic electrodes. Due to the fact that the effect ratio is lower than in figure 3.10(b) (which should be equivalent due to the same conditions during the measurements), it is obvious that the antiparallel alignment during the recording of the plot was not perfect. For that reason the current in antiparallel alignment was to a small extent higher than usual and the signal-to-noise ratio high. In section 4.4 the assumption of a bias dependent BMC-ratio is supported (see below figure 4.5). Due to the fact that the BMC ratio is predominantly dependent on the electron attenuation lengths, this must be the origin of this effect.

From the free electron gas model energy dependent attenuation lengths were to be expected. The dominating electron-electron scattering for the parallel polarized electrons should decrease like:

$$\lambda_{\uparrow\uparrow el-el} \sim \frac{\sqrt{E_e + E_F}}{E_e^2}, \tag{3.1.1}$$

In this equation, E_e is the electron energy. The BMC ratio does not need to be

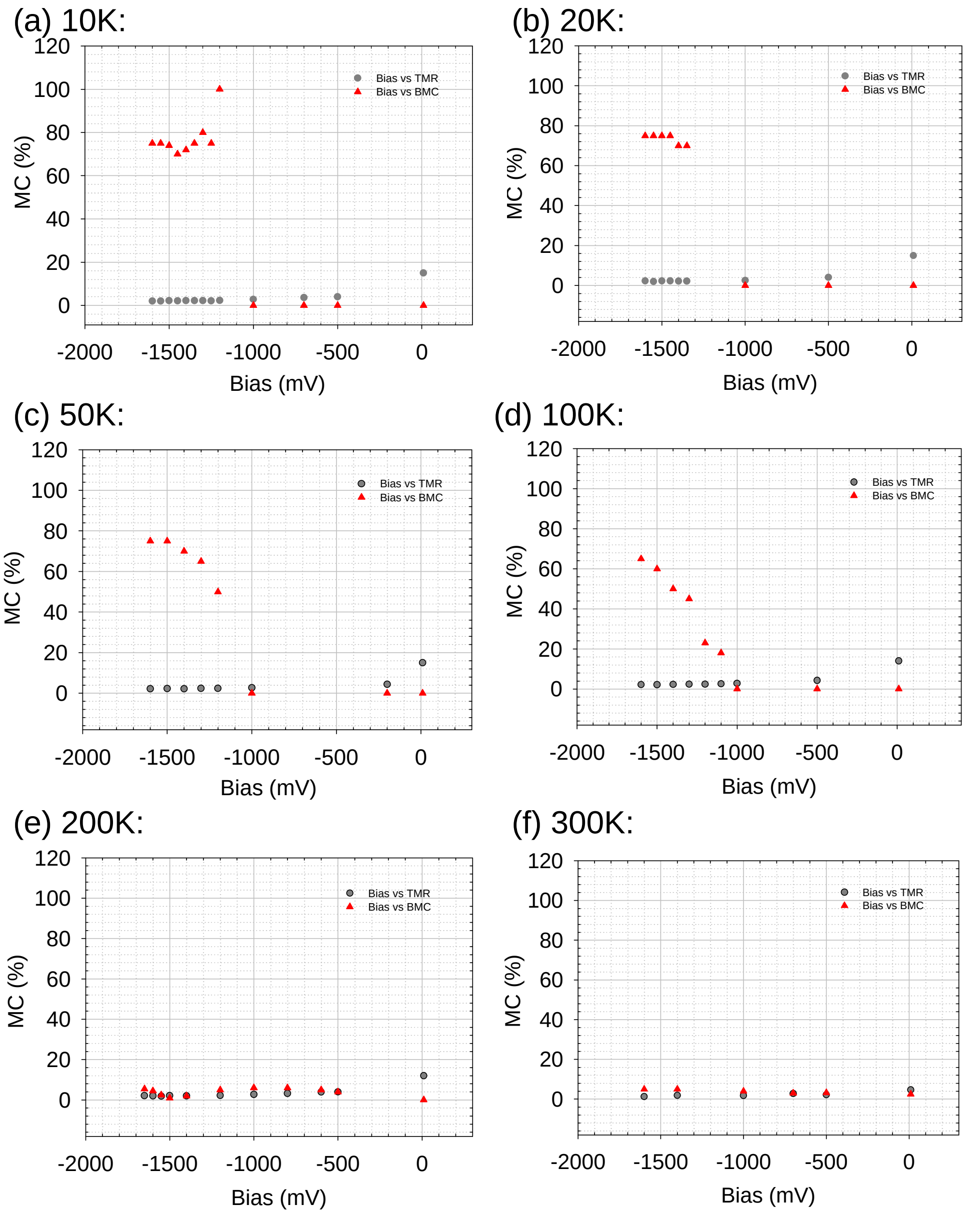

Figure 3.10: BMC and TMR ratio vs. bias for different temperatures. Ballistic transport is detected from 10 K to room temperature. The stack of the junction has a base thickness of 9.6 nm. The lateral size has been 6400 μm^2. The measurement has been started at 10 K. During the last measurement at room temperature the junction has been destroyed.

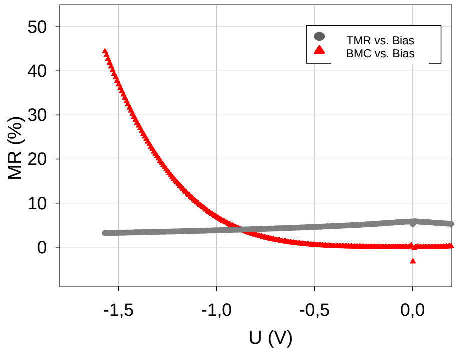

Figure 3.11: Effect ratios versus bias obtained from I/V-plots of the same junction as to be found in figure 3.10 at 20 K (refer to section 2.2.1). In this case a bias dependency of the BMC-ratio can be anticipated.

dependent on this, especially when both spin channels are influenced equally. A closer look at this fact will be taken in the next section.

Above 100 K the signal becomes noisy and small. The BMC ratio exceeds the TMR ratio only slightly and only at high bias, shown in figure 3.10 (e) and (f). The increase of the collector current cannot only be explained by thermal energy variations of electrons. This energy would be ≈25 meV, which is too low. The fact that the ratio emitter current to collector current I_E/I_C increases with rising temperature indicates that the Schottky-barrier properties change. The only temperature dependent effect which influences the barrier ideality factor are tunnel contributions, see equation 1.2.11.

Ballistic currents can be detected up to 330 K, even though the signal is noisy then and no systematical measurement series but only single measurements have been taken.

3.1.3 Spin Attenuation Lengths in Cobalt

The measurement of spin dependent attenuation lengths in transition metals can be taken by gathering the ratio of the collector current I_C to the emitter current I_E for different base thicknesses and fitting equation 1.3.6. The following approximations are necessary:

- Possible influence of the oxide layer at the Cobalt/Gallium Arsenide interface is neglected (see section 3.1.1)
- Possible inaccuracies induced by Cobalt growth are neglected (refer to section 3.1.1)
- The magnetic electrodes are assumed to be perfectly aligned.

The first estimation is legitimate because there is no spin dependent effect at this oxide layer which could falsify the results. Only the total current is decreased.

The second approximation is acceptable because the TEM cross section picture proves the correct calibration of the sputter rate, at least for this particular sample, which has a comparatively thin layer.

The third item is also reasonable, because all measured major-loops showed a plateau in an antiparallel state. This is a strong indication for a good alignment.

The approach of fitting equation 1.3.6 is only justifiable if enough data, especially for very thin layers, are available. Otherwise, the fraction of the antiparallel polarized current can almost be neglected. In this thesis, the attenuation lengths are calculated from the data measured in parallel alignment of the TMR junction's electrodes. In antiparallel configuration, the noise is too large to obtain supplementing information.

Plotting the ratio of collector current to emitter current I_C/I_E versus the base layer thickness shows an exponential decay. Plotting the I_C/I_E-axis logarithmically shows a linear dependence, see figure 3.12(a). If the influence of minority electrons is neglected, which is reasonably above a certain threshold for the base layer thickness, the slope of this linear plot can be evaluated. Assuming $\lambda_{\uparrow\downarrow} = 10\,\text{Å}$ as an approximation, it can be calculated that only $\approx 4\%$ of the electrons at a base layer thickness of 4 nm would be minority electrons. At 5 nm it is only 1.8% of the current. Thus neglecting this fraction is an adequate approach. The result of the linear regression of base thicknesses ≥ 6 nm in figure 3.12 is $\lambda_{\uparrow\uparrow} = 60 \pm 9\,\text{Å}$ [2].

It is also possible to make an approximation of $\lambda_{\uparrow\downarrow}$:

The transmission coefficient at an imaginary base thickness of 0 nm, extrapolated from the linear graph, is $T_{\uparrow\uparrow} = 5 \cdot 10^{-5}$. Due to the fact that the influence of the antiparallel polarized electrons is neglected by this plot, the real total transmission factor is higher. This transmission $T_{\uparrow\uparrow}$ is in the strict sense $T_{\uparrow\uparrow} \cdot (0.5 + 0.5\cdot \text{P}_E)$ [3]. Assuming the spin-polarization of Permalloy to be 53%[4] it is possible to estimate as follows:

---

[2] The fit has been accomplished with the *regression wizard* of *Sigma Plot 2001 v. 7.101*

[3] In the following it is assumed that $T_{\uparrow\uparrow} = T_{\uparrow\downarrow}$.

[4] The experimental value of 53% at 10 K can be found in the literature [20].

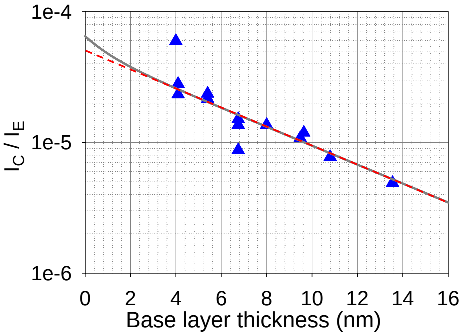

Figure 3.12: Plot of the current ratio I_C/I_E versus the base layer thickness. The currents are measured in parallel configuration of the ferromagnetic electrodes. All data have been measured at 10 K and 1.2 V bias. From the slope of the red dashed line $\lambda_{\uparrow\uparrow}$ can be quantified (the influence of minority charge carriers is neglected): $\lambda_{\uparrow\uparrow} = 60 \pm 9\,\text{Å}$. Also neglected for the regression are the values below 6 nm base thickness. The grey graph is a plot of equation 1.3.6 using $\lambda_{\uparrow\uparrow} = 60\,\text{Å}$ and $\lambda_{\uparrow\downarrow} = 10\,\text{Å}$.

$$T_{total} = T_{\uparrow\uparrow} \cdot (0.5 + 0.5 \cdot P_E) + T_{\uparrow\downarrow} \cdot (0.5 - 0.5 \cdot P_E) = 5 \cdot 10^{-5} + 1.5 \cdot 10^{-5} = 6.5 \cdot 10^{-5}$$

[5]

For that reason it is maintainable to implement a point to the regression with the coordinates t=0 nm and $I_C/I_E = 6.5 \cdot 10^{-5}$. This additional data point allows an approximation of the maximum $\lambda_{\uparrow\downarrow}$.

Plotting a regression curve using equation 1.3.6 shows that reasonable fits are only possible with $\lambda_{\uparrow\downarrow} \leq 20\,\text{Å}$. With higher values the graph does not comply with the data. The grey graph in figure 3.12(a) is an exemplary plot of this equation using $\lambda_{\uparrow\downarrow} = 10\,\text{Å}$ and $\lambda_{\uparrow\uparrow} = 60\,\text{Å}$. The graph visualizes again the difficulty to quantify $\lambda_{\uparrow\downarrow}$ from raw data.

The attenuation lengths in Cobalt have been experimentally determined before in GMR experiments: $\lambda_{\uparrow\uparrow} = 55 \pm 4\,\text{Å}$ and $\lambda_{\uparrow\downarrow} \leq 6\,\text{Å}$ at room temperature [158].

With regard to BEEM-experiments, this result is not approved. Using this technique, $\lambda_{\uparrow\uparrow} = 21 \pm 1\,\text{Å}$ and $\lambda_{\uparrow\downarrow} = 8.3 \pm 0.8\,\text{Å}$ have been measured, again at room temperature [108].

---

[5] These values are in good agreement with comparable experiments, e.g. [10]

	$\lambda_{\uparrow\uparrow}$(Å)	$\lambda_{\uparrow\downarrow}$(Å)	Bias(V)	Temperature(K)	Source
Co	60±9	≤ 20	1.2	10	this thesis
Co	21.0±1	8.3±0.8	1.3	RT	[108]
Co	55±4	≤ 6		RT	[158]
CoFe	67.0±2.6	13±1	1.4	77	[10]
Fe	15±2	21±5		RT	[158]
NiFe (81/19)	50.4±3	9±2	1.4	77	[10]
NiFe (80/20)	43.0±3	10±2	0.9	100	[112]
NiFe (80/20)	46.0±3	≤ 6		RT	[158]

Table 3.1: Review on experimentally found attenuation lengths in ferromagnetic materials. The data is measured with different setups, therefore a comparison might not make sense. This might be a reason for the inconsistent values, especially for Cobalt. The desired magnitudes should not be dependent on the measurement setup but on the material, temperature and bias. Systematical mistakes or inapplicable experiments might falsify these results. Note that the value of $\lambda_{\uparrow\downarrow}$ is in some experiments only approximated, e.g. in this thesis.

These experiments are substantially different. At first, during the BEEM-experiment, the bias voltage was $\geq 1.3\,V$ while GMR-experiments are usually carried out at 10-100 mV. Secondly, the approach and evaluation is completely different.

The BEEM approach is very direct: The attenuation of the current is measured versus the layer thickness. The deviant to values of other groups might be due to the roughness of the layers, which can be seen in the BEEM images.

The GMR-experiment uses a pinned spinvalve characterized in CPP-geometry: Current is injected from an exchange-bias coupled Nickel Iron layer through a spacer into a ferromagnetic (again Nickel Iron) filter layer and subsequently into the so-called "back layer" of which the properties are to be examined [158]. A similar setup has been used before to perform spin-accumulation experiments on Gold [159].

Both experiments show in common: The minority electron attenuation length is below 10 Å. In case of TMR/Schottky hybrid junctions, extremely thin base layers are necessary for an adequate quantification; base layers thinner than 40 Å are impossible to prepare with the setup used in this thesis, refer to section 2.1.2. Nevertheless the majority electron attenuation length is easy to measure in ballistic experiments.

Table 3.1 shows a review on several experimental attenuation lengths in transition metals. Only comparatively few data can be found in literature, especially at low temperatures. For that reason, the results of this thesis are difficult to compare with those from other experiments; the injection energy and the temperature are different. Nevertheless, a qualitative comparison is possible:

- Most investigated ferromagnetic materials have $\lambda_{\uparrow\uparrow} \approx 40 - 60\,\text{Å}$
- Usually $\lambda_{\uparrow\downarrow} \approx 5 - 15\,\text{Å}$, therefore it is considerably smaller than $\lambda_{\uparrow\uparrow}$.
- The injection energy does not seem to be a dominant parameter on the attenuation length (unless the energy is $\gg 1\,\text{eV}$ similar to most alternative experiments.
- No temperature dependence of the attenuation length is found.

The assertion of the last item is based only on few data from literature. For that reason the next section presents the temperature dependent I_C/I_E ratio.

3.1.4 Temperature Dependent Scattering

According to Matthiessens' rule and Mott's prediction there should be a significant difference of the temperature dependence of scattering for the two spin channels. At low temperatures a term $\sim T^2$ in the resistance should occur due to electron scattering at spin waves. At higher temperatures spin disorder should gain importance.

Investigating these effects using TMR/Schottky hybrid junctions ambiguous results are measured. Only a small change in the I_C/I_E ratio is measured. Figure 3.13 shows two plots of the collector current, normalized on the emitter current. The relative current rises with increasing temperature. Due to Mott, the current should drop, because of spin wave scattering.

I_C/I_E is dependent on three effects:

$$I_C/I_E \sim f(\lambda_{\uparrow\downarrow,\uparrow\uparrow}(T), T_{total}(T), P_E(T)) \tag{3.1.2}$$

T_{total} is the total transmission through the Schottky barrier and P_E the spin-polarization of the emitter.

A temperature dependency of the attenuation length is nowhere to be found in the scarce literature on transition metals, but in SVT junctions temperature dependent spin wave scattering has been quantified [131]. These results cannot be approved in this experiment. The I_C/I_E increases at high temperatures. If spin wave scattering would be a dominating effect, this ratio should decrease.

The maximum value of the spin-polarization is found at low temperature. When the spin polarization of the injected current is high, more electrons are collected in parallel alignment of the magnetic layers. This effect should decrease I_C/I_E for high temperature, too.

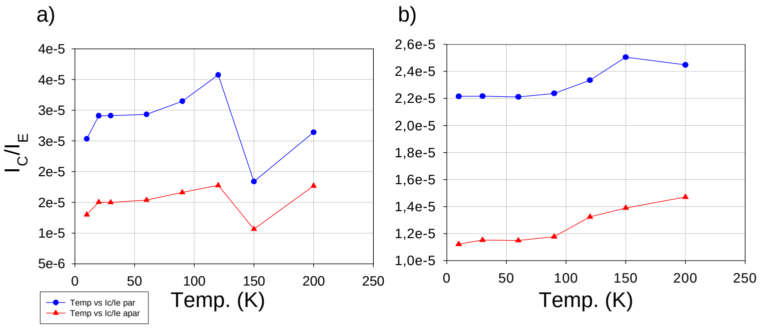

Figure 3.13: Collector current normalized on the emitter current. Plot (a) is for a 4.2 nm and plot (b) for a 5.6 nm Cobalt base. The blue graph is the current in parallel alignment, the red in antiparallel alignment of the electrodes. In plot (a) the electrical connection to the junction seems to be instable, due to the large shift at 150 K. The relative collector current rises with increasing temperature.

The influence of the total transmission should be small, but as seen before the BMC ratio decreases at high temperatures which might be a result of a change of the Schottky-barrier properties. This proposition can be confirmed by figure 3.13: The relative collector current increases at high temperature and thus the BMC ratio is decreased, because this effect is not spin dependent.

3.2 Results from Tunnel-Barrier/Spinvalve/Schottky-Barrier Hybrid Junctions

As already explained in chapter 1.5.3, instead of using the wafer-bonding technique to create a SVT it is possible to integrate a spinvalve between a tunnel-barrier and a Schottky-barrier alternatively. This hybrid junction should have the same spin-filtering properties as the SVT. An interesting advancement of this setup is the possible spin-polarized injection from another ferromagnetic electrode beyond the tunnel-barrier.

The main obstacle in this particular experiment is to get a sufficient transmission through the spinvalve stack. The spinvalve consists of three layers. Layer interfaces induce scattering of electrons which decreases the transmission. Furthermore the total thickness of this stack is at least 10 nm, which reduces the ballistic current at the collector.

For practical reasons it is renounced at this point to optimize an antiferromagnetically coupled spinvalve[6]. The ferromagnetic layers are decoupled using a comparatively thick Copper interlayer instead. This leads to a well defined antiparallel state of the stack, but the thickness of the Copper layer is yet another crucial parameter on the transmission since the attenuation length is about 9-10 nm [94][102].

Figure 3.14 shows a TEM cross section picture of a test stack. According to the calibration, the thicknesses should be:

GaAs / 4.0 nm Co / 3.9 nm Cu /3.5 nm Py / 1.8 nm AlOx. / 7.2 nm Ta

An analysis of the picture shows that all layer thicknesses but the Aluminum oxide thickness are correct. In the TEM picture, this value seems to be 2.3 nm which is too thick. The oxidation process is not adjusted to this thickness. The sputter calibration has not been wrong due to the sample in the other TEM picture (figure 3.1), which has been sputtered on the same day. This could be a hint for a specific property of this stack.

For electrical characterization a slightly different stack has been sputtered:

GaAs / 4.0 nm Co / Cu 4.0 nm / 3.9 nm Py / 1.8 nm AlOx. / 4 nm Py / Cu / Au

The antiparallel state of the spinvalve is approved from other similar stacks by MOKE. The sample is connected to the measurement box, similarly to TMR hybrid junctions. Again the bias is applied at the tunnel-barrier and the ballistic current observed at the second channel of the box.

Unfortunately, the measurement quality is limited by the reproducible low quality tunnel-barrier, which has a tendency to over-oxidize in this stack. The Brinkman-fit delivers $\Phi_B = 1.5\,\mathrm{eV}$, d=20 Å and $\Delta\Phi = 0.08\,\mathrm{eV}$; perfect barriers should have Φ_B =2.5-3 eV and d=18 Å and a low asymmetry. The area resistance was limited to $0.5\,\mathrm{M}\Omega\mu m^2$. For that reason wire bonding directly on the upper electrode has been impossible. Only cautious contacting with Gold tips has been used. This implicates the impossibility of low temperature measurements.

Figure 3.15 shows a major-loop recorded with a hybrid junction. In the tunnel-current (figure 3.15a) only the (in this case non-pinned) TMR major-loop can be

---

[6] A batch of substrate in this thesis has maximum eight 2" wafers. Using substrates from different batches in one experimental series is not possible because the carrier concentration has a large error bar and experiments are only reproducible with wafers from the same batch. For that reason it would be irresponsible waste of material to carry out an optimization series for the exchange coupling each time if the sputter device is equipped for these experiments.

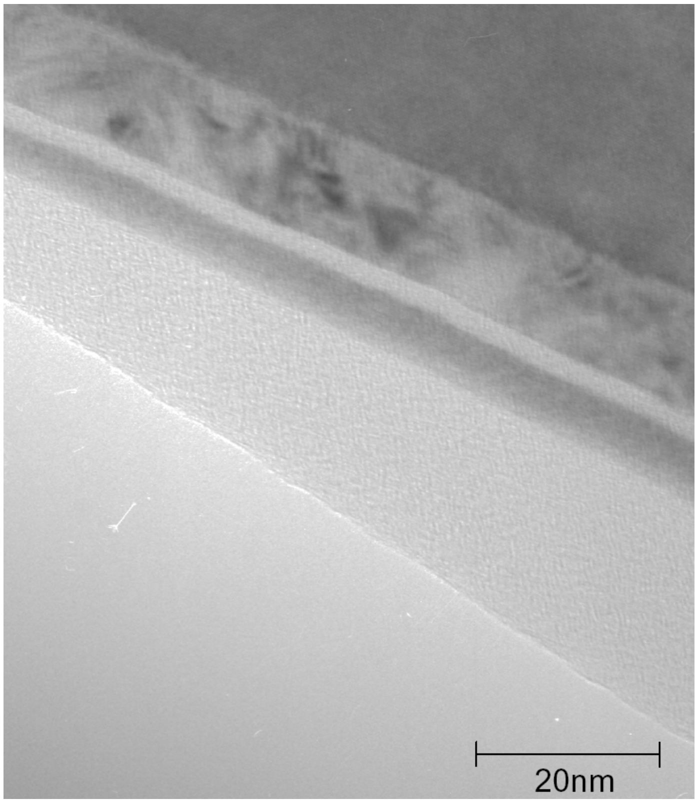

Figure 3.14: TEM cross section picture of a spinvalve in-between Gallium Arsenide and Aluminum oxide layer. The tunnel-barrier is 2.3 nm thick here though it should be 1.8 nm due to the sputter time. Because of the correct calibration (approved in figure 3.1), this must be a specific problem here.

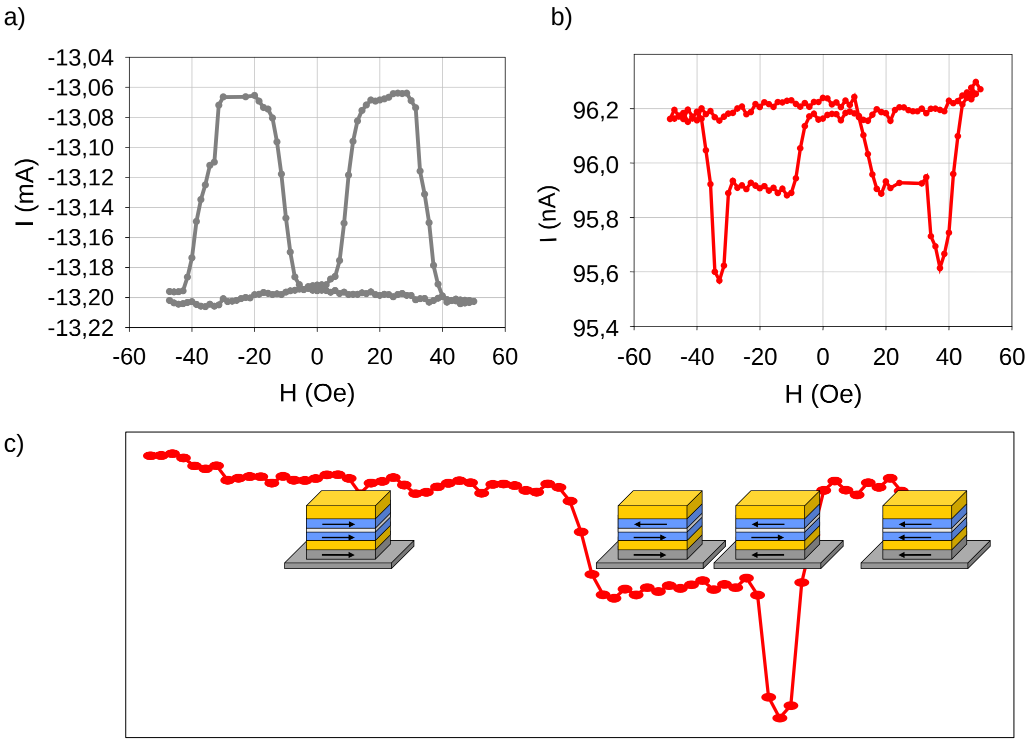

Figure 3.15: Major-loops a of tunnel-barrier/spinvalve/Schottky-barrier hybrid junctions. The tunnel bias has been 500 mV and the measurement has been accomplished at room temperature. a) Loop recorded at the tunnel-barrier. b) Loop recorded in the ballistic current at the Schottky-barrier. The switching of the single layers is visualized in c).

observed. The spinvalve effect is not visible here due to the fact that the Permalloy layer in the base is mostly removed during the Argon ion etching. The complete stack only remains under the patterned tunnel-barrier. Moreover, the spinvalve major-loop would vanish in this plot because the absolute resistance of about 20 Ω of the lateral spinvalve is two orders of magnitude lower than that of the tunnel-barrier.

In the ballistic current (figure 3.15b) an additional state can be observed: Not only the two ferromagnetic layers of the TMR-element but three layers switch independently.

The arrows in figure 3.15c visualize the order of the single layers' switching. The major-loop can be interpreted as follows:

- Starting the major-loop at -60 Oe all layers are parallel.
- The effect ratio increases at +5 Oe in the tunnel *and* the ballistic current. So the upper TMR electrode must have switched. The spinvalve is still aligned in parallel.
- The ballistic ratio increases again at 32 Oe to its maximum. Now the spinvalve must have switched. The TMR is unchanged, so the lower spinvalve layer must have switched.
- The TMR- and the BMC-ratio start decreasing again at 35 Oe. The upper spinvalve electrode (respectively the lower TMR-electrode) has switched. All layers are parallel again.

The maximum effect amplitude is observed only in a small interval between ≈32 Oe and ≈35 Oe. It cannot be proved that all layers are practically aligned perfectly antiparallel in this state, but the existence of the state is clearly proved.

Due to the magnetic properties of the stack it is not possible to observe more states of such a stack. With an antiferromagnetically pinned upper TMR-electrode or an antiferromagnetically coupled spinvalve it would be possible to obtain an additional state where the magnetic tunnel junction is magnetized in parallel position and the spinvalve in antiparallel alignment; only the lowest layer is switched.

The ballistic current is more than 5 orders of magnitude lower than the tunnel current. This value is consistent with TMR/Schottky-hybrid junctions with comparable base thickness. The two additional interfaces inside the spinvalve stack seem to have a minor effect on scattering.

Leak currents decrease the ballistic effect ratio at room temperature. The TMR-ratio is only about 1.1% and the BMC-ratio about 1.4%. The ballistic effect ratio again exceeds the conventional ratio.

Chapter 4

Ballistic Electron Emission Microscope Experiments

This chapter contains the results of a fruitful cooperation between the *Technical University* in Vienna, department of *Festkörperelektronik* and the *Universität of Bielefeld, Department of Physics, D2 Nano Device Group.* Non-patterned spinvalve samples, prepared and characterized magnetically and electrically in Bielefeld have been investigated by BEEM in Vienna.

The experimental idea is similar to the one of the SVT-junction, but the electrons are injected by a STM tip instead of a Schottky-barrier. For that reason the injection (vacuum-) barrier is almost perfect.

4.1 Fabrication

BEEM spinvalve samples have to fulfill two major specifications:

- sufficiently thin stack
- clear switching behavior of the spinvalve

The injected (STM) tunnel current of a BEEM is small compared to the plane currents in hybrid junctions. For that reason the net thickness of all layers should be as small as possible to guarantee a sufficiently large collector current. On the other hand, the spinvalve should have a well defined antiparallel state and a protective layer to avoid oxidation on top. A compromise of these converse conditions has to be found.

Chosen substrate and preparation method is the same as described in section 2.1.1. The deposition is obtained in the sputter apparatus described in chapter 2.1.2. As a compromise for the necessary specifications the following stack is used:

4.5 nm Co/ 4.2 nm Cu / 3.5 nm Py /4.0 nm Au,

sputtered on Silicon doped (100) Gallium Arsenide. During the sputtering process, a magnetic field is applied at the sample. It is aligned along the (100) direction of the substrate. In that way, anisotropy induced by the substrate and easy axis induced by the magnetic field have the same direction.

The 4 nm Gold layer is the protection against oxidizing. A 4 nm Gold film is the thinnest definitely entirely homogeneous layer which can be sputtered. For the BEEM experiment the Gold thickness is not crucial, the specific electron attenuation length is comparatively high (λ=100-130 Å) at room temperature, determined by BEEM [109] [110]), but the lateral GMR vanishes with thicker films completely due to the decreasing resistance. Moreover, the tip can be damaged when oxidized areas are on the sample: When the current at such an area decreases the tip is approached to the sample until it crashes into the surface.

4.2 Magnetic and Electrical Characterization

In this case electrical characterization consists of recording major-loops in direction of the easy axis of the induced anisotropy and in 90° rotated direction (just for completeness reasons).

Figure 4.1 shows a typical GMR major-loop in easy axis direction. The GMR ratio of 1.6% is as expected comparatively low; the thick Copper and Gold layer dominate the lateral conductance. More important for this experiment is the switching behavior of the magnetic films. The coercivity of each layer can only be anticipated from figure 4.1. A MOKE measurement delivers the exact coercive fields of each layer and is stringent.

MOKE measurements ensure the magnetic separation of the Cobalt and the Permalloy layer. Again the data is recorded in easy axis and hard axis direction. Because of the thin protection layer MOKE is able to characterize this stack excellently.

Figure 4.2 shows a typical MOKE graph in direction of the easy axis of the anisotropy. The coercivity of the first layer is about 5 Oe, the second switches at 35 Oe. The graph proves that there are no more switching processes between 5 to 35 Oe which is an indicator for a good antiparallel alignment.

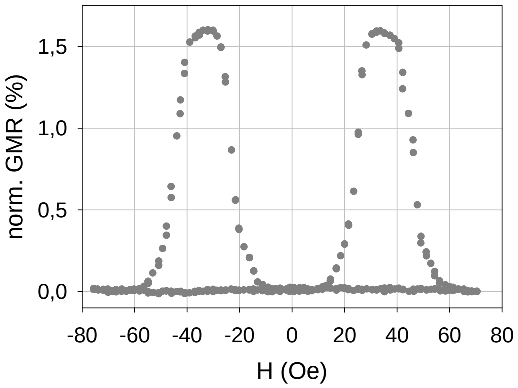

Figure 4.1: GMR graph of non-patterned a spinvalve, recorded with 50 mV Bias. The coercive fields can be anticipated.

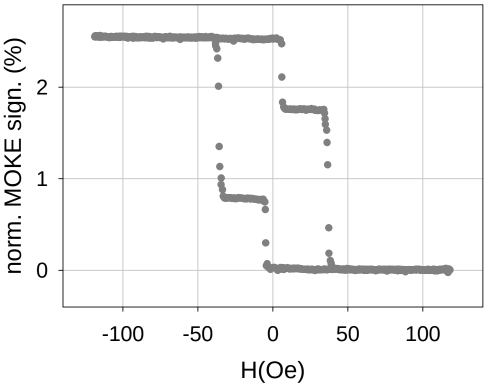

Figure 4.2: Magnetization characterization of the spinvalve obtained by MOKE. At 5 Oe and 35 Oe switching processes are monitored. Between theses coercivities the magnetic layers are magnetized antiparallel. A decrease in the BEEM signal should be monitored if the magnetic field is applied between 5 Oe and 35 Oe.

4.3 BEEM Setup

The BEEM is equipped with a liquid Helium cryostat which can apply temperatures between 4.2 K and room temperature. Two Helmholtz coils are implemented to the microscope to apply the magnetic field. Major- and minor-loops can be accomplished during the scanning or during spectroscopy. A schematic sketch of the setup is shown in figure 4.3.

A specially cut Gold wire is used as the STM tip. It is sharpened by a scalpel with two cuts, performed in an angle of 90°. Before any BEEM spectroscopy is started one fast STM scan with low resolution is carried out. By doing so, potentially existing double tips can be repaired because the tip shape changes slightly during such a process. Subsequently the tip is evaluated by a scan with high resolution.

The signal from the modified STM head (shown in figure 4.4) is submitted by shielded coaxial wires through a 1.5 m long rod to the electronics. Both signals (STM and BEEM) have to be amplified before they are evaluated by the applied electronics. For practical reasons, it cannot be amplified near the measurement but at the end of the rod, outside the cryostat. This leads to capacities which limit the speed of a measurement due to crosstalk.

The STM signal is increased by a standard OP-circuit. In contrast the amplification of the BEEM signal is non-trivial. The sample is on floating potential because the tip is grounded. For that reason, the amplification has to be done by a special floating electrometer, designed by *R. Heer* [160]. This instrument shows a bias independent output offset. Noise and thermal drift are low. The resolution is up to $\pm 20\,fA$ and it can also be used for fA measurements related to the ground. For a detailed description refer to [160].

The presented BEEM measurements at room temperature are carried out in ambient atmosphere in contrast to most STM experiments in literature [161]. The applied tunnel current must not fall below a threshold of $20\,nA$ to ensure a sufficient high ballistic signal at the collector. Tunnel voltages $V_T < 1.2\,V$ are too low to guarantee a current detection in antiparallel configuration of the magnetization. An antagonistic problem occurs here: The signal in antiparallel configuration should be as small as possible for good BMC ratios but it has to be sufficiently high for detection.

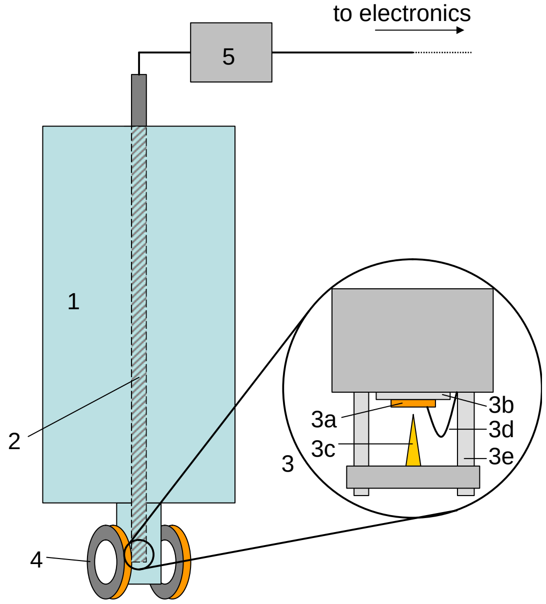

Figure 4.3: Schematic sketch of a BEEM setup: Inside the liquid Helium cryostat (1) a rod (2) is attached, equipped with the STM head (3) at its end. The sample (3a) is fixed using conducting silver on the sample-holder (3b) which can be moved by piezo crystals. All edges of the samples have to be accurately cleaved beforehand to avoid shortcuts at that point. The sample holder has a contact to collect the ballistic current. The tip (3c) is a sharpened Gold wire. The sample surface (the base, respectively) is contacted by a gold wire (3d), which is carefully glued by Indium to prevent destruction of the interface. The tip can approach the sample by a special piezo-electric mechanism (3e). Outside the cryostat, two Helmholtz coils (4) apply the homogenous magnetic field. Signals from the tip and the collector are submitted by shielded wires inside the rod. Two measurement boxes (5) at the end of the rod (outside the cryostat) edit the signal. The first is an amplifier for the STM signal. The second is a special floating electrometer for the non-grounded BEEM signal.

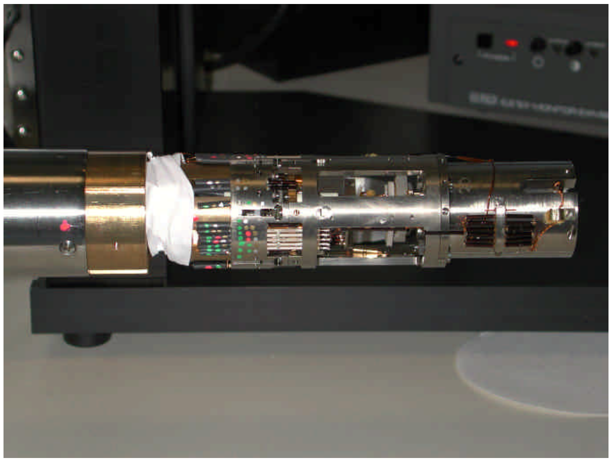

Figure 4.4: OMICRON scanning probe microscope used for BEEM experiments. This device is additionally equipped with an AFM.

4.4 Results

BEEM is used in this thesis for three applications:

- spectroscopy of the ballistic transmission in a spinvalve with different magnetic configurations of the layers
- magnetic major-loops of ballistic electrons
- mapping of ballistic currents versus the topography

Spectroscopy and magnetic major-loops have been accomplished at different temperatures between 10 K and room temperature. Topography scans have recently been carried out at room temperature. Due to the small currents, accurate mapping is difficult at low temperatures for the comparatively thick stacks presented in this thesis. An accurate BEEM picture at room temperature takes about six hours. Low temperature scans would take much longer.

Before any scan the samples are saturated by the Helmholtz coils, so that the magnetic configuration is defined in parallel.

4.4.1 Spectroscopy and Magnetic Major-Loops

Figure 4.5(a) shows the collector current versus the tunnel bias at 0 Oe and at 26 Oe magnetic field[1]. This spectrogram visualizes the different transmission in antiparallel (26 Oe) and parallel configuration (0 Oe).

Figure 4.5 (b) is a major-loop recorded in the ballistic current. Using a tunnel bias $V_T = 1.5\,V$ at room temperature the collector current in parallel magnetization alignment is $I_{C,P} = 0.7\,pA$ and $I_{C,AP} = 0.1\,pA$ in antiparallel alignment; thus a BMC ratio of 600% is observed. The signal-to-noise ratio is high due to the low collector current. Related recent experiments by Lodder *et al.* show an analogical behavior [162].

Figure 4.6 shows two typical major-loops recorded at 250 K and at 10 K. The approximate absence of leak currents at the Schottky-barrier reduces the total current to the net ballistic current at 10 K. This fact and the higher spin-polarization lead to less noise and larger ratio. Leak currents attenuate the signal because the total currents in parallel and antiparallel magnetic alignment are both increased.

To observe this systematically, I/V-curves are recorded in the parallel and the antiparallel state for different temperatures and the MC-ratio is calculated bias dependent on this, see figure 4.7. Again, when the temperature is decreased the signal increases at the cost of the total current. Additionally, this spectroscopy contains the energy dependence of the MC-ratio.

Equation 1.5.2 can be used with the attenuation lengths obtained in chapter 3.1 and the values from Parkin *et al.* to estimate a maximum BMC ratio of about 1400% for this particular stack [10]. Including the 8% error bar of the sputter calibration the effect amplitude is predicted to be 1400%±500%. The experimental value is 800% at 10 K, which is in good agreement to the prediction, refer to figure 4.7.

4.4.2 Topography and BEEM Pictures

Figure 4.8 shows the difference between parallel and antiparallel alignment of the magnetic films in a typical BEEM picture. An external magnetic field switches the magnetization of one layer during the scan. While the topographic STM picture remains unchanged the BEEM picture changes abruptly when the coercivity of one layer is crossed and the spinvalve is in antiparallel configuration.

---

[1] Though the sample is the same which is characterized in the MOKE graph figure 4.2 the coercivity is different. This might have two reasons: First, the field in the cryostat is not measured but calculated from the (calibrated) current. Second, the angle between coils and easy axis of the anisotropy might be chosen slightly different in both measurements. It is difficult to make a better alignment than ±5° in both cases.

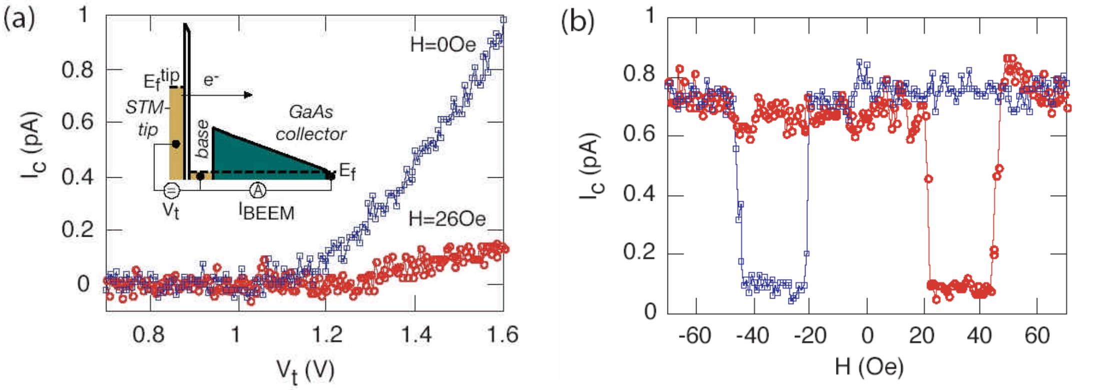

Figure 4.5: (a) Collector current versus tunnel bias with constant magnetic fields 0 Oe and 26 Oe at room temperature. When no magnetic field is applied and the sample has been saturated before, the magnetization of both layers is aligned parallel; the collector current increases with rising bias. In antiparallel configuration, the collector current increases less; more electrons scatter in the base, loose energy, and cannot pass the Schottky-barrier. Additionally, a schematic sketch of the setup is shown.(b) Collector current versus magnetic field with constant bias of 1.5 V. The major-loop shows an effect amplitude of 600%

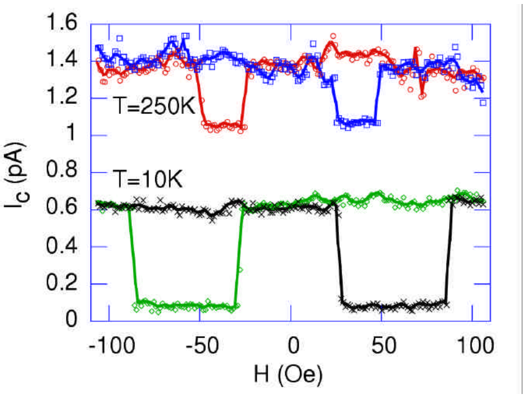

Figure 4.6: Two typical major loops at 250 K and 10 K, both recorded with $V_T = 1.5\,V$ and $I_T = 20\,nA$. The noise is less at 10 K because of the decrease of thermal leak currents.

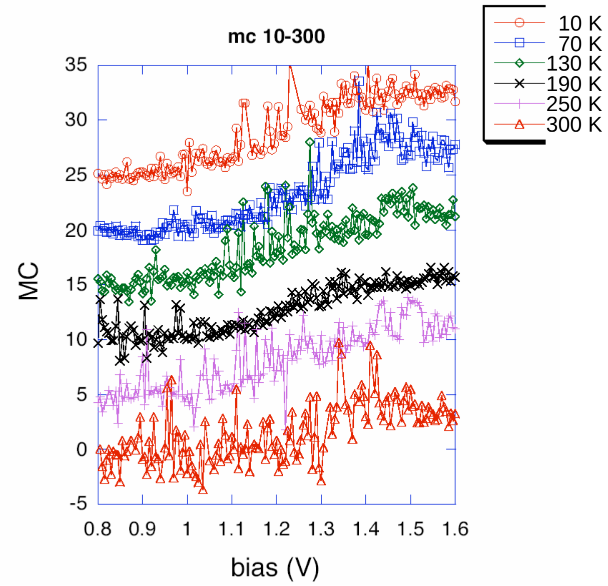

Figure 4.7: Local magneto current MC plotted as a function of the tunneling voltage at temperatures of T=10K, 70K 139K, 190K, 250K and T=300 K, respectively. An offset was added for better viewing. At room temperature the maximum BMC ratio is 400%, at 10 K 800%.

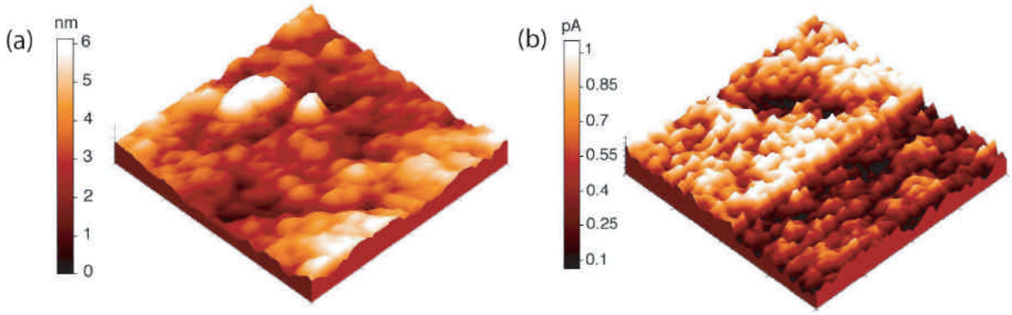

Figure 4.8: $400 \times 400\,nm^2$ topography and BEEM picture of spinvalve sample ($V_T = 1.8\,V, I_T = 20\,nA, T = 300K$). The image resolution is ≈1 nm per pixel. During the scanning process the magnetization of one layer is switched by an external magnetic field. (a) Topography. No change can be observed. (b) Corresponding collector current picture. The switching process is visible.

Dust on top of the sample, to be seen in the topography, shields the current and can be identified as a "shadow" in the BEEM picture, but only in the part where both layers are magnetized in parallel. Moreover this picture demonstrates the resolution of this technique which is not yet on its limit at this point. Obtaining better high resolution pictures is at first only a question of time with regard to the measurement, which might be limited by external properties.

In figure 4.9 magnetic domains formed at a film imperfection are shown. The four pictures are a series recorded during a minor-loop[2]. The imperfection seems to be a scratch, due to the locally high transmission in any magnetic configuration of the spinvalve. The resolution is ≈8 nm per pixel.

The minor-loop is started at a high field so that both layers are magnetically aligned in parallel (a). When the magnetic field is near the coercivity of the magnetic soft layer, domains are formed at the imperfection (b). The switching process is constricted by local fields. When a critical magnetic field value is passed, the whole layer switches and the spinvalve is in antiparallel alignment (c). Nearly no current can pass the Schottky-barrier and the BEEM picture is dark. The field is decreased again

---

[2] Scanning one BEEM picture in good quality and high resolution takes hours of time. For that reason, the field has not been changed constantly, as in a common minor-loop, but gradually to reasonable values.

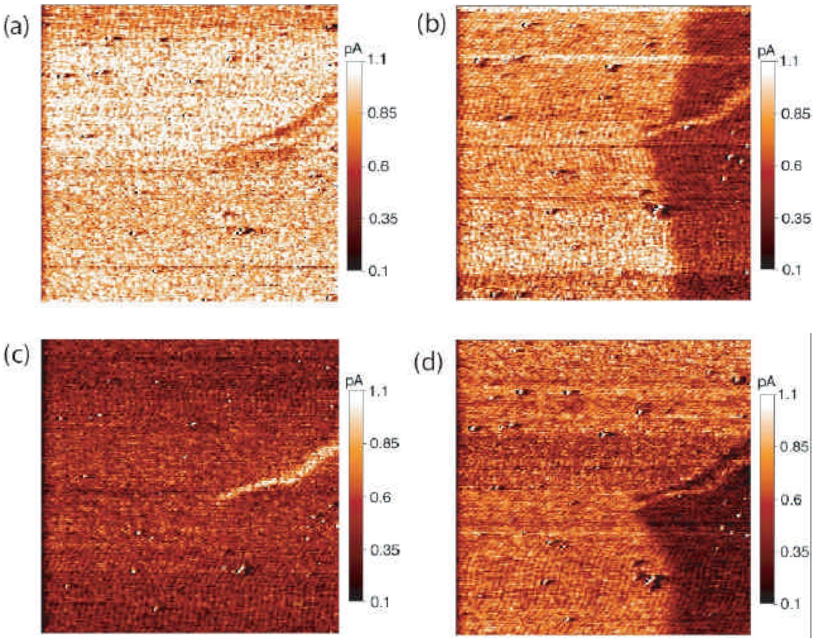

Figure 4.9: Series of four $4 \times 4\,\mu m^2$ BEEM pictures of a spinvalve sample, recorded during a minor-loop cycle ($V_T = 1.8\,V, I_T = 20\,nA, T = 300\,K$). A film imperfection captures magnetic domains. (a) Both layers are magnetized in parallel (angle 0°) and the magnetic field is sufficiently high. The imperfection does not affect the magnetization. (b) Near the coercive field of the magnetic soft layer a magnetic domain is formed. The scratch pins the magnetization by its stray fields. From the reduced transmission through the spinvalve, visualized by the darker color, the mean angle between the layers' magnetizations can be approximated. The magnetization of the layers has rotated ≈ 25°. (c) In antiparallel magnetization alignment (angle 180°), the imperfection is well visible but does not affect the surrounding area. (d) Decreasing the magnetic field leads again to the formation of a domain. The alignment of the remaining area does not seem to be perfectly parallel, due to the low transmission (compared to picture (a)). The mean angle between the magnetizations can be approximated from the collector current to be at ≈ 65°.

and crossing the critical field leads to domain formation again (d). The transmission is not the same as in picture (b) because the magnetization of the film is not saturated; as mentioned above the sample is saturated prior to each measurement by applying a sufficiently high magnetic field. The mean angle between the magnetic layers can be approximated from the transmission.

The investigated domain is a result of a scratch in the film. Stray field effects, which are known from the edges of patterned magnetoresistive junctions, affect the magnetic layers during the switching process. One layer is locally pinned by these fields while the other is aligned along the external field. This leads to a locally antiparallel configuration of the spinvalve; the transmission is low and the BEEM picture is dark at that point. The domain wall is a Neél wall. The energy to build up a Neél wall is less than the energy of a Bloch wall inside such a thin film [163]. Furthermore, a Bloch wall would require ≈ 300 times the lattice constant to change the magnetization direction 180° [164]; this should be visible as a continuous change in the contrast, disturbed on a distance >50 nm.

The only comparable experiments in the literature are BEEM spectra of spinvalves by *Haq et al.* and BEMM domain mapping of a Co/Cu/Co trilayer by *Rippard et al.* [162] [127] [108].

Haq's experiment is similar to the presented spectra; the results are similar, too. In contrast to the spinvalve used in this thesis, the collector is a silicon substrate, which is covered with 7 nm Gold. By doing so, a high quality Schottky-barrier is fabricated, but the total transmission is reduced. For that reason, the signal-to-noise ratio of the major-loop is comparatively low.

In Rippard's experiment BEMM pictures of a 3 nm Co/4.5 nm Cu/3 nm Co/0.9 nm Cu/7.5 nm Au stack on silicon are taken at different magnetic states. The formation of domains is visible near the coercive field of the films. The transmission is evaluated and compared with that of trilayers with other Cobalt thicknesses. From the results attenuation lengths in Cobalt are calculated, see Table 3.1. The resolution of the images presented in this thesis and Rippard's BEMM pictures is approximately the same. The BMC ratios measured by BEEM in this thesis, also support the measured attenuation length values.

Chapter 5

Summary

The use of modified MR-junctions as ballistic electron injection tools is outlined in this thesis.

First TMR/Schottky hybrid junctions on Gallium Arsenide are presented. These junctions can be fabricated reproducibly with varying base thickness. They are used for investigations on the electron transport in transition metals. It is shown that the ferromagnetic base electrode spin-filters the electrons. The ballistic current decays exponentially in this layer. The resulting BMC-ratio is in the expected magnitude. Spin-attenuation lengths in Cobalt could be quantified: $\lambda_{\uparrow\uparrow} = 60 \pm 9\,\text{Å}$ and $\lambda_{\uparrow\downarrow} \leq 20\,\text{Å}$ at 10 K and 1.2 V bias. This result is consistent with comparable experiments on Cobalt (BEEM, GMR). It is shown, that the attenuation lengths are bias dependent. Also the transmissions into the substrate comply with other publications.

The TMR/Schottky hybrid experiment is a good method to determine spin-polarized ballistic currents and characterize them. These junctions could be utilized as sources of spin-polarized currents in possible applications. The spin-polarization of the current inside the base layer can converge to 100%, dependent on the thickness of the base. It remains to be shown if this current is really *injected* in the spin-polarized way into the semiconductor. This experiment should also deliver the sustainment inside the substrate.

The fabrication of tunnel-barrier/spinvalve/Schottky-barrier hybrid junctions has been executed in almost the same manner as the fabrication of the TMR/Schottky hybrid junctions. In contrast to Parkin's MTT- and Lodder's SVT-junction this thesis presents a setup where the current is injected spin-polarized into a spinvalve. Three independent states of the ballistic current amplitude can be observed, which correspond to the two TMR-states and an additional spinvalve state. Quantitatively the results are not different to the room temperature results of TMR/Schottky hybrid junctions. Both suffer from leak currents outside cryogenic ambient conditions. The multiple states of the collector current are another interesting improvement of the basic idea.

BEEM-sample preparation has been made without lithography. BEEM is presented as a high resolution microscope and spectroscope to observe several ballistic effects and to map magnetic domains in magnetoresistive junctions, here spinvalves. It delivers major-loops in the ballistic current, recorded in sub-nanometer areas of a sample [162][165].

In this thesis BEEM spectra at different temperatures are shown. The BMC ratio of the collector current is up to 800%, which corresponds well with the theory. Again, the bias dependence of the BMC ratio is demonstrated. The mapping of magnetic domains has also been shown. The maximum pixel resolution of the presented BEEM images is about 1 nm at a current resolution of 10 fA.

Chapter 6

Outlook

The essential requirements for spintronic semiconductor devices are:

- Efficient injection of spin-polarized electrons into a semiconductor
- Negligible spin-depolarization during transport
- An electronic detection element

All these requirements should be fulfilled by sub-micron scale junctions.

This thesis concentrates on the first prompt. Consequently an interesting continuation of this work would be the investigation and maybe application of the high spin polarized current inside the semiconductor. At first the spin diffusion length in the substrate could be determined. Until now all experiments concerning this topic have been accomplished using optical detection. The degree of circular polarization of the electroluminescence emitted by a LED allows the direct determination of the spin polarization of the injected carriers [166][167]. The polarization of the current can be accomplished using dilute magnetic semiconductors or ferromagnetic layers grown on the substrate for those experiments [19][168]. In this setup the analyzer is grown in the Gallium Arsenide and can thus be located arbitrary near to the emitter without complex lithography.

Alternatively a TMR/Schottky hybrid junction could be integrated into a setup, similar to that proposed by *Das* and *Datta* [14]; for a schematic sketch of this upgraded configuration see figure 6.1.

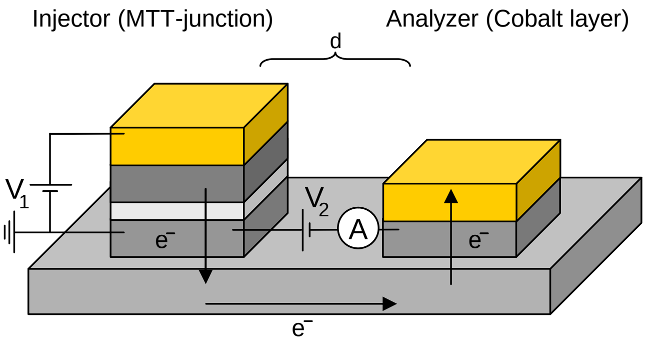

Figure 6.1: Schematic sketch of a setup to analyze spin diffusion. The TMR bias V_1 injects the current into the substrate. V_2 is a small bias to force the electrons to the analyzer. The distance d, the current has to pass through the semiconductor, can be varied to measure the diffusion length. The MR-ratio measured at the analyzer can be used to quantify the spin-polarization. In a Das/Datta transistor a Schottky gate would be between the injector and the analyzer.

The referred experiment is highly discussed due to the search for a possible solution for the *fundamental obstacle* for electrical spin injection from a ferromagnetic metal into a diffusive semiconductor, demonstrated by *Schmidt et al.* [18]. As mentioned in the preface, lateral spin transistor devices show a degree of spin-polarization limited to $\approx 0.1\%$ [15][16][17]. In the literature two possible approaches are mentioned to circumvent this dilemma and build a working spin transistor:

- Injecting with 100% spin-polarization.
- Adapting density of charge carriers.

Schmidt concludes from his results that "...for efficient spin injection one needs a contact where the spin-polarization is almost 100%"; he concentrates on the first item. E.g. half-metallic alloys like Nickel Manganese Antimony have been proposed as a candidate to inject directly [169]. Calculations on the band-structure of this Heusler-alloy predict a bulk spin-polarization P=100% as an intrinsic property [170]. However experimentally obtained values for P are 28% in a tunnel junction experiment and 58% measured with superconducting point contacts [171] [172]; this is no crucial advantage to simple ferromagnetic layers. Recent TMR experiments confirm these results [173]. In these works one electrode of a MTJ has been a Heusler-alloy.

The TMR-ratio at 10 K is 95%; assuming 50% spin-polarization for the metal electrode as an approximation (Cobalt Iron 70/30, refer to [20][174]) the spin-polarization of the Heusler alloy can be estimated as 66% in this case, according to equation 1.1.7. With 100% spin-polarization 200% TMR-ratio would be expected. Even if a perfect Heusler-alloy would be fabricated, there are new obstacles in this approach: To fabricate such samples an annealing process during the deposition is necessary. The substrate is heated up to 450° C to achieve the necessary Heusler phase, for details refer to [173]. It might be implausible that the half-metal/semiconductor interface is of sufficient quality in such a junction because of diffusion processes; nevertheless *de Groot et al.* are confident that it is possible to restore the Heusler properties at the interface by proper engineering [169].

Rashba's proposal concentrates on the second item: He suggests the preparation of a tunnel barrier between metal and semiconductor [175]. The reduced injected (tunnel-) current effects an adaption of the charge carrier densities. Due to the difficult fabrication of this junction until now no experimentally breakthrough has been published. The controlled reproducible oxidation directly on a semiconductor substrate is challenging because of charge effects during the process. Furthermore the barrier must be sufficient thick and homogeneous for an eligible injection.

The highly polarized and small current in TMR/Schottky hybrid junctions or in BEEM experiments might be an alternative approach to this experiment. Both approaches, small current and moreover high polarization, can be achieved this way. Furthermore the injection energy is above Fermi level. First work on this has recently been started by *Lars Tiemann* [136]. His thesis mainly concentrates on the fabrication of Rashba-junctions and similar setups. It is shown that for ambient temperature and temperatures above spin-polarized currents can be detected in the semiconductor, but again with weak effect-ratio. First steps for the proposed TMR/Schottky hybrid junctions device have also been accomplished.

The main challenge to perform a spin-injection experiment is the fabrication of an appropriate analyzer. Usually, it is a ferromagnetic layer which should have different coercivity than the layers of the hybrid junction. This can be achieved for instance by utilizing shape anisotropy, which does not require additionally sputter but lithography steps; for practical reasons lithography is the favored process.

In fact the analyzer is the weak point in every spin injection experiment, especially in lateral setups like the Das/Datta-transistor. For that reason the LED-experiment has already been successfully upgraded with a TMR/Schottky hybrid junction as injector, as mentioned in the preface [13].

Alternatively to complete LEDs, single quantum wells could be integrated into the substrate. BEEM experiments on quantum wells with unpolarized current have already been accomplished by the cooperating group in Vienna [176]. Burying those structures under MTT-junctions, hybrid junctions or alternatively spinvalves for BEEM investigations is an interesting advancement in spintronics: The spin-polarized injection of currents into single quantum wells.

For applications it would be interesting to transfer the existing junctions to Silicon substrates. The spin relaxation time is orders of magnitude higher than in Gallium Arsenide. Optical detection by LEDs is difficult in Silicon, but in this case a magnetic analyzer might be more effective than in Gallium Arsenide. Furthermore Silicon based devices are more attractive for industrial applications due to the long experience with this material.

Bibliography

[1] Grünberg, P., Schreiber, R., Pang, Y., Brodsky, M. B., and Sowers, H. *Phys. Rev. Lett.* **57**, 2442 (1986).

[2] Jullière, M. *Phys. Lett. A* **54**, 225 (1975).

[3] Wolf, S. A., Awschalom, D. D., Buhrman, R. A., Daughton, J. M., von Molnar, S., Roukes, M. L., Chtchelkanova, A. Y., and Treger, D. M. *Science* **294**, 1488 (2001).

[4] Prinz, G. A. *J. Magn. Magn. Mat.* **200**, 57 (1999).

[5] Levy, P., Zhang, S., and Fert, A. *Phys. Rev. Lett.* **65**, 1643 (1990).

[6] Johnson, B. and Camley, R. *Phys. Rev. B* **44**, 9997 (1991).

[7] Barthelemy, A. and Fert, A. *Phys. Rev. B* **43**, 13124 (1991).

[8] Dieny, B. *Europhys. Lett.* **17**, 261 (1992).

[9] Mott, N. *Proc. R. Soc.* **156**, 368 (1936).

[10] van Dijken, S., Jiang, X., and Parkin, S. S. P. *Phys. Rev. B* **66**, 094417 (2002).

[11] van Dijken, S., Jiang, X., and Parkin, S. S. P. *Appl. Phys. Lett.* **82**, 775 (2003).

[12] Bell, L. D., Kaiser, W. J., Hecht, M. H., and Grunthalner, F. J. *Appl. Phys. Lett.* **52**, 278 (1988).

[13] Jiang, X., R.Wang, van Dijken, S., Shelby, R., Macfarlane, R., Solomon, G. S., Harris, J., and Parkin, S. S. P. *Phys. Rev. Lett.* **90**, 256603 (2003).

[14] Das, B., Miller, D. C., and Datta, S. *Phys. Rev. B* **39**, 1411 (1989).

[15] Lee, W. Y., Gardelis, S., Choi, B.-C., Xu, Y. B., Smith, C. G., Barnes, C. H. W., Ritchie, D. A., Linfield, E. H., and Bland, J. A. C. *J. Appl. Phys.* **85**, 6682 (1999).

[16] Hammar, P. R., Bennet, B. R., Yang, M. J., and Johnson, K. *Phys. Rev. Lett.* **83**, 203 (1999).

[17] Filip, A. T., Hoving, B. H., Jedema, F. J., van Wees, B. J., Dutta, B., and Borghs, S. *Phys. Rev. B* **62**, 9996 (2000).

[18] Schmidt, G., Ferrand, D., Molenkamp, L. W., Filip, A., and van Wees, B. J. *Phys Rev. B* **62**, R4790 (2000).

[19] Oestreich, M., Hübner, J., Hägele, D., Klar, P. J., Heimbrodt, W., Rühle, W. W., Ashenford, D. E., and Lunn, B. *Appl. Phys. Lett.* **74**, 1251 (1999).

[20] Thomas, S. P. N. A. *Ph.D. Thesis.* Universität Bielefeld, (2003).

[21] Miyazaki, T. and Tezuka, N. *J. Magn. Magn. Mat.* **139**, L231 (1995).

[22] Moodera, J. S., Kinder, L. R., and Wong, T. M. *Phys. Rev. Lett.* **74**, 3273 (1995).

[23] Miyazaki, T. and Tezuka, N. *J. Magn. Magn. Mat.* **151**, 403 (1995).

[24] Schrag, B. D., Anguelouch, A., Xiao, G., Trouilloud, P., Lu, Y., Gallagher, W. J., and Parkin, S. *J. Appl. Phys.* **85**, 5828 (1999).

[25] Ghallager, W. J., Parkin, S. S. P., Lu, Y., Bian, X. P., Marley, A., Roche, K. P., Altman, R. A., Rishton, S. A., Jahnes, C., Shaw, T. M., and Xiao, G. *J. Appl. Phys.* **81**, 3741 (1997).

[26] Lu, Y., Altman, R. A., Marley, A., Rishton, S. A., Trouilloud, P., Xiao, G., Ghallager, W. J., and Parkin, S. S. P. *Appl. Phys. Lett.* **70**, 2610 (1997).

[27] Sommerfeld, A. and Bethe, H. *Handbuch der Physik.* ed. by H. Geiger and K. Schell, (J. Springer Verlag, Berlin, 1933).

[28] Bardeen, J. *Phys. Rev. Lett.* **6**, 51 (1961).

[29] Messiah, A. *Quantenmechanik I*, chapter 6, 203. de Gruyter (1976).

[30] Simmons, J. G. *J. Appl. Phys.* **34**, 1793 (1963).

[31] Simmons, J. G. *J. Appl. Phys.* **34**, 2581 (1963).

[32] Brinkman, W. F., Dynes, R. C., and Rowell, J. M. *J. Appl. Phys.* **41**, 1915 (1970).

[33] Bratkovky, A. M. *Phys. Rev. B* **56**, 2344 (1997).

[34] Press, W. H., Flannery, B., Teukolsky, S., and Vetterling, W. *Numerical Recipes in C.* Camebridge University Press, (1988).

[35] Schmalhorst, J. *Ph.D. Thesis.* Universität Bielefeld, (2001).

[36] Andreev, A. F. *Zh. Eksp. Teor. Fiz* **46**, 1823 (1964). engl. transl.: Sov. Phys. JETP 19, 1228 (1964).

[37] Fadley, C. S., Shirley, D. A., Freeman, A. J., Bagus, P. S., and Mallow, J. V. *Phys. Rev. Lett.* **23**, 1397 (1969).

[38] de Teresa, J. M., Bartélémy, A., Fert, A., Contour, J. P., Lyonnet, R., Montaigne, F., Seneor, P., and Vaurès, A. *Phys Rev. Lett.* **82**, 4288 (1999).

[39] Papaconstantopoulos, D. A. *Handbook of the Band Structures of Elemental Solids*. Plenum, New York, (1986).

[40] Stearns, M. B. *J. Magn. Magn. Mater.* **5**, 167 (1977).

[41] Moodera, J. S. and Mathon, G. *J. Magn. Magn. Mater.* **200**, 248 (1999).

[42] Kämmerer, S., Heitmann, S., Meyners, D., Sudfeld, D., Thomas, A., Hütten, A., and Reiss, G. *J. Appl. Phys.* **9**, 7945 (2003).

[43] Wang, D. X., Nordman, C., and Daughton, J. M. *IEEE Trans. Mag.* **40**, 2269 (2004).

[44] http://www.almaden.ibm.com/st/magnetism/ms/index.shtml.

[45] Parkin, S. S. P., Bhadra, R., and Roche, K. P. *Phys. Rev. Lett* **66**, 2152 (1991).

[46] Parkin, S. S. P., More, N., and Roche, K. P. *Phys. Rev. Lett.* **64**, 2304 (1990).

[47] Yafet, Y. *J. Appl. Phys.* **61**, 4058 (1987).

[48] Yafet, Y. *Phys. Rev. B* **36**, 3948 (1987).

[49] Bruno, P. *Phys. Rev. B* **52**, 411 (1995).

[50] Stiles, M. D. *Phys. Rev. B* **48**, 7238 (1993).

[51] Edwards, D. M., Mathon, J., Muniz, R. B., and Phan, M. S. *Phys. Rev. Lett.* **67**, 493 (1991).

[52] Bruno, P. *Magnetische Schichtsysteme*, chapter Theory of Interlayer Exchange Coupling, B8.1–B8.39. 30. IFF-Ferienkurs, Forschungszentrum Jülich (1999).

[53] Baibich, M. N., Broto, J. M., and Fert, A. *Phys. Rev. Lett.* **61**, 2472 (1988).

[54] Binasch, G., Grünberg, P., Sauerberg, F., and Zinn, W. *Phys. Rev. B* **39**, 4828 (1989).

[55] Campbell, I. and Fert, A. *Ferromagn. Mater.*, volume 3. (1982).

[56] Reiss, G., Brückl, H., and Hütten, A. *Magnetische Schichtsysteme*, chapter GMR Experimente, B3.1–B3.30. 30. IFF-Ferienkurs, Forschungszentrum Jülich (1999).

[57] Heitmann, S. *Ph.D. Thesis.* Universität Bielefeld, (2004).

[58] Dieny, B., Speriosu, V. S., Parkin, S. S. P., Gurney, B. A., Wilhoit, D. R., and Mauri, D. *Phys. Rev. B* **43**, 1297 (1991).

[59] Pratt, W. P., Lee, S. F., Slaughter, J. M., Loloee, R., Schroeder, P. A., and Bass, J. *Phys. Rev. Lett.* **66**, 3060 (1991).

[60] Schroeder, P. A., Bass, J., Holody, P., Lee, S. F., Loloee, R., Pratt, W. P., and Yang, Q. *NATO ASI series B: Physics* **309**, 129 (1993).

[61] Braun, F. *Ann. Phys. Chem.* **153**, 556 (1874).

[62] Schottky, W. *Z. Phys.* **113**, 367 (1939).

[63] Rhoederick, E. H. *Metal-Semiconductor Contacts.* Clarendon Press, Oxford, (1978).

[64] Lüth, H. *Solid Surfaces, Interfaces and Thin Films.* Springer, (2001).

[65] Bardeen, J. *Phys. Rev.* **71**, 717 (1947).

[66] Meyerhof, W. E. *Phys. Rev.* **69**, 42 (1946).

[67] Spicer, W. E., Chye, P. W., Skeath, P. R., Su, C. Y., and Lindau, I. *J. Vac. Sci. Technol.* **16**, 1422 (1979).

[68] Spicer, W. E., Lindau, I., Skealth, P., and Su, C. Y. *J. Vac. Sci. Technol.* **17**, 1019 (1980).

[69] Newman, N., Spicer, W. E., Kendelewicz, T., and Lindau, I. *J. Vac. Sci. Technol. B* **4**, 931 (1986).

[70] Spicer, W. E., Miyano, K., Kendelewicz, T., Lindau, I., Weber, E., and Z. Liliental-Weber, N. N. *Appl. Surf. Sci.* **41/42**, 1 (1989).

[71] Spicer, W. E., Cao, R., Miyano, K., Kendelewicz, T., Lindau, I., Weber, E., Liliental-Weber, Z., and Newman, N. *Appl. Surf. Sci.* **41/42**, 1 (1989).

[72] Spicer, W. E. and Green, A. M. *J. Vac. Sci. Technol. B* **11**, 1347 (1993).

[73] Heine, V. *Phys. Rev. A* **138**, 1689 (1965).

[74] Tersoff, J. *Phys. Rev. B* **30**, 4874 (1984).

[75] Tersoff, J. *Phys. Rev. B* **32**, 6968 (1985).

[76] Tersoff, J. *Surf. Sci.* **168**, 275 (1986).

[77] Tersoff, J. *Phys. Rev. Lett.* **56**, 2755 (1986).

[78] Pauling, L. *The Nature of the Chemical Bond.* Cornell University Press, Ithaca, (1960).

[79] Troost, D., L.Koenders, Fan, L.-Y., and Mönch, W. *J. Vac. Sci. Technol. B* **5(4)**, 1119 (1987).

[80] Koenders, L., Blömacher, M., and Mönch, W. *J. Vac. Sci. Technol. B* **6(4)**, 1416 (1988).

[81] Mönch, W. *J. Appl. Phys.* **80**, 5076 (1996).

[82] Mönch, W. *J. Appl. Phys.* **80**, 5076 (1996).

[83] Mönch, W. *J. Vac. Sci. Technol. B* **17**, 1867 (1999).

[84] Brillson, L. J. *Phys. Rev. Lett.* **40**, 260 (1977).

[85] Eastman, D. E., Chiang, T.-C., Heimann, P., and Himpsel, F. J. *Phys. Rev. Lett.* **45**, 656 (1980).

[86] Kendelexicz, T., Petro, W. G., Pan, S. H., Williams, M. D., Lindau, I., and Spicer, W. E. *Appl. Phys. Lett.* **44**, 113 (1984).

[87] Ludeke, R., D.Straub, Himpsel, F. J., and Landgren, G. *J. Vac. Sci. Technol. A* **4**, 874 (1985).

[88] Ludeke, R. and Landgren, G. *Phys. Rev. B* **33**, 5526 (1986).

[89] Doniach, S. and Sunjic, M. *J. Phys. C* **3**, 285 (1970).

[90] Freeouf, J. L. and Woodall, J. M. *J. Vac. Sci. Technol.* **19(3)**, 794 (1981).

[91] Freeouf, J. L. and Woodall, J. M. *Appl. Phys. Lett.* **39**, 727 (1981).

[92] Drude, P. *Ann. Phys.* **1**, 566 (1900).

[93] Drude, P. *Ann. Phys.* **3**, 369 (1900).

[94] Lu, R. P., Morgan, B. A., Kavanagh, K. L., Powell, C. J., Chen, P. J., Serpa, F. G., and Engelhof, W. F. *J. Appl. Phys.* **87**, 5164 (2000).

[95] Fuchs, K. *Proc. Cambridge Philos. Soc.* **34**, 100 (1938).

[96] Sondheimer, H. *Adv. Phys.* **1**, 1 (1952).

[97] MacDonald, D. K. C. and Sarginson, K. *Proc. Roy. Soc. A* **203**, 223 (1950).

[98] Celotta, R. J., Pierce, D. T., and Wang, G.-C. *Phys. Rev. Lett.* **43**, 728 (1979).

[99] Bringer, A., Campagna, M., Feder, R., Kisker, E., and Kulhmann, E. *Phys. Rev. Lett.* **42**, 1705 (1979).

[100] Rendell, R. W. and Penn, D. R. *J. Appl. Phys.* **52**, 1620 (1981).

[101] Barnas, J., Fuss, A., Camley, R. E., Grünberg, P., and Zinn, W. *Phys. Rev. B* **42**, 8110 (1990).

[102] Schönhense, G. and Siegmann, H. C. *Ann. Phys. (Leipzig)* **505 (2)**, 465 (1993).

[103] Pappas, D. P., Kämper, K., Miller, B. P., Hopster, H., Fowler, D. E., Brundle, C. R., Luntz, A. C., and Shen, Z. X. *Phys. Rev. Lett.* **66**, 504 (1991).

[104] Gröbli, J. C., Oberli, D., and Meier, F. *Phys. Rev. B* **52**, R13095 (1993).

[105] Aeschlimann, M., Bauer, M., Pawlik, S., Weber, W., Burgermeister, R., Oberli, D., and Siegmann, H. C. *Phys. Rev. Lett* **79**, 5158 (1997).

[106] Drouhin, H. J., van der Sluijs, A. J., Lassailly, Y., and Lampel, G. *J. Appl. Phys.* **79**, 4734 (1996).

[107] Oberli, D., Burgermeister, R., Riesen, S., Weber, W., and Siegmann, H. C. *Phys. Rev. Lett* **81**, 4228 (1998).

[108] Rippard, W. H. and Buhrman, R. H. *Phys. Rev. Lett.* **84**, 971 (2000).

[109] Girardin, C., Coratger, R., Pechou, R., Ajustron, F., and Beauvillian, J. *J. Phys. III* **6**, 661 (1996).

[110] Bell, L. D. *Phys. Rev. Lett.* **77**, 3893 (1996).

[111] Monsma, D. J., Lodder, J. C., Popma, T. J. A., and Dieny, B. *Phys. Rev. Lett.* **74(26)**, 5260 (1995).

[112] Vlutters, R., van't Erve, O. M. J., Kim, S. D., Jansens, R., and Lodder, J. C. *Phys. Rev. Lett.* **88**, 027202 (2002).

[113] Hong, J. and Mills, D. L. *Phys. Rev. B* **59**, 13840 (1999).

[114] Hong, J. and Mills, D. L. *Phys. Rev. B* **62**, 5589 (2000).

[115] Grundler, D. *Phys. Rev. B* **63**, 161307(R) (2001).

[116] Möller, C. H., Heyn, C., and Grundler, D. *Appl. Phys. Lett.* **83**, 2181 (2003).

[117] Binnig, G., Rohrer, H., Gerberer, C., and Weibel, E. *Phys. Rev. Lett.* **49**, 57 (1982).

[118] Binnig, G., Rohrer, H., Gerberer, C., and Weibel, E. *Appl. Phys. Lett.* **40**, 178 (1982).

[119] Binnig, G., Rohrer, H., Gerberer, C., and Weibel, E. *Phys. Rev. Lett.* **50**, 120 (1983).

[120] Czerkas, S. *Ph.D. Thesis.* Universität Bielefeld, (2004).

[121] Binnig, G. and Rohrer, H. *Rev. Mod. Phys.* **59**, 615 (1987).

[122] Binnig, G. and Rohrer, H. *Rev. Mod. Phys.* **71**, S324 (1999).

[123] Kaiser, W. J. and Bell, L. D. *Phys. Rev. Lett.* **60**, 1406 (1988).

[124] Bell, L. D. and Kaiser, W. J. *Phys. Rev. Lett.* **61**, 2368 (1988).

[125] Smoliner, J., Rakozcy, D., and Kast, M. *Rep. Prog. Phys.* **67**, 1863 (2004).

[126] Kinno, T., Tanaka, K., and Mizushima, K. *Phys. Rev. B* **56**, R4391 (1997).

[127] Rippard, W. H. and Buhrman, R. H. *Appl. Phys. Lett.* **75**, 1001 (1999).

[128] Monsma, D. J., Vlutters, R., and Lodder, J. C. *Science* **281**, 407 (199).

[129] Jansen, R., van't Erve, O. M. J., Kim, S. D., Vlutters, R., Kumar, P. S. A., and Lodder, J. C. *J. Appl. Phys.* **89(11)**, 7431 (2001).

[130] Jansen, R., Gokhan, H., van t'Erve, O. M. J., Potsma, F. M., and Lodder, J. C. *J. Appl. Phys.* **95**, 6927 (2004).

[131] Jansen, R. *J. Phys. D* **36**, R289 (2003).

[132] Sato, R. and Mizushima, K. *Appl. Phys. Lett.* **79**, 1157 (2001).

[133] van Dijken, S., Jiang, X., and Parkin, S. P. *Appl. Phys. Lett.* **83**, 951 (2003).

[134] Jansen, R., van t'Erve, O. M. J., Potsma, F. M., and Lodder, J. C. *Appl. Phys. Lett* **84**, 4337 (2004).

[135] Chelikowski, J. R. and Cohen, M. L. *Phys. Rev. Lett.* **32**, 674 (1973).

[136] Tiemann, L. *Diploma Thesis.* Universität Bielefeld, (2004).

[137] Liliental-Weber, Z., Gronski, R., Washburn, J., Newman, N., Spicer, W. E., and Weber, E. R. *J. Vac. Sci. Technol. B* **11**, 912 (1986).

[138] Justus, M. *Ph.D. Thesis.* Universität Bielefeld, (2003).

[139] Thomas, A., Brückl, H., Sacher, M. D., Schmalhorst, J., and Reiss, G. *J. Vac. Sci. Technol. B* **21**, 2120 (2003).

[140] Kubota, H., Reiss, G., Brückl, H., Schepper, W., Wecker, J., and Gieres, G. *Jap. J. Appl. Phys.* **41**, L180 (2002).

[141] Pedersen, R. J. and Vernon, F. L. *Appl. Phys. Lett.* **10**, 29 (1967).

[142] Meiklejohn, W. H. and Bean, C. P. *Phys. Rev.* **102**, 1413 (1956).

[143] Meiklejohn, W. H. and Bean, C. P. *Phys. Rev.* **105**, 904 (1957).

[144] Néel, L. *Annales de Physique* **2**, 61 (1967).

[145] Stoner, E. C. and Wohlfarth, E. P. *Phil. Trans. R. Soc. A* **240**, 599 (1948).

[146] http://math.nist.gov/oommf.

[147] Kerr, J. *Rep. Brit. Ass.* **5** (1876).

[148] Kerr, J. *Phil. Mag.* **3**, 321 (1877).

[149] Hulme, H. R. *Proc. R. Soc. A* **135**, 237 (1932).

[150] Argyres, P. N. *Phys. Rev.* **97**, 334 (1955).

[151] Bechthold, P. *Magnetooptische Effekte: Phänomenologische Beschreibung und Anwendung*, chapter GMR Experimente, C.8.1–C8.33. 30. IFF-Ferienkurs, Forschungszentrum Jülich (1999).

[152] Knoll, M. and Ruska, E. *Z. Physik* **78**, 318 (1932).

[153] v. Borries, B. and Ruska, E. *Z. Physik* **83**, 187 (1933).

[154] Fullerton, E., Margulies, D., Schabes, M., Carey, M., Gurney, B., Moser, A., Best, M., Zeltzer, G., Rubin, K., Rosen, H., and Doerner, M. *Appl. Phys. Lett.* **77**, 3806 (2000).

[155] Result from XRD-investigations in the scope of *BMBF-Leitprojekt "Magneto-Electronik"*, supported by *Robert Bosch GmbH*, information by A. Hütten .

[156] Allongue, P. and Souteyrand, E. *J. Vac. Sci. Technol. B* **5**, 1644 (1987).

[157] Waldrop, J. R. *J. Vac. Sci. Technol. B* **2**, 445 (1984).

[158] Gurney, B. A., Speriosu, V. S., Nozieres, J.-P., Lefakis, H., Wilhoit, D. R., and Need, O. U. *Phys. Rev. Lett.* **71**, 4023 (1993).

[159] Johnson, M. *Phys. Rev. Lett.* **70**, 2142 (1993).

[160] Heer, R., Eder, C., Smoliner, J., and Gornik, E. *Rev. Sci. Instrum.* **68(12)**, 4488 (1997).

[161] Eder, C., Smoliner, J., and Strasser, G. *Appl. Phys. Lett.* **68(20)**, 2876 (1996).

[162] Haq, E., Gokcan, H., Banerjee, T., Potsma, F. M., Siekmann, M. H., Jansen, R., and Lodder, J. C. *J. Appl. Phys.* **95**, 6930 (2004).

[163] Dietze, H. D. and Thomas, H. *Z. Physik* **163**, 523 (1961).

[164] Kittel, C. *Einführung in die Festkörperphysik, 11. Auflage.* Oldenbourg Verlag, (1996).

[165] Heer, R., Smoliner, J., Bornemeier, J., and Brückl, H. *Appl. Phys. Lett* **85**, 4388 (2004).

[166] Fiederling, R., Grabs, P., Ossau, W., Schmidt, G., and Molenkamp, L. W. *Appl. Phys. Lett.* **82**, 2160 (2003).

[167] Fiedering, R., Keim, M., Reuscher, G., Ossau, W., Schmidt, G., Waag, A., and Molenkamp, L. W. *Nature* **204**, 787 (1999).

[168] Zhu, H. J., Ramsteiner, M., Kostial, H., Wassermeier, M., Schönherr, H.-P., , and Ploog, K. H. *Phys. Rev. Lett.* **87**, 016601 (2001).

[169] de Wijs, G. A. and de Groot, R. A. *Phys. Rev. B* **64**, 020402(R) (2001).

[170] de Groot, R. A., Mueller, F. M., van Engen, P. G., and Buschow, K. J. H. *Phys. Rev. Lett.* **50**, 2024 (1983).

[171] Tanaka, C. T., Nowak, J., and Moodera, J. S. *J. Appl. Phys.* **86**, 6239 (1999).

[172] Soulen, R. J., Byers, J. M., Osofsky, M. S., Nadgorny, B., Ambrose, T., Cheng, S. F., Broussard, P. R., Tanaka, C. T., Nowak, J., Moodera, J. S., Barry, A., and Coey, J. M. D. *Nature* **282**, 85 (1998).

[173] Kämmerer, S. *Ph.D. Thesis.* Universität Bielefeld, (2004).

[174] Urbaniak, M., Schmalhorst, J., Thomas, A., Brückl, H., Reiss, G., Lucinski, T., and Stobiecki, F. *Physica Status Solidi B,* **199(2)**, 284 (2003).

[175] Rashba, E. I. *Phys Rev. B* **62**, R16267 (2000).

[176] Rakoczy, D., Strasser, G., and Smoliner, J. *Physica B* **314(1-4)**, 81 (2002).

Publications and Conferences

Publications

- Brückl, H., Thomas,A., Schotter, J., Bornemeier, J. and Reiss, G., "New Developments with Magnetic Tunnel Junctions", Advances in Solid State Physics **43**, ed. B. Kramer, Springer Verlag Berlin, 397, (2003)
- Heer, R., Smoliner, J., Bornemeier, J. and Brückl, H., "Magnetic tunnel transistors studied by ballistic electron emission microscopy", Appl. Phys. Lett. **85**, 4388 (2004)
- Bornemeier, J., Reiss, G. and Brueckl, H., "Ballistic Electron Injection from Co into GaAs via Magnetic Tunnel Junctions", submitted
- Heer, R., Smoliner, J., Bornemeier, J. and Brueckl, H., "Temperature Dependent Ballistic Transport through Spinvalve Structures", submitted

Conferences

- Poster: DPG-Frühjahrstagung Hamburg (2001), "Spinabhängige Leitfähigkeit mit ballistischen Elektronen"
- Poster: DPG-Frühjahrstagung Regensburg (2002), "Herstellung und Charakterisierung magnetischer Tunnelelemente mit Schottkybarrieren"
- Poster: DPG-Frühjahrstagung Dresden (2003), "Injection of ballistic Electrons into Semiconductors"

- Talk: DPG-Frühjahrstagung Berlin (2005) ”Ballistic Magneto-Current in Magnetic Tunnel Junctions”

Acknowledgements

This thesis would not have been possible without the support of several people. I am deeply grateful for the help of all co-workers in the D2 department. Special thanks goes to the following persons:

I thank Günter Reiss and Hubert Brückl as well as Andreas Hütten and Jan Schmalhorst for the supervision and founding of my work. Moreover, my thanks go also to Karsten Rott for the practical support, especially lithography, and the fruitful discussion.

Furthermore, I thank Maik Justus, Dirk Meyners and Dirk Brinkmann for software support and Sonja Heitmann for XRD measurements. For discussions on my work and lab support, I thank (additionally to the already mentioned persons) Slawek Czerkas, Andy Thomas, Lars Tiemann, Jörg Schotter, Michael Panhorst and Sven Kämmerer. I appreciate the help of the department's mechanical workshop, and especially Dieter Gollay from the electronic workshop for their uncomplicated and creative help.

Beside the co-workers in Bielefeld this thesis was supported by two other groups:

I would like to express my gratitude to Jürgen Smoliner and Rudi Heer from the TU Vienna for the BEEM measurements as well as the co-operation and the support in Gallium Arsenide application. Furthermore I would like to thank Thomas Hägler and Josef Zweck from the Universität Regensburg for the fast and non-bureaucratic delivery of TEM cross section pictures.

I thank Doris Mikesky for proofreading. Furthermore, I would like to thank my family and friends for their continuous support.

Bielefeld (Germany), January 20th 2004 Jan Bornemeier

Danksagung

Die Erstellung dieser Arbeit wäre ohne die Hilfe einiger Personen nicht möglich gewesen. Ich bin allen Kollegen der Abteilung D2 zutiefst zu Dank verpflichtet. Mein besonderer Dank geht an die im folgenden erwähnten Personen:

Für die Betreuung und finanzielle Unterstützung dieser Doktorarbeit danke ich Günter Reiss, Hubert Brückl sowie Andreas Hütten und Jan Schmalhorst. Darüber hinaus geht mein Dank an Karsten Rott für praktische Hilfe, insbesondere bei der Lithographie und für konstruktive Diskussionen.

Ebenfalls danke ich Maik Justus, Dirk Meyners und Dirk Brinkmann für die Erstellung bzw. Untersützung bei der Software des Messprogramms und Sonja Heitmann für XRD Messungen. Zusätzlich zu den bereits erwähnten Personen geht mein Dank an Slawek Czerkas, Andy Thomas, Lars Tiemann, Jörg Schotter, Michael Panhorst und Sven Kämmerer für Unterstützung im Labor und Diskussionen. Der Mechanik Werkstatt und besonders Dieter Gollay aus der Elektronik Werkstatt danke ich ebenfalls für die unkomplizierte und kreative Hilfe.

Außer von den Kollegen in Bielefeld habe ich von zwei weiteren Gruppen Unterstützung erfahren:

Die BEEM Messungen wurden an der TU Wien von Jürgen Smoliner und Rudi Heer durchgeführt. Selbige haben mich zum Umgang mit Gallium Arsenids beraten. Thomas Hägler und Josef Zweck haben die TEM Bilder schnell und unbürokratisch geliefert. An diese Personen geht mein Dank ebenfalls.

Weiterhin möchte ich mich bei Doris Mikesky für das Korrekturlesen bedanken. Nicht zuletzt will ich mich noch bei meiner Familie und meinen Freunden bedanken, deren stetige Unterstützung mir immer sicher war.

Bielefeld, der 20. Januar 2005 Jan Bornemeier